②

NAVAL POSTGRADUATE SCHOOL
Monterey, California

DISSERTATION

BAROTROPIC VORTEX ADJUSTMENT
TO ASYMMETRIC FORCING
WITH APPLICATION TO
TROPICAL CYCLONE MOTION

by

Lester E. Carr III

September 1989

Dissertation Supervisor   R. L. Elsberry

90 03 29 085

Unclassified

security classification of this page

REPORT DOCUMENTATION PAGE

1a Report Security Classification Unclassified	1b Restrictive Markings
2a Security Classification Authority	3 Distribution Availability of Report
2b Declassification Downgrading Schedule	Approved for public release; distribution is unlimited.

4 Performing Organization Report Number(s)	5 Monitoring Organization Report Number(s)

6a Name of Performing Organization Naval Postgraduate School	6b Office Symbol *(if applicable)* 35	7a Name of Monitoring Organization Naval Postgraduate School
6c Address *(city, state, and ZIP code)* Monterey, CA 93943-5000		7b Address *(city, state, and ZIP code)* Monterey, CA 93943-5000

8a Name of Funding Sponsoring Organization	8b Office Symbol *(if applicable)*	9 Procurement Instrument Identification Number
8c Address *(city, state, and ZIP code)*		10 Source of Funding Numbers

10 Source of Funding Numbers			
Program Element No	Project No	Task No	Work Unit Accession No

11 Title *(include security classification)* BAROTROPIC VORTEX ADJUSTMENT TO ASYMMETRIC FORCING WITH APPLICATION TO TROPICAL CYCLONE MOTION

12 Personal Author(s) Lester E. Carr III

13a Type of Report Doctoral Dissertation	13b Time Covered From To	14 Date of Report *(year, month, day)* September 1989	15 Page Count 158

16 Supplementary Notation The views expressed in this thesis are those of the author and do not reflect the official policy or position of the Department of Defense or the U.S. Government.

17 Cosati Codes			18 Subject Terms *(continue on reverse if necessary and identify by block number)*
Field	Group	Subgroup	Tropical cyclone motion, Vortex stability, Vortex propagation

19 Abstract *(continue on reverse if necessary and identify by block number)*

A nondivergent, barotropic analytical model to predict steady tropical cyclone (TC) propagation relative to the large-scale environment is developed in terms of a "self-advection" process in which the TC is advected by an azimuthal wavenumber one gyre flow that results from TC-environment interaction. The model is comprehensive in that it includes the first-order effects of all of the dynamical influences that are presently understood to be important to barotropic propagation: gradients of planetary and environmental vorticity, changes in TC wind structure, and environmental windshear. An unforced version of the model is used to show that angular windshear in the symmetric TC circulation acts to damp perturbations from axisymmetry by tilting the perturbations downshear. The resultant transfer of kinetic energy from perturbation to symmetric circulation thus tends to restore axisymmetry. Thus, steady propagation of TC-like barotropic vortices is a manifestation of a stable response to asymmetric forcing. To predict both the asymmetric gyre flow and the propagation it induces, the forced Barotropic Self-Advection Model (BSAM) is closed by seeking a particular pattern in the vorticity tendencies of the TC-environmental interaction flow. For realistic combinations of environmental vorticity gradients and linear windshear, the BSAM predicts propagation speeds and directions that are consistent with TC propagation characteristics observed in composite data. The capability of the BSAM to account for variable TC structure is used to show that errors in determining TC outer wind strength of ±1 m/s can result in an 85 km forecast error at 48 h. Finally, and most importantly, the capability of the BSAM to initialize a barotropic numerical model so that quasi-steady TC propagation occurs almost immediately is demonstrated for several simple dynamical situations.

20 Distribution Availability of Abstract ☒ unclassified unlimited ☐ same as report ☐ DTIC users	21 Abstract Security Classification Unclassified	
22a Name of Responsible Individual R. L. Elsberry	22b Telephone *(include Area code)* (408) 646-2373	22c Office Symbol 63Es

DD FORM 1473,84 MAR   83 APR edition may be used until exhausted   security classification of this page
All other editions are obsolete

Unclassified

i

Barotropic Vortex Adjustment to Asymmetric Forcing
with Application to Tropical Cyclone Motion

by

Lester E. Carr III
Lieutenant Commander, United States Navy
B.S., United States Naval Academy, 1977

Submitted in partial fulfillment of the
requirements for the degree of

DOCTOR OF PHILOSOPHY IN METEOROLOGY

from the
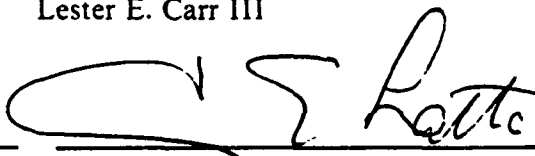
NAVAL POSTGRADUATE SCHOOL
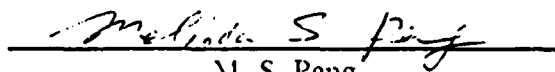September 1989

Author: _____

Lester E. Carr III

Approved by: _____

P. A. Durkee   G. E. Latta
Associate Professor of Meteorology   Professor of Mathematics

M. S. Peng   D. C. Smith IV
Adj. Res. Professor of Meteorology   Assistant Professor of Oceanography

R. T. Williams   R. L. Elsberry
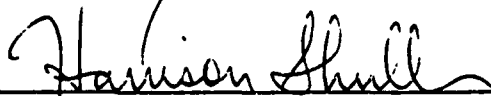Professor of Meteorology   Professor of Meteorology
Dissertation Co-advisor   Dissertation Supervisor

Approved by: _____

Robert J. Renard, Chairman, Department of Meteorology

Approved by: _____

Harrison Shull, Provost and Academic Dean

ii

ABSTRACT

A nondivergent, barotropic analytical model to predict steady tropical cyclone (TC) propagation relative to the large-scale environment is developed in terms of a "self-advection" process in which the TC is advected by an azimuthal wavenumber one gyre flow that results from TC-environment interaction. The model is comprehensive in that it includes the first-order effects of all of the dynamical influences that are presently understood to be important to barotropic propagation: gradients of planetary and environmental vorticity, changes in TC wind structure, and environmental windshear. An unforced version of the model is used to show that angular windshear in the symmetric TC circulation acts to damp perturbations from axisymmetry by tilting the perturbations downshear. The resultant transfer of kinetic energy from perturbation to symmetric circulation thus tends to restore axisymmetry. Thus, steady propagation of TC-like barotropic vortices is a manifestation of a stable response to asymmetric forcing. To predict both the asymmetric gyre flow and the propagation it induces, the forced Barotropic Self-Advection Model (BSAM) is closed by seeking a particular pattern in the vorticity tendencies of the TC-environmental interaction flow. For realistic combinations of environmental vorticity gradients and linear windshear, the BSAM predicts propagation speeds and directions that are consistent with TC propagation characteristics observed in composite data. The capability of the BSAM to account for variable TC structure is used to show that errors in determining TC outer wind strength of ± 1 m/s can result in an 85 km forecast error at 48 h. Finally, and most importantly, the capability of the BSAM to initialize a barotropic numerical model so that quasi-steady TC propagation occurs almost immediately is demonstrated for several simple dynamical situations.

iii

TABLE OF CONTENTS

LIST OF TABLES

LIST OF FIGURES

ACKNOWLEDGMENTS

During the course of this research, I have received expert insight and guidance from a number of highly skilled and professional individuals. I am indebted to my dissertation supervisor, Professor R. L. Elsberry, for the unparalleled editorial supervision that he diligently provided as I wrote this dissertation, and for his broad insights into the tropical cyclone motion problem that have helped me see the applications that lie beyond the theory. The broad experience and expertise in geophysical fluid dynamics of my co-advisor, Professor R. T. Williams, were instrumental in helping me attack the dynamic complexities associated with this research. On more than one occasion, his guidance helped me to choose the right "fork in the road." A special thanks goes to Professor G. E. Latta who expertly guided me through half of my mathematics minor, and whose love for and fascination with the classical methods of mathematical physics motivated me to choose a research topic that heavily relied on such techniques. Professor A. Schoenstadt of the Mathematics Department also provided some key guidance concerning the modeling approach used in this dissertation. I also wish to thank the other members of the dissertation committee, Professors P. A. Durkee, M. S. Peng and D. C. Smith IV for many helpful discussions over the course of the research program.

Finally, and most importantly, I would like to thank my wife, Terann, and children, Hilary and Jeremy, for their support and patience during the past fours years when the demands of task at hand sometimes required longer than desired absences from their loving company.

I. INTRODUCTION

It is well known that tropical cyclone (TC) motion persistently differs from the mean advective effect (*i.e.*, the "steering") of the large-scale environment (*e.g.*, George and Gray 1976; Chan and Gray 1982). The precise speed and direction of this velocity difference (hereafter referred to as "propagation") depends to some extent on the particular steering flow definition employed, but is generally westward and poleward in direction and 1 to 2.5 m/s in magnitude (Carr and Elsberry 1989). Although this propagation velocity is typically smaller than the advection by environmental steering, it can induce significant TC track errors (2 m/s $\approx$ 170 km/d) if not properly accounted for in dynamical models. Interestingly, it is well known that numerical model forecasts of TC tracks generally have less skill than CLIPER (CLImatology and PERsistance) over the first 24-36 h, and that the error is primarily an underestimation of TC speed (*e.g.*, Neumann and Pelissier 1981; their Figs. 4,8 respectively). Since TC's track generally westward and poleward throughout much of their lifetimes, such statistics provide circumstantial evidence that dynamical forecast models do not as yet properly account for TC propagation until about 1 day into the numerical integration. It will be shown that the initial slowness of numerical models may result from initializing the model with a symmetric TC structure that lacks any propagation-inducing asymmetries caused by TC-environment interaction. Although past modeling experience indicates that both barotropic and baroclinic processes can cause TC propagation asymmetries, the general goal of this research is to develop an improved theoretical model for understanding and predicting the barotropic contributions to TC propagation asymmetries.

A. MODELING REVIEW

1. Status of basic understanding

a. β-induced propagation

The propagation of an initially symmetric, nondivergent barotropic (NDBT) vortex in a quiescent environment due to the influence of planetary rotation, as approximated by a β-plane, provides the most basic dynamical scenario for beginning a review of TC motion theory. The northwestward propagation at 2-3 m/s noted by Chan and William (1987; hereafter CW) in a recent numerical study of this problem is generally consistent with the propagation observed in previous numerical studies (Anthes and Hoke 1975; Kitade 1981; DeMaria 1985, hereafter DM). The authors of the previous

1

numerical studies attributed their results to the traditional linear theories of barotropic vortex propagation advocated in various forms (*e.g.*, Rossby 1939, 1948; Kasahara 1957; Kasahara and Platzmann 1963; Holland 1983). An interesting aspect of these theoretical predictions is that the westward and poleward components of the propagation are associated with different linear mechanisms, *e.g.*, Rossby wave propagation by the TC to the west as opposed to poleward acceleration due to net Coriolis force on the TC. In contrast, CW concluded that only the nonlinear "self-advection" (*i.e.*, the TC advecting its own vorticity) process associated with the development of a horizontal asymmetry in the TC windfield was responsible for both the westward and poleward components of the propagation.

The basis for this important distinction can be demonstrated by partitioning the vortex flow into a steady symmetric (S) component and an asymmetric (A) component that is generally small by comparison. In a coordinate system centered at any instant on the symmetric component, the propagation process in a quiescent environment is approximately described by

$$\frac{\partial \zeta_A}{\partial t} = -\mathbf{V}_A \cdot \nabla \zeta_S - \mathbf{V}_S \cdot \nabla \zeta_A - \mathbf{V}_S \cdot \nabla f, \qquad (1.1)$$

       (a)   (b)   (c)   (d)

where term (a) represents the vorticity tendency associated with motion and or distortion of the TC due to the combined effect of the two dominant self-advection terms (b and c) and the advection of planetary vorticity (d). Linear theories regard the westward component of propagation as a Rossby wave-like propagation associated with the east-west dipole of vorticity tendency generated by term (d), and either eliminate self-advection by requiring the TC to be symmetric at all times (*e.g.*, Kasahara and Platzman 1963), or assume that self-advection is implicit in computations of observed steering flows (*e.g.*, Holland 1983, 1984). When the nonlinear self-advection term was omitted from their model, CW noted that advection of planetary vorticity by the TC is a strong dispersive distorting influence, but by itself generates negligible motion of the TC center (≈ 0.3 m s). Thus, they concluded that the linear process generates the asymmetric flow essential to the existence of the self-advection process, but the self-advective interaction of the symmetric and asymmetric TC components actually causes the propagation.

Fiorino (1987) and Fiorino and Elsberry (1989; hereafter FE) clarified the individual roles of the two primary self-advection processes (terms b and c) via a diag-

2

nostic technique that extracts V_S and V_A from a numerical model similar to that used by CW. Their analysis showed that the structure of V_A is predominantly an azimuthal wavenumber one asymmetry that consists of two counterrotating gyres (hereafter referred to as "wavenumber one gyres") that produce a near-uniform flow across the central region of the TC. The average velocity of the uniform flow is very nearly equal to the TC propagation vector, which indicates that NDBT β-induced propagation is essentially an advection of symmetric TC vorticity by the asymmetric flow component of the TC, *i.e.*, term (b) of (1.1). This is somewhat surprising since simple scale arguments suggest that the advection of asymmetric vorticity by the symmetric tangential wind (term c) should be equally important to the propagation process. However, FE demonstrated that streamfunction tendencies associated with term (c) nearly cancel those associated with term (d) after a quasi-steady state is achieved. Thus, term (c) acts primarily to limit the growth of the wavenumber one gyres and the resultant propagation to nearly steady values after an initial adjustment period of approximately 24-48 h.

A theoretical model that accurately predicts β-induced gyre structure and the associated propagation based on this recently identified self-advection process has yet to be developed, and this is the principal objective of this research. The successful development of such a model that confirms the numerical work of CW and FE will be an important step in establishing the nonlinear self-advection principle as the mechanism responsible for barotropic TC propagation as opposed to the traditional linear Rossby wave arguments.

Since advection of planetary vorticity by a vortical flow represents essentially steady asymmetric forcing, FE's results suggest that advection by the symmetric tangential wind tends to stabilize a barotropic approximation of a TC to such forcing. Nonlinear advection is necessary to permit dispersion-resistant movement of model vortices in general (*e.g.*, McWilliams and Flierl 1979; Mied and Lindemann 1979), or nondispersive movement in the case of very specialized entities known as either modons or solitary eddy solutions (see Flierl *et al.* 1980). However, the precise mechanism by which nonlinear advection stabilizes a vortex of arbitrary radial structure has not been identified. Because steady barotropic vortex propagation is essentially a manifestation of this stability to asymmetric forcing, a thorough analysis of this process is important to improved understanding of barotropic TC propagation, and thus is another objective of this research.

It is important to briefly address the question whether barotropic vortex propagation stability is a sufficiently important process compared to potential baroclinic

3

influences to warrant the present barotropic modeling effort. Although Holland (1983) has suggested that inertial stability accounts for near axisymmetry in the inner 300 km of a TC, inertial stabilization cannot occur in NDBT or quasi-geostrophic models. The qualitatitive similarity of TC propagation tracks in simple baroclinic models (*e.g.*, Madala and Piacsek 1975; Kitade 1980) to barotropic results provides at least circumstantial evidence that baroclinic TC stability/propagation is more a modification to, as opposed to being fundamentally different from, the barotropic phenomenon. Thus, it is reasonable to assume that TC propagation/stability is fundamentally a vorticity advection process that should be fully understood within a barotropic context before additional baroclinic complexities are added.

b. Influence of TC structure

By using an initial vortex specification that permits independent variations of the inner and outer tangential wind structure, FE clearly showed TC propagation is strongly dependent on outer wind changes (strength), but is virtually independent of inner wind changes (intensity) as predicted by earlier researchers (Holland 1983; DM). In particular, an increase of only a few m/s in the initial tangential wind between 300 and 800 km results in a faster and more westward TC propagation that can significantly alter the β-induced TC track. Although the initial value of TC total relative angular momentum (RAM) has been cited as having a potentially important influence on TC tracks (DeMaria 1987), Shapiro and Ooyama (1989) have recently shown that β-induced motion does not depend on initial TC RAM in any well-defined way. Since RAM is essentially an integral (and therefore not unique) measure of TC strength, TC propagation variations due to changes in RAM are likely a manifestation of the dependence on TC strength described by FE.

In view of the above, it is clear that properly initializing dynamical forecast models for TC strength, and ensuring that the model dynamics/physics maintain an accurate TC outer wind profile throughout the integration are important areas for ongoing research. Without aircraft, improved measurements of TC structure for initializing operational forecast models can only be achieved by advancement in remote sensing capabilities. Designing utilizing remote sensors to better detect TC strength and choosing model parameterizations to best maintain a desired TC structure both depend on improved understanding of the nature and sensitivity of TC propagation dependence on outer wind strength. Thus, an additional objective of this research is to identify the dynamical basis for this dependence and provide at least a preliminary assessment of the

wind measurement accuracy required to adequately account for the influence of TC outer wind strength on the barotropic propagation process.

c. Influence of divergence

Anthes and Hoke (1975) noted significant differences in the β-induced TC motion tracks predicted by nondivergent and divergent (5 km depth) barotropic numerical models, which they attributed to divergence-induced slowing of Rossby wave phase speeds. Such a result would suggest that nondivergent forecast models such as SANBAR (Sanders et al. 1975) fail to account for a significant propagation process. In a model comparison similar to Anthes and Hoke, Shapiro and Ooyama (1989) found nearly identical propagation tracks, even though substantially more divergence was included (1 km depth). Thus, Shapiro and Ooyama concluded that the earlier result was due to dissimilar initial TC structures that were employed in the divergent and nondivergent models. This result is important for clarifying the minimal role divergence plays in barotropic TC propagation, and also supports the choice of a NDBT dynamical framework for the theoretical model employed in this study. In addition, their result re-emphasizes the important influence of initial TC specification on the accuracy of TC tracks predicted by a barotropic model.

d. Environmentally-induced propagation

Barotropic models also have been used to study the influence of horizontally nonuniform environmental winds on TC propagation relative to steering. The additional influences on the propagation process may be described by rewriting (1.1) as

$$\frac{\partial \zeta_A}{\partial t} = - V_A \cdot \nabla \zeta_S - V_S \cdot \nabla \zeta_A - V_S \cdot \nabla (f + \zeta_E) - V_E \cdot \nabla (\zeta_S + \zeta_A), \quad (1.2)$$

$$\text{(a)} \qquad \text{(b)} \qquad \text{(c)} \qquad \text{(d)} \qquad \text{(e)}$$

in which the environmental (E) processes $V_E \cdot \nabla (f + \zeta_E)$ and $\partial \zeta_E / \partial t$ have been omitted since they relate to the evolution of the steering flow. Terms (a), (b) and (c) of (1.2) are the same as in (1.1). However, term (d) of (1.2) now includes advection of environmental vorticity by the TC, and a new term (e) accounts for both steering and shearing of the symmetric TC and wavenumber one gyres by the environmental wind.

With the addition of variable environmental winds, it becomes essentially a matter of convention whether V_A should be associated with the symmetric TC (V_S) in which case the term "self-advection" is still meaningful, or whether V_A should be regarded as a modification to V_E, and thus a contribution to steering. The comparison of

5

observational data with theory presented in Section C will provide strong evidence to suggest that V_A will be manifested as propagation rather than a contribution to conventionally computed environmental steering. Thus, V_A will continue to be referred to as a self-advection flow associated with TC-environment interaction, and will be regarded as distinct from the steering associated with V_E.

In a NDBT numerical study with steady zonal winds that varied only with latitude, DM noted that the poleward component of propagation associated with a TC in a poleward (equatorward) gradient of environmental vorticity increased (decreased) the northward propagation component relative to β alone. DM attributed his results to the linear theory of Kasahara and Platzman (1963), which predicts that horizontal variability of the environmental winds will induce TC propagation in the direction of and 90° to the left of the large-scale gradient of absolute vorticity. This theory is essentially a direct extension of Rossby's westward propagation (1939) and poleward acceleration (1948) of TC's due to β alone. The presence of ζ_E in term (d) of (1.2) would make Kasahara and Platzman's hypothesis intuitively plausible. However, the recent demonstration by CW that linear advection of planetary vorticity only distorts the TC must also apply to the advection of environmental vorticity by the TC. DM's results clearly indicate that environmental vorticity gradients alter barotropic TC propagation. This suggests that Kasahara and Platzmann's theory of a linear absolute vorticity-induced propagation due to the combined effects of β and ζ_E can be recast within the context of the nonlinear self-advection mechanism recently identified. Thus, another objective of this research will be to determine the extent to which a self-advection model for β-induced propagation can also accomodate the presence of a horizontally variable windfield.

Any analogy between the propagation-inducing effects of β and ζ_E is complicated by the additional distorting influence of environmental wind shear in term (e) of (1.2). In a barotropic model that includes β and an environmental current with only linear shear, Chan and Williams (1989) found that cyclonic (anticyclonic) shear induces a westward (eastward) curving TC propagation relative to the tracks induced by β alone. They also noted that the orientation of the wavenumber one gyres rotates consistently with the propagation changes, which suggests that this process is due to shearing of gyre vorticity by the rotational part of the environmental current. Although curving TC tracks are also evident in the results of DM who used a sinusoidal windfield, the effect is much smaller than that seen by Chan and Williams. Because of the potentially im-

portant impact of environmental shear on TC propagation direction, modeling of this linear shear process will be included in this research.

2. Status of propagation/gyre prediction models

a. Recent results

The preceding discussion of the self-advection mechanism for barotropic TC propagation has been based on diagnostic analyses of numerical modeling results. Theoretical models of TC motion that explicitly predict wave number one gyre structure and associated propagation based on the self-advection concept are also being developed. The limited success of such models as discussed below has provided motivation for this research.

Given the intense advective influence of the TC's tangential winds, the quasi-steady nature of the β-induced wavenumber one gyre observed by FE suggests that it is a standing azimuthal wave. Such a wave would propagate clockwise in a Rossby wave-like manner on the basic state vorticity gradient represented by the symmetric component of the TC via term (b) of (1.1). On the basis of such a hypothesis and an assumption as in (1.1) and (1.2) that $V_A << V_S$ over a large area, Willoughby (1988) formulated a linear shallow model that explicitly predicts the structure of such "vorticity waves" as well as the propagation they induce. He solved the potential vorticity and divergence equations in a polar coordinate system moving with the TC for a range of possible propagation velocities, and assumed that the correct propagation velocity would minimize the Lagrangian of the system as required by Hamilton's Principle from variational calculus. By incorporating a rotating mass source-sink pair to approximate asymmetric eyewall convection, he obtained a vorticity wave angular frequency that agrees well with that of small-scale trochoidal oscillations observed in TC tracks. This result suggests that TC track oscillations are also explainable in terms of a barotropic self-advection process associated with asymmetric convection, as opposed to the traditional Magnus force theory (Kuo 1950; Yeh 1950).

Willoughby's model failed to predict a correct propagation velocity on a β-plane (quiescent environment), presumably due to a barotropic instability studied by Peng and Williams (1989) in a nondivergent version of the model. Peng and Williams showed that existence of the instability depends on the vorticity gradient sign reversal of the TC (necessary condition) and sufficient model resolution to resolve the small scale of the instability (radius of maximum winds). Thus, they suggest that this linear instability is dynamically based, but is highly damped in full numerical models due to a combination of nonlinear interaction and coarse horizontal resolutionn. However, ana-

7

lytical gyre propagation models such as the one discussed in the next paragraph and the one developed herein do not experience the instability. Further analysis of this process is necessary to resolve the apparent paradox, but this issue is not considered within the scope of the present research.

Smith *et al.* (1989) have devised an approximate analytical model for the β-induced gyre structure by ignoring vortex propagation and computing the streamfunction associated with a redistribution of the initial absolute vorticity by the symmetric TC. The inner gyre uniform flow predicted by the model closely approximates the propagation speeds predicted by nonlinear numerical models up to about 24 h. Smith (personal communication, 1989) is presently modifying the model to extend the period of accurate propagation prediction by empirically accounting for the movement of the TC.

b. Application

A natural application for a barotropic TC propagation model would be as part of a track prediction scheme that computes total TC motion at any time by adding: i) a steering velocity obtained from a numerical model for the evolution of the large-scale environmental winds; and ii) a propagation velocity derived from the theoretical model based on the gradient of absolute (or potential) vorticity of the numerically generated environmental winds. Early efforts based on linear propagation theory (Kasahara 1957; Kasahara and Platzman 1963) included the cross-vorticity gradient propagation effect, but ignored the hypothesized up-vorticity gradient acceleration of the TC. In fact, this supposed acceleration due to a net force on "the vortex" has never been transformed into a calculated propagation velocity. A recent track prediction model developed by Holland (1983; 1984) computes westward propagation due to β similar to the earlier efforts, but also includes a northward propagation effect by empirically accounting for net convergence into the TC. That these models have shown only limited forecast skill is not surprising in light of the recent self-advection theory of propagation, and the skill that they do possess is probably due to some portion of the actual nonlinear self-advection phenomenon being parameterized by the linear models.

The present unavailability of an accurate TC propagation model based on nonlinear self-advection has precluded any implementation into an "advection + propagation" track prediction model analogous to the linear models. Although the present model may prove suitable for this type of endeavor, development and testing of such a model is outside the scope of this research. Unlike the linear propagation models that are insensitive to small deviations of the TC from axisymmetry, self-advection models

depend fundamentally on such asymmetries, and more importantly, actually predict their structure (*e.g.*, Willoughby 1988; Smith *et al.* 1989). Accurate predictions of such gyre structures would be ideally suited for initializing barotropic numerical models such as SANBAR (Sanders *et al.* 1975) so that quasi-steady propagation occurs immediately at the start of the integration rather than after the 24-48 h typically observed for an initially symmetric TC (*e.g.*, DM; CW; FE). This dissertation will conclude with a proof-of-concept demonstration of how the gyre/propagation model developed here can be used to improve numerical model initialization.

B. OBSERVATIONAL EVIDENCE FOR PROPAGATION

Given the many barotropic models of TC propagation in the literature, it is natural to ask whether observational evidence exists to support the predictions of the theoretical or numerical models. Unfortunately, data deficiencies have made computation of propagation for an individual TC difficult. However, studies that average the data from many TC's to produce a "composite" TC are available for this purpose. The propagation vectors in Fig. 1.1 from Carr and Elsberry (1989) are based on data from two such studies (George and Gray 1976; Chan and Gray 1982). A description of the process by which the vectors were obtained is given in Appendix A.

1. Comparison with modeling results

The propagation vectors in Fig. 1.1 exhibit a number of interesting properties that strongly resemble the TC propagation in the numerical models cited above. Except for the anomalous "after recurvature" vector (Fig. 1.1f), the vectors have magnitudes ranging from 1.0 to 2.5 m s and directions that tend to be westward and poleward in both hemispheres, which is consistent with the numerical and analytical results previously cited. In addition, the rotation of the propagation vector direction from west-southwestward for westward moving TC's to northwestward for eastward moving TC's in the direction stratification (Fig. 1.1b) is consistent with DM's numerical results. DM showed that the change in the direction of the environmental vorticity gradient from poleward on the poleward side of the subtropical ridge to equatorward on the equatorward side caused a decrease in the meridional component of TC propagation similar to that in Fig. 1.1b. Finally, the propagation vectors in the intensity stratification (Fig. 1.1d) have a direct dependence on TC intensity. As discussed earlier, the modeling studies of DM and FE demonstrate that a nondivergent barotropic prediction of TC propagation due to β is independent of TC intensity, but is well correlated with outer wind strength (see Merrill 1984 for typical definitions of strength and inten-
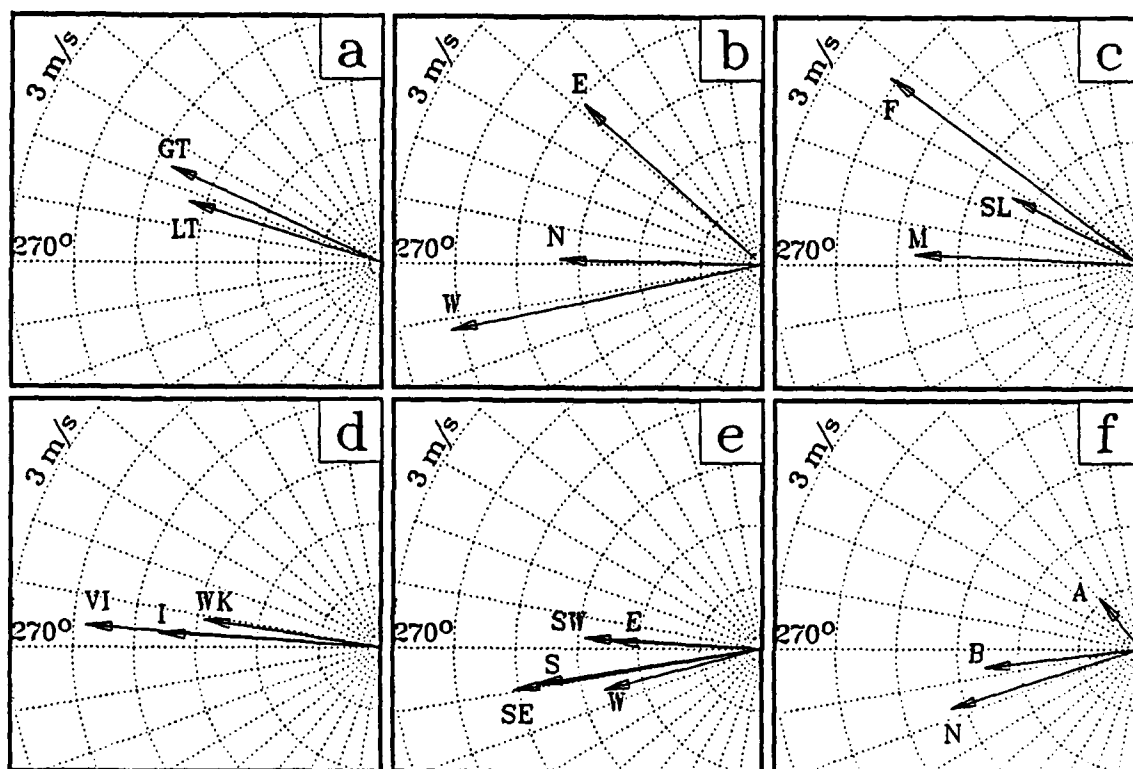
Fig. 1.1 Vector differences of composite TC motion minus steering for the (a) latitude, (b) direction, (c) speed and (d) intensity stratifications of Chan and Gray (1982), and the (e) direction and (f) recurvature stratifications of Holland (1984). The vector identification labels correspond to those in column 1 of Tables A.1 and A.2.

sity). Since a weak correlation exists between the intensity and strength of TC's (Weatherford and Gray 1988), the increase in propagation vector magnitude in Fig. 1.1d may be a manifestation of the numerically-predicted dependence of β-induced propagation on TC strength.

The results in Fig. 1.1 also contain some apparent inconsistencies. Examples are: i) the significantly larger meridional components of the Northern Hemisphere vectors compared to that of the Southern Hemisphere vectors; and ii) the presence of equatorward components in some of the propagation vectors. Such properties may be associated with boundary layer or baroclinic processes not considered in the barotropic theories. However, a possible barotropic explanation might be the presence of east-west vorticity gradients in the TC environment that were excluded by DM. For example, a large-scale westward relative vorticity gradient is present during the summer in the troposphere between the anticyclone over the western North Pacific and the heat low over southeastern Asia. Based on DM's results, a TC vortex embedded in such a vorticity gradient should have a westward, and more importantly, a southward component of propagation. Since the meridional gradient of environmental relative vorticity and β are in opposite directions south of the Northern Hemisphere subtropical ridge, the zonal gradient of environmental vorticity might tend to dominate, and thus explain the southward component of vector W in Fig. 1.1b. In contrast, the meridional environmental vorticity gradient and β are in the same direction north of the Northern Hemisphere subtropical ridge, and thus might dominate over the influence of a zonal vorticity gradient in the cases of vectors N and E in Fig. 1.1b. Differences in the direction of the large-scale absolute vorticity gradients in the Northern and Southern Hemispheres thus may contribute to the hemispheric variability of the data shown here. The present propagation model will permit testing of such a hypothesis within a modeling context since the influence of an east-west environmental vorticity gradient will be included.

Statistical influences in Fig. 1.1 also must be considered, such as: i) ambiguities introduced by composite stratifications that may incorporate multiple propagation-inducing influences; and ii) possible random or systematic errors in the composite data that may be significant relative to the small size of the propagation vectors being analyzed (e.g., accuracy of rawinsonde wind measurements and error in locating the TC center position). Random and systematic errors should be reduced as sample sizes are increased and observational accuracies are improved respectively.

11

2. Interpretation of observed propagation vectors

The fundamentally important issue that determines the mechanism responsible for observed TC propagation is whether or not a TC-interaction flow (V_A) will be manifested as an essentially inseparable contribution to conventionally computed environnmental steering. If V_A is included within the steering, then the observed TC propagation vectors must be due to some mechanism other than self-advection, at least within the context of the barotropic theory. If a self-advection flow is not accounted for in the computed environmental steering flows, then the observed propagation vectors may indeed represent the self-advection process.

Holland (1983) assumed that V_A is included in the steering, and he has proposed a linear propagation model that is consistent with the near-zonal orientation of the Australian-Southwest Pacific difference vectors (Fig. 1.1e-f). Holland assumes that inertial stability constrains the inner core of the TC to move with the outer envelope, which is assumed to propagate westward as a Rossby wave with a phase speed appropriate to an "effective radius." In practice, the "effective radius" parameter for a particular storm and time is chosen to give a barotropic Rossby wave propagation speed that equals the observed westward component of TC propagation over a preceding time interval. Although Holland proposed low-level convergence to account for small deviations from pure westward motion, the above discussion of environmental shear in addition to β is an alternative explanation.

In contrast to Holland's assumptions, FE's explicit illustration of the wavenumber one structure of the self-advection flow provides strong evidence that V_A is, for the most part, not included in the steering. Key aspects of this structure are that the central uniform flow portion of the gyres that account for the propagation is confined to radii less than 300 km from the TC center, and that the gyre flow is considerably weaker outside that radius. Even allowing for somewhat larger gyres in actual TC's, this suggests that the uniform flow region of the interaction flow would be largely unaccounted for in a steering flow calculated over an annulus of 5°-7° lat. radius from the TC center as is the case for the data used to produce Fig. 1.1. Thus, "self-advection" should be manifested primarily as propagation, rather than as a contribution to conventionally calculated steering flows. Thus, Holland's linear model may actually include nonlinear motion-inducing processes since the selection of an effective radius is based on the observed difference between TC motion and steering over a preceding time interval.

Accurate measurement of steering near the TC center will continue to be problematic for the foreseeable future. Thus, it seems advisable as a practical matter to continue to compute steering at a large scale ($\approx$ 1000 km) as is now done, and to regard the self-advection flow as a propagation-inducing process that is distinct from steering by the large-scale environment. In light of the subsynoptic scale region in which the self-advective flow is influential, such a flow partitioning may also be a good approximation to the long-sought scheme to uniquely separate the TC from its environment. Thus, this research will use the three-part partitioning scheme proposed in Elsberry (1986) that consists of: i) a symmetric TC; ii) a propagation-inducing TC-environment interaction flow; and iii) a large-scale environmental flow component that accounts for TC steering.

C. DISSERTATION OVERVIEW

In summary, the specific objectives of this research are:

1. identification and analysis of the specific mechanism responsible for barotropic vortex stability to asymmetric forcing, and how this stabilizing influence is related to TC motion;

2. development and analysis of a theoretical model for barotropic TC propagation due to both planetary and environmental vorticity effects that is based on nonlinear self-advection, and that accurately predicts gyre structure and associated propagation velocity relative to equivalent numerical model solutions;

3. identification of the dynamical basis for the dependence of barotropic TC propagation of outer wind strength, and an assessment of the wind measurements required to account for this phenomenon; and

4. provide a preliminary demonstration of the viability of self-advection propagation models for improved initialization of barotropic TC track forecasting models.

Because of the mathematical complexity of the model to be constructed, Chapter II will be devoted to preliminary development and analysis. Objectives 1 and 2 above will be addressed in Chapters III and IV respectively, and the theoretical aspect of Objective 3 will be addressed in Chapter IV as well. In Chapter V, the model will be applied to satisfy the second half on Objective 3 and Objective 4. Chapter VI will conclude the dissertation with an overview of the modeling approach and a summary of results.

II. PRELIMINARY MODEL DEVELOPMENT

A. REFERENCE FRAME TRANSFORMATION

The behavior of fluid motion in a NDBT system on a β-plane is governed by the conservation of absolute vorticity, which may be expressed as

$$\frac{d}{dt}(\zeta + f) = 0 \qquad (2.1)$$

$$\zeta = \mathbf{k} \cdot \nabla \times \mathbf{V} \qquad (2.2)$$

$$f = f_o + \beta y , \qquad (2.3)$$

where ζ is the local vertical component of relative vorticity, β is the linearized latitudinal derivative of the Coriolis parameter f, and f_o is the average value of f in the domain. In terms of Eulerian partial derivatives, (2.1) may be expressed as

$$\frac{\partial \zeta}{\partial t} + \mathbf{V} \cdot \nabla(\zeta + f) = 0 . \qquad (2.4)$$

A formal partitioning of the total fluid flow that takes advantage of the near-axisymmetry of TC's as suggested by (1.1) and (1.2) requires (2.4) to be transformed to a reference frame moving with the TC at a translation velocity $\mathbf{C}(t)$. In terms of cartesian coordinates, the relationship between the position vectors for an arbitrary point P in each reference frame is illustrated in Fig. 2.1, and is mathematically defined by

$$\mathbf{R}(x, y) = \mathbf{R}'(x', y') + \int_0^t \mathbf{C}(\tau) d\tau , \qquad (2.5)$$

where the (') symbol denotes variables in the moving reference frame. Let the (') symbol also define certain derivative operations in the moving reference frame

$$\nabla' \equiv \mathbf{i} \frac{\partial}{\partial x'} \bigg|_{y', t = const} + \mathbf{j} \frac{\partial}{\partial y'} \bigg|_{x', t = const} \qquad (2.6)$$

$$\frac{\partial'}{\partial t} \equiv \frac{\partial}{\partial t} \bigg|_{x', y' = const} . \qquad (2.7)$$

14
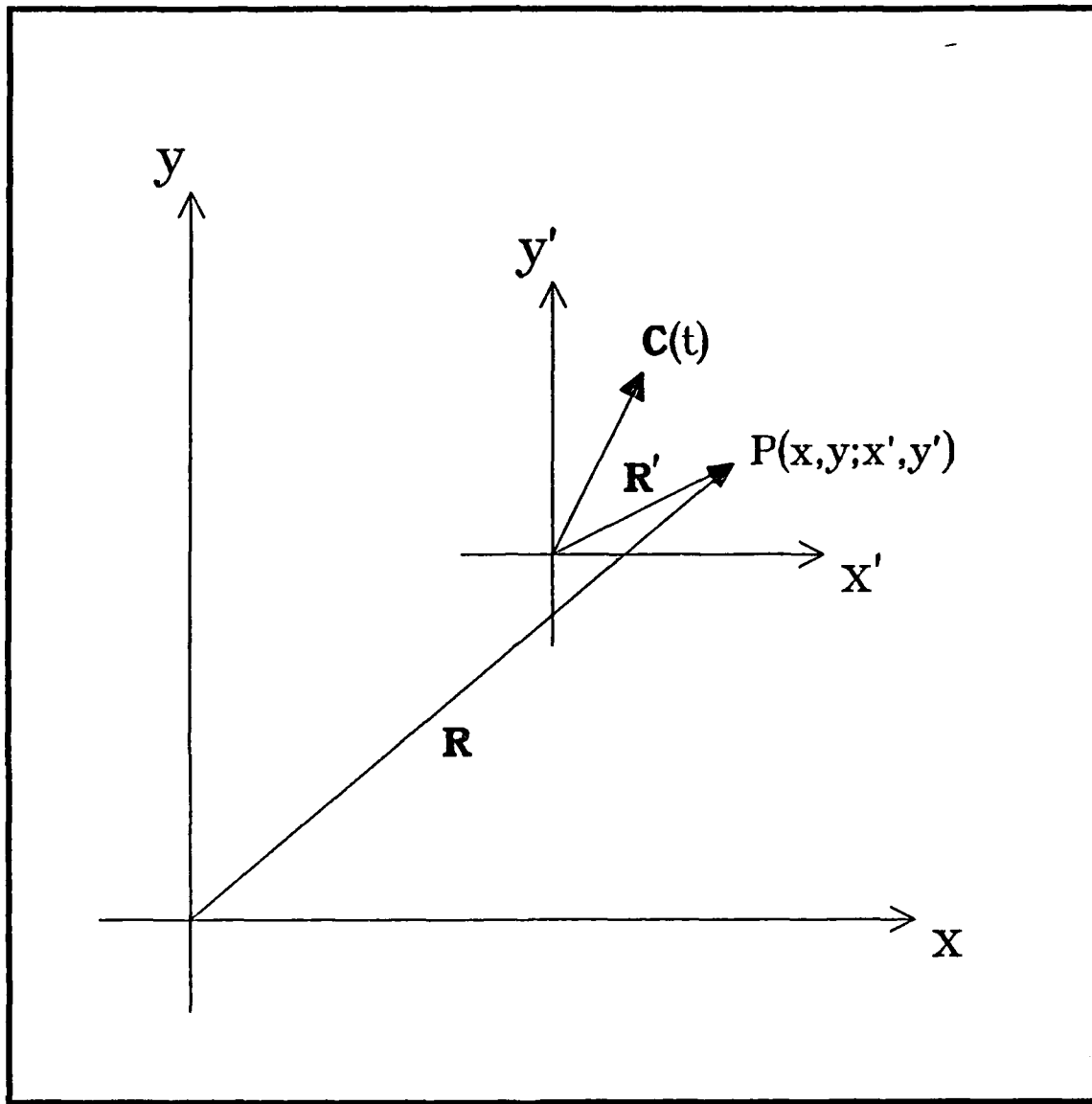
Fig. 2.1 Relationship between the position vectors of an arbitrary point P in a reference frame fixed to the surface of the earth (unprimed variables), and in a reference frame moving at velocity C(t) (primed variables).

15

By using the chain rule and (2.5)-(2.7), it may shown that

$$\nabla = \nabla' \qquad (2.8)$$

$$\frac{\partial}{\partial t} = \frac{\partial'}{\partial t} - \mathbf{C} \cdot \nabla', \qquad (2.9)$$

which, when substituted into (2.4), results in the desired transformed expression

$$\left(\frac{\partial'}{\partial t} - \mathbf{C} \cdot \nabla' \right) \zeta + \mathbf{V} \cdot \nabla'(\zeta + f'). \qquad (2.10)$$

It is important to note that a convention of leaving the dependent variables untransformed in (2.10) has been employed. Although relative vorticity and the gradient of the Coriolis parameter are invariant with respect to the coordinate transformation, fluid velocity is not. Thus, the velocity transformation

$$\mathbf{V} = \mathbf{V}' + \mathbf{C}(t), \qquad (2.11)$$

obtained from d/dt of (2.5) has not been used. This results in explicit advection by $\mathbf{C}$ in (2.10), but has the desirable property of avoiding an implicit dependence of the fluid flow on $\mathbf{C}$ in the moving reference frame. Such a convention is necessary to justify the use of the homogeneous boundary conditions that will be employed in solving this model, and facilitates later use of the solutions in a numerical model initialization scheme.

B. FLOW PARTITIONING

As outlined in Chapter I, the total fluid flow is partitioned into

$$\mathbf{V} = \mathbf{V}_S + \mathbf{V}_E + \mathbf{V}_A, \qquad (2.12)$$

according to the following definitions: i) $\mathbf{V}_S$ is a known symmetric (S) TC flow component that is steady in the moving reference frame; ii) $\mathbf{V}_E$ is a known environmental (E) flow; and iii) $\mathbf{V}_A$ is a predominantly asymmetric (A) flow component that represents as yet unknown interactions between the symmetric TC and the specified environmental flow. Subject to these definitions, substituting (2.12) into (2.10) gives

$$\left(\frac{\partial'}{\partial t} - \mathbf{C} \cdot \nabla' \right)(\zeta_A + \zeta_E) - \mathbf{C} \cdot \nabla' \zeta_S + \mathbf{V}_S \cdot \nabla'(\zeta_A + \zeta_E + f')$$

$$+ (\mathbf{V}_E + \mathbf{V}_A) \cdot \nabla'(\zeta_S + \zeta_A + \zeta_E + f') = 0, \qquad (2.13)$$

16

in which the term $V_S \cdot \nabla'\zeta_S$ is absent since V_S is by definition orthogonal to $\nabla'\zeta_S$. Removing the terms associated with the symmetric TC and interaction flows from (2.13) gives

$$\left(\frac{\partial'}{\partial t} - C \cdot \nabla'\right)\zeta_E + V_E \cdot \nabla'(\zeta_E + f') = 0, \qquad (2.14)$$

which defines the evolution of the environmental winds in the absence of the TC with respect to the moving reference frame. Subtracting (2.14) from (2.13) gives

$$\frac{\partial \zeta_A}{\partial t} + (V_S + V_E - C) \cdot \nabla\zeta_A + (V_A - C) \cdot \nabla\zeta_S$$

$$+ V_A \cdot \nabla(\zeta_A + \zeta_E + f) = - V_E \cdot \nabla\zeta_S - V_S \cdot \nabla(\zeta_E + f), \qquad (2.15)$$

in which the (') symbols have been omitted for simplicity. In all subsequent analysis, independent variables will be relative to the moving reference frame. The various terms of (2.15) have been grouped so that the left side represents a nonlinear partial differential equation for the evolution of the interaction flow in response to two asymmetry-inducing forcing terms on the right side. The first forcing term includes: i) distortion of the symmetric TC vorticity field due to large-scale horizontal windshear; and ii) steering of the TC by the environmental winds. The second forcing term represents the dispersive effect of Rossby wave radiation associated with the advection of large-scale absolute vorticity by the tangential wind of the symmetric TC. The TC translation velocity C also appears on the left side of (2.15), and represents an additional unknown.

The effect of requiring (2.14) to hold with the TC present is that the interaction flow must represent all changes to both the symmetric TC and the "basic state" environment due to the interaction process. However, the earlier assumption that V_S may be regarded as steady in the moving reference frame simplifies the interpretation of (2.15) to a purely asymmetric interaction flow that can cause TC propagation relative to the large-scale environment described by (2.14). The assumption of a steady TC is regarded as a good first-order approximation to lessen the considerable complexity of the TC motion problem evident even in NDBT dynamics. However, such an assumption excludes the potential impact of TC strength and intensity changes from the scope of this research.

As noted above, the first term on the right side of (2.15) represents both steering and shearing of the TC by the environmental wind. As a result, the TC translation velocity C incorporates both a known advection by V_E as determined by (2.14), and an unknown

17

propagation velocity associated with the interaction flow V_A. To separate the known and unknown effects, a pure shearing component of the environmental wind relative to the center of the symmetric TC may be defined as

$$\hat{V}_E(r, \theta, t) = V_E(r, \theta, t) - V_E(0,0,t), \tag{2.16}$$

where $V_E(0,0,t)$ represents the instantaneous value of V_E at the TC center. Note that $V_E(0,0,t)$ provides a theoretically useful definition of environmental steering for this model. A propagation velocity $\hat{C}$ then may be defined by

$$\hat{C}(t) \equiv C(t) - V_E(0,0,t). \tag{2.17}$$

Substituting (2.16) and (2.17) into (2.15) gives

$$\frac{\partial \zeta_A}{\partial t} + (V_S + \hat{V}_E - \hat{C}) \cdot \nabla \zeta_A + (V_A - \hat{C}) \cdot \nabla \zeta_S$$

$$+ V_A \cdot \nabla(\zeta_A + \zeta_E + f) = - \hat{V}_E \cdot \nabla \zeta_S - V_S \cdot \nabla(\zeta_E + f), \tag{2.18}$$

in which the unknowns are the self-advection flow field and the associated propagation velocity $\hat{C}$.

It should be noted that (2.14) and (2.18) represent the basis for a "propagation + advection" track prediction model based on self-advection that is analogous to the traditional linear versions discussed earlier. Equation (2.14) could be numerically integrated to provide $V_E(0,0,t)$ at appropriate time intervals, while a solution to (2.18) would provide information on TC propagation. As discussed earlier, this research will focus on solving and analyzing several approximate forms of (2.18). The remainder of this chapter describes the additional assumptions and concepts on which the solutions in Chapters III and IV are predicated.

C. SIMPLIFYING ASSUMPTIONS

1. Adjustment time concept

Except for special circumstances, (2.14) indicates that the environmental windfield will evolve with time. The resultant temporal variability of $\hat{V}_E$ and ζ_E makes (2.18) analytically intractable for use as a theoretical propagation model without some simplifying assumption regarding the time dimension in (2.18).

As discussed in Chapter I, an initially symmetric TC in a NDBT numerical model will propagate in response to steady large-scale forcing at a nearly steady velocity and with quasi-steady asymmetric structure after a transient adjustment period of about 24-48 h (DM; CW; FE). The transient phase results from choosing an initial TC structure that differs from the steady-state structure. Since TC's are continually subjected to environmental forcing, it may be expected that mature TC's in a steady or slowly varying large-scale windfield possess an asymmetric structure that reflects nearly complete adjustment to the asymmetric forcing of the environment. Thus, the temporal varibility of $\hat{V}_E$ and ζ_E in (2.18) will be eliminated by regarding the t variable in (2.18) as a hypothetical "adjustment time" during which a "first-guess" symmetric TC will develop a quasi-steady asymmetry appropriate to the forcing defined by (2.14) at any instant.

In a rapidly varying large-scale environment, the TC may not be fully adjusted to the asymmetric forcing of the environment, such as during TC interaction with a rapidly moving midlatitude trough. Without high resolution observational data to analyze TC propagation and horizontal asymmetries under such circumstances, a quantitative estimate for the amount of error associated with a steady-state propagation model is not possible. Thus, it is simply noted that the present model may be less accurate in such circumstances.

2. Matched solution approach

a. The transition radius

The magnitudes of the wind speed and vorticity of the symmetric TC component are much larger than the corresponding asymmetric and environmental components over a significant horizontal area in the lower and middle troposphere. Since TC tangential winds decay to essentially zero at large radius, a region must exist in which the magnitudes of the asymmetric interaction and environmental flows are as large as the symmetric flow. This radius is called the "transition radius," and will be denoted by R_T. The value of R_T will depend on the structure of the symmetric TC and the environmental windfield under consideration, and would vary with height in baroclinic situations. Subject to some additional assumptions delineated in Chapter IV, a single transition radius will be assumed to exist for the barotropic model used here.

b. Self-advection Region

For $r < R_T$, it is assumed that advective terms in (2.18) not involving the symmetric flow will be negligible. Based on such an assumption, (2.18) simplifies to

$$\frac{\partial \zeta_A}{\partial t} + \mathbf{V}_S \cdot \nabla \zeta_A + (\mathbf{V}_A - \hat{\mathbf{C}}) \cdot \nabla \zeta_S = - \hat{\mathbf{V}}_E \cdot \nabla \zeta_S - \mathbf{V}_S \cdot \nabla (\zeta_E + f) \, . \quad (2.19)$$

The circular area within which (2.19) applies will be called the Self-advection Region since mutual advection by the asymmetric interaction flow and the symmetric TC flow dominate the left side of (2.19). It should be noted that the Self-advection Region assumption is equivalent to regarding the interaction flow as a linear perturbation to the symmetric TC flow.

c. Dispersion Region

For $r > R_T$, it is assumed that self-advection terms on the left side of (2.18) will be negligible relative to advection terms involving the environment and either the symmetric TC or interaction flow. Based on this assumption, (2.18) simplifies to

$$\frac{\partial \zeta_A}{\partial t} + \hat{\mathbf{V}}_E \cdot \nabla \zeta_A + \mathbf{V}_A \cdot \nabla (\zeta_E + f) = - \hat{\mathbf{V}}_E \cdot \nabla \zeta_S - \mathbf{V}_S \cdot \nabla (\zeta_E + f) \, . \quad (2.20)$$

The outer area in which (2.20) applies will be called the Dispersion Region since mutual advection by the interaction and symmetric TC flows, which enables barotropic vortices to resist dispersion, is excluded.

d. Asymptotic assumption

In an annular region where $r \approx R_T$, the assumptions that distinguish the Self-advection Region and Dispersion Region are not valid. However, (2.19) and (2.20) are suitable for a developing a matched solution for a propagation-inducing interaction flow field that becomes asymptotically close to an exact solution to (2.18) as r becomes larger or smaller than R_T. Such a matched-asymptotic-solution approach will be used in Chapter IV.

3. Isolating wavenumber one processes

The diagnostic analysis by FE showed that the interaction flow field (their "ventilation flow") responsible for TC propagation due to just β has a predominantly azimuthal wavenumber one structure. Chan and Williams (1989) have shown that the interaction flow maintains an predominantly wavenumber one structure in the presence of horizontal wind shear in the environment, even though forcing at higher wavenumbers is present. The absence of significant wavenumber two and higher components in the interaction flow will be addressed in the stability analysis of Chapter III.

The observation that only a wavenumber one flow structure should cause TC propagation is intuitively plausible since only a wavenumber one gyre will produce

20

nonzero flow across the center of the symmetric TC (Fig. 2.2). Formally establishing this concept and simplifying governing equations for the Self-advection and Dispersion Regions is facilitated by writing (2.19) and (2.20) in component form. In a polar coordinate system centered on the symmetric TC,

$$\mathbf{V}_S = v_S(r)\,\mathbf{\Theta}, \tag{2.21a}$$

$$\mathbf{V}_A = u_A(r,\theta,t)\,\mathbf{r} + v_A(r,\theta,t)\,\mathbf{\Theta}, \tag{2.21b}$$

$$\hat{\mathbf{C}}(t) = \hat{C}(t)\,[\cos(\theta-\alpha)\,\mathbf{r} - \sin(\theta-\alpha)\,\mathbf{\Theta}], \tag{2.21c}$$

where $\mathbf{r}$ and $\mathbf{\Theta}$ are unit vectors in the radial and azimuthal directions respectively, and $\hat{C}$ and α are the propagation speed and direction respectively. The mathematical convention of measuring angles counter-clockwise from east has been used. In addition, let

$$\hat{\mathbf{V}}_E = \hat{u}_E(r,\theta)\,\mathbf{i} + \hat{v}_E(r,\theta)\,\mathbf{j}, \tag{2.22}$$

in which conventional cartesian symbology has been used for the environmental wind components and unit vectors. Note that in view of the adjustment time concept, (2.22) contains no dependence on time.

a. Wavenumber one Self-advection Region equation

Substituting (2.21a,b,c) and (2.22) into (2.19) gives

$$\frac{\partial \zeta_A}{\partial t} + \frac{v_S}{r}\frac{\partial \zeta_A}{\partial \theta} + [u_A - \hat{C}\cos(\theta-\alpha)]\frac{\partial \zeta_S}{\partial r} =$$

$$-\hat{u}_E\frac{\partial \zeta_S}{\partial r}\cos\theta - \hat{v}_E\frac{\partial \zeta_S}{\partial r}\sin\theta - v_S\left(\frac{\partial \zeta_E}{\partial y} + \beta\right)\cos\theta + v_S\frac{\partial \zeta_E}{\partial x}\sin\theta. \tag{2.23}$$

$$\text{(a)} \qquad\qquad \text{(b)} \qquad\qquad \text{(c)} \qquad\qquad \text{(d)}$$

Since both $\partial \zeta_S/\partial r$ and $\hat{C}$ are independent of azimuth, the propagation term on the left side of (2.23) is a wavenumber one process. Only projections onto wavenumber one by the forcing terms on the right side of (2.23) can cause TC propagation, because projections onto other wavenumbers are orthogonal to the propagation term. The validity of this result depends on the assumption that the term $\hat{\mathbf{C}} \cdot \nabla \zeta_A$ may be neglected in both the Self-advection and Dispersion Regions. Since ζ_A is by definition a function of θ, projections of forcing onto other wavenumbers can potentially influence
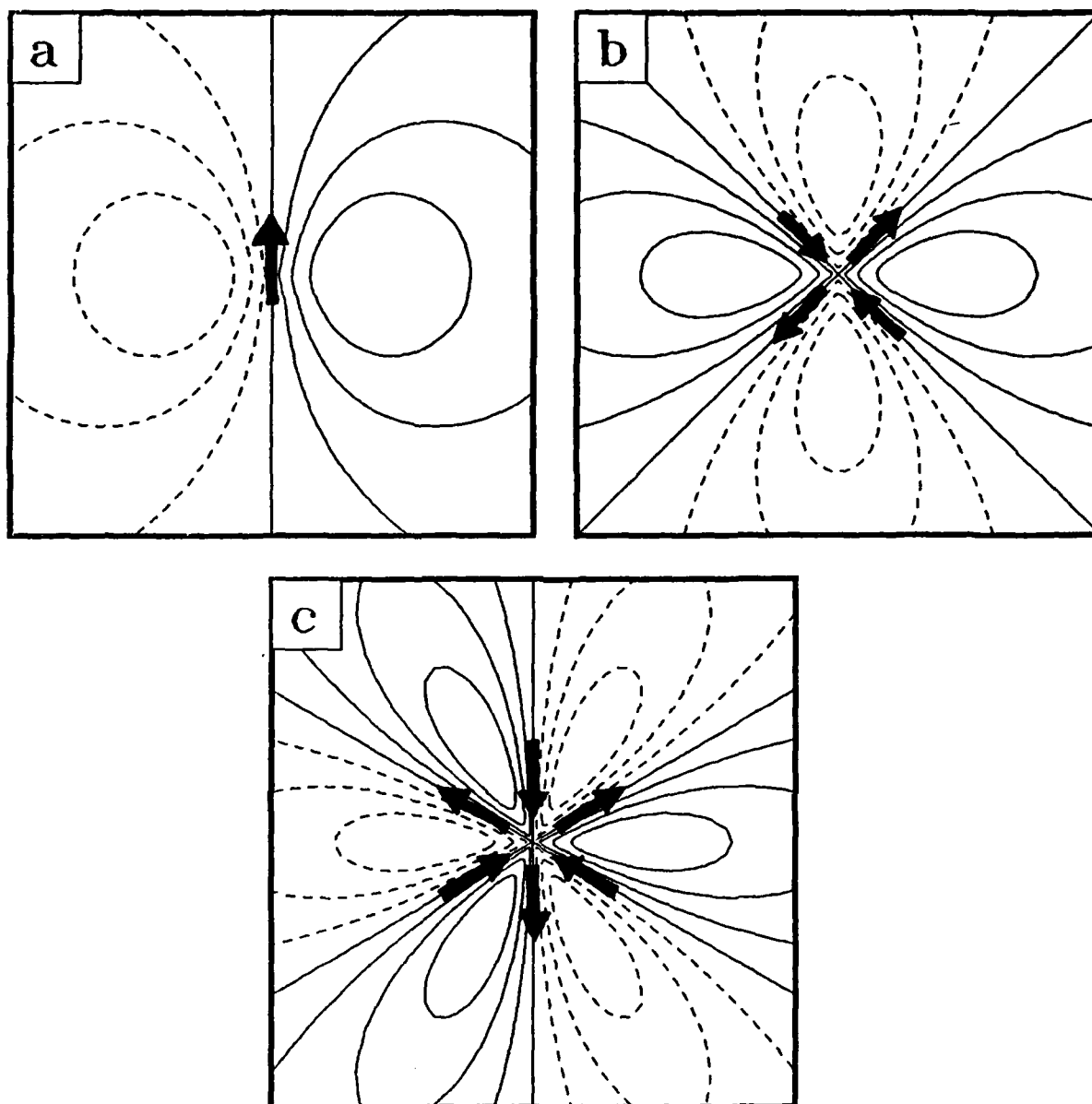
Fig. 2.2 Hypothetical streamfunction patterns (solid, positive; dashed, negative) for flows that are purely azimuthal wavenumber: (a) one; (b) two; and (c) three. Arrows indicate general direction of the flow at that location.

TC propagation via this term. However, FE's finding that TC propagation was almost completely accounted for by advection by the wavenumber one gyre provides numerical support for regarding the interaction flow as a linear perturbation to the symmetric TC.

Simplifying (2.23) to include only the dominant wavenumber one influence of each term is facilitated by writing the environmental flow factors as truncated Taylor series of the form

$$\hat{u}_E, \hat{v}_E, \frac{\partial \zeta_E}{\partial x}, \frac{\partial \zeta_E}{\partial y} = A_0 + A_1 r \cos(\theta + \phi_1). \tag{2.24}$$

Since (2.16) requires A_0 in (2.24) to be zero for $\hat{u}_E$ and $\hat{v}_E$, the forcing terms (a) and (b) of (2.23) project onto wavenumbers zero and two to first order. In contrast, A_0 is generally nonzero for the first derivatives of environmental vorticity. Thus, to first order the Self-advection Region equation governing TC propagation is

$$\frac{\partial \zeta_A}{\partial t} + \frac{v_S}{r} \frac{\partial \zeta_A}{\partial \theta} + [u_A - \hat{C} \cos(\theta - \alpha)] \frac{\partial \zeta_S}{\partial r} =$$

$$- v_S \left(\frac{\partial \zeta_E}{\partial y} \bigg|_{r=0} + \beta \right) \cos\theta + v_S \frac{\partial \zeta_E}{\partial x} \bigg|_{r=0} \sin\theta, \tag{2.25}$$

which may be expressed more concisely as

$$\frac{\partial \zeta_A}{\partial t} + \frac{v_S}{r} \frac{\partial \zeta_A}{\partial \theta} + [u_A - \hat{C} \cos(\theta - \alpha)] \frac{\partial \zeta_S}{\partial r} = v_S \beta_{eff} \sin(\theta - \phi). \tag{2.26}$$

The parameter β_{eff} is the magnitude of the environmental absolute vorticity gradient (i.e., an "effective" β) defined by

$$\beta_{eff} \equiv \left[\left(\beta + \frac{\partial \zeta_E}{\partial y} \bigg|_{r=0} \right)^2 + \left(\frac{\partial \zeta_E}{\partial x} \bigg|_{r=0} \right)^2 \right]^{\frac{1}{2}}, \tag{2.27}$$

and ϕ is the direction associated with β_{eff} in degrees from east as defined by

$$\phi \equiv 90^\circ - \arctan\left[\frac{\frac{\partial \zeta_E}{\partial x} \bigg|_{r=0}}{\beta + \frac{\partial \zeta_E}{\partial y} \bigg|_{r=0}} \right]. \tag{2.28}$$

23

b. Wavenumber one Dispersion Region equation

A wavenumber one propagation term does not appear explicitly in (2.20). Nevertheless, it may be anticipated that only wavenumber one processes in the Dispersion Region are important to TC propagation since orthogonality between wavenumbers would preclude the matching of higher order wavenumber solutions in the Dispersion Region to the solutions of the wavenumber one Self-advection Region equation (2.26). In addition, FE and Chan and Williams (1989) have shown that the self-advection flow is predominantly wavenumber one throughout a large region where the Dispersion Region assumption is applicable.

The analysis in Section C.3.a above has already shown that the term $V_E \cdot \nabla \zeta_S$ is to first order a wavenumber two process, and by implication that the term $V_A \cdot \nabla (\zeta_E + f)$ is also to first order a wavenumber two process. Thus, substituting (2.21a,b,c) and (2.22) into (2.20) gives

$$\frac{\partial \zeta_A}{\partial t} + \hat{u}_E \left[\frac{\partial \zeta_A}{\partial r} \cos \theta - \frac{1}{r} \frac{\partial \zeta_A}{\partial \theta} \sin \theta \right]$$

$$+ \hat{v}_L \left[\frac{\partial \zeta_A}{\partial r} \sin \theta + \frac{1}{r} \frac{\partial \zeta_A}{\partial \theta} \cos \theta \right] = v_S \beta_{eff} \sin(\theta - \phi). \tag{2.29}$$

To further simplify (2.29), let $\hat{u}_E$ and $\hat{v}_E$ be approximated by the truncated Taylor series

$$\hat{u}_E(r, \theta) = \left. \frac{\partial \hat{u}_E}{\partial x} \right|_{r=0} r \cos \theta + \left. \frac{\partial \hat{u}_E}{\partial y} \right|_{r=0} r \sin \theta \tag{2.30a}$$

$$\hat{v}_E(r, \theta) = \left. \frac{\partial \hat{v}_E}{\partial x} \right|_{r=0} r \cos \theta + \left. \frac{\partial \hat{v}_E}{\partial y} \right|_{r=0} r \sin \theta, \tag{2.30b}$$

in which $\sin \theta$ and $\cos \theta$ terms have been used in lieu of the phase angle ϕ in (2.24). In substituting (2.30a,b) into (2.29), only terms involving $\sin^2 \theta$ and $\cos^2 \theta$ can contribute to wavenumber one. Retaining only the wavenumber one components of such terms gives

$$\frac{\partial \zeta_A}{\partial t} + \frac{D_E r}{2} \frac{\partial \zeta_A}{\partial r} + \frac{Z_E}{2} \frac{\partial \zeta_A}{\partial \theta} = v_S \beta_{eff} \sin(\theta - \phi), \tag{2.31}$$

where

24

$$D_E \equiv \frac{\partial \hat{u}_E}{\partial x}\bigg|_{r=0} + \frac{\partial \hat{v}_E}{\partial y}\bigg|_{r=0} \quad , \quad Z_E \equiv \frac{\partial \hat{v}_E}{\partial x}\bigg|_{r=0} - \frac{\partial \hat{u}_E}{\partial y}\bigg|_{r=0} . \quad (2.32a,b)$$

Noting that D_E and Z_E represent first-order estimates of environmental divergence and vorticity respectively in the vicinity of the TC, and assuming that $D_E \approx 0$ simplifies (2.31) to

$$\frac{\partial \zeta_A}{\partial t} + \frac{Z_E}{2} \frac{\partial \zeta_A}{\partial \theta} = v_S \beta_{eff} \sin(\theta - \phi) , \quad (2.33)$$

which is to first order the Dispersion Region equation governing TC propagation. Since $Z_E/2$ represents a constant angular velocity for the environmental wind, the second term on the left side of (2.33) represents a gyre-rotating influence consistent with the numerical results of Chan and Williams (1989).

D. SUMMARY AND NONDIMENSIONALIZATION

In summary, two equations have been developed that describe to first order the wavenumber one interaction flow associated with barotropic TC propagation. A transformation to a polar coordinate system moving with the TC and a partitioning of the total flow into symmetric TC, large-scale environment and a TC-environment interaction flow have been employed. A transition radius R_T has been defined inside of which is a Self-advection Region and outside of which is a Dispersion Region where mutual advections by the symmetric and interaction flows are important and unimportant respectively. The wavenumber one interaction flow within the Self-advection Region is governed to first order by

$$\frac{\partial \zeta_{A*}}{\partial t_*} + \frac{v_{S*}}{r_*} \frac{\partial \zeta_{A*}}{\partial \theta} + [u_{A*} - \hat{C}_* \cos(\theta - \alpha)] \frac{\partial \zeta_{S*}}{\partial r_*} = v_{S*} \beta_{eff*} \sin(\theta - \phi) , \quad (2.34)$$

and within the Dispersion Region is governed to first order by

$$\frac{\partial \zeta_{A*}}{\partial t_*} + \frac{Z_{E*}}{2} \frac{\partial \zeta_{A*}}{\partial \theta} = v_{S*} \beta_{eff*} \sin(\theta - \phi) , \quad (2.35)$$

where the asterisk subscripts denote dimensional variables. In all subsequent analysis, the absence of an asterisk will denote nondimensional variables.

This preliminary development is concluded by deriving a nondimensional form of (2.34) and (2.35) by scaling r by the radius of maximum winds (R_M), all velocities by the

25

maximum symmetric wind (V_{M^*}), time by R_{M^*}/V_{M^*} and all vorticities by V_{M^*}/R_{M^*}. The resulting Self-advection Region equation is

$$\frac{\partial \zeta_A}{\partial t} + \frac{v_S}{r}\frac{\partial \zeta_A}{\partial \theta} + [u_A - \hat{C}\cos(\theta - \alpha)]\frac{\partial \zeta_S}{\partial r} = v_S \beta_{eff}\sin(\theta - \phi), \quad (2.36)$$

and the Dispersion Region equation is

$$\frac{\partial \zeta_A}{\partial t} + \frac{Z_E}{2}\frac{\partial \zeta_A}{\partial \theta} = v_S \beta_{eff}\sin(\theta - \phi), \quad (2.37)$$

where

$$\beta_{eff} \equiv \frac{\beta_{eff^*}R_{M^*}^2}{V_{M^*}} \quad \text{and} \quad Z_E \equiv \frac{Z_{E^*}R_{M^*}}{V_{M^*}}. \quad (2.38a,b)$$

26

III. BAROTROPIC VORTEX STABILITY

In this chapter, the specific mechanism responsible for barotropic vortex stability to asymmetric forcing will be identified and analyzed. Since self-advection has been clearly identified to be necessary for this stability to exist in barotropic numerical models (CW), the scope of this chapter will be limited to the Self-advection Region as governed by (2.32). Despite the already simplified form of (2.32), a complete solution for an arbitrary initial condition that includes both the transient and quasi-steadystate responses in TC propagation models is in all likelihood analytically insolvable. As a result, the focus in this chapter will primarily be on the transient adjustment process by transforming (2.32) into the related unforced initial value problem. Equation (2.32) includes only the dominant terms describing the wavenumber one interaction flow associated with barotropic propagation of TC's. To explain the absence of higher wavenumber asymmetries in TC propagation, the following development will address vortex stability to initial asymmetric perturbations of arbitrary wavenumber.

A. MODEL DEVELOPMENT

1. Background

The motivation for the following analytical development is the study of NDBT f-plane Couette flow by Case (1960). He obtained an integral solution for the time evolution of linear perturbations imposed as initial conditions on the NDBT Couette flow, which is a steady, zonally uniform flow with constant latitudinal shear (Fig. 3.1a). Case's result may be interpreted as an infinite summation of a continuum of singular solutions, hereafter referred to as continuous spectrum modes (Pedlosky 1964). For the NDBT f-plane Couette flow problem, this continuous spectrum forms a complete basis, since discrete normal modes are eliminated by the lack of an environmental vorticity gradient. The superposition of these continuous spectrum modes results in a perturbation streamfunction structure that has an algebraic time dependence (i.e., depends on factors involving t to an integer power) as the perturbation is tilted down-shear by the Couette flow. Although the baroclinic Couette flow study of Farrell (1982) showed that initial growth of the perturbation is possible for particular initial conditions, both Farrell and Case showed that the response is asymptotically proportional to t^{-2} for $t \to \infty$, as schematically portrayed in Fig. 3.1a. In terms of instability theory, NDBT f-plane
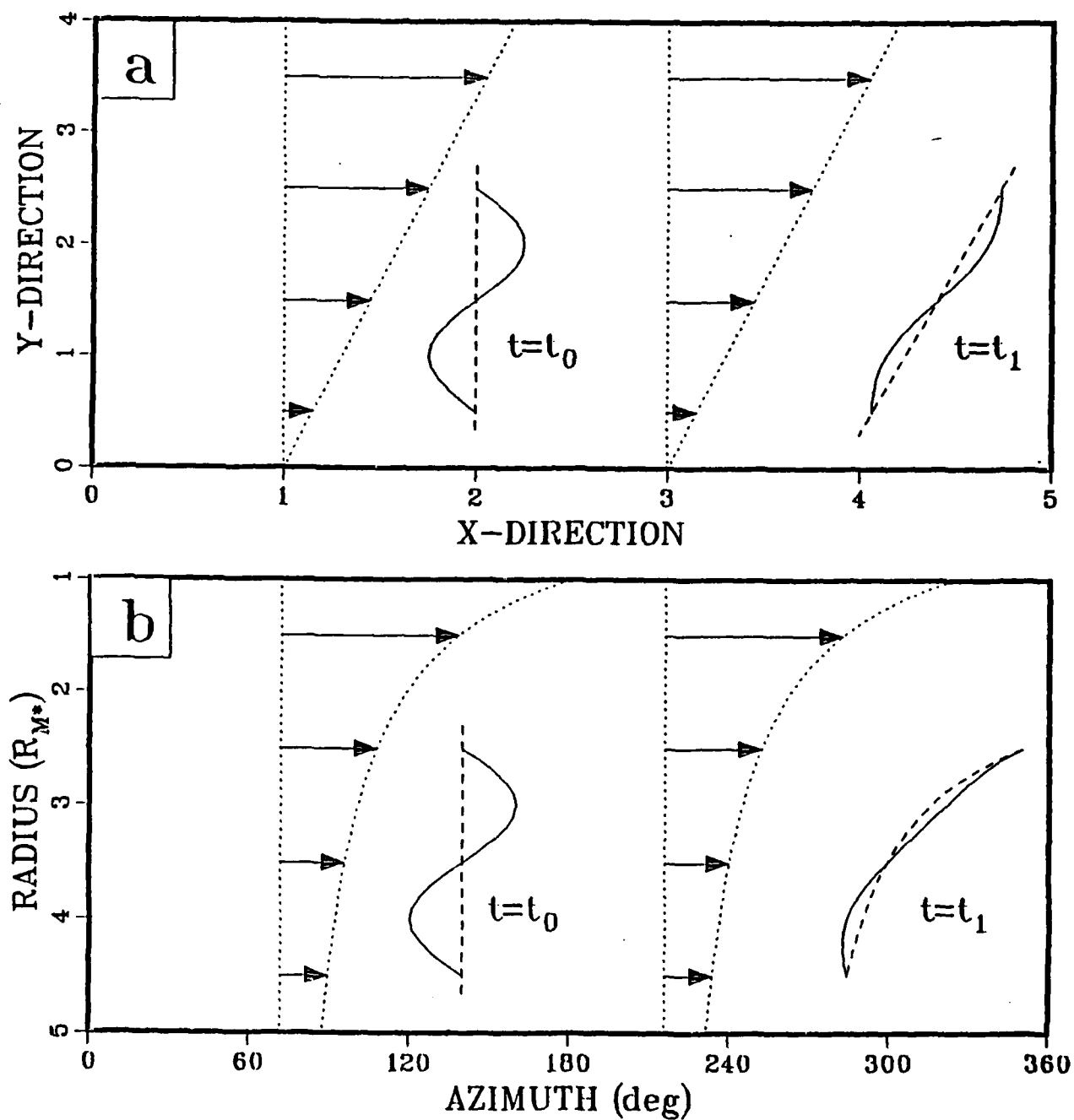
Fig. 3.1   Schematic portrayal of perturbation damping with time due to (a) a meridionally sheared Couette flow, and (b) a radially sheared axisymmetric vortical flow.

Couette flow may be viewed as a barotropically stable "basic state" with respect to linear perturbations.

The NDBT f-plane Couette flow model, as in the Eady or Charney models, may be viewed as an idealization of the response of synoptic disturbances to a particular planetary-scale flow. Along with other limitations, the accuracy of this approach depends on the extent to which synoptic-scale disturbances may be regarded as linear perturbations. In the case of an intense vortex such as a tropical cyclone, such an assumption would be clearly unjustified since the TC winds can be substantially stronger than the environmental flow at quite large distances from the center. However, the large magnitude and nearly circular structure of the TC windfield suggests that a model analogous to NDBT f-plane Couette flow could be developed in a polar coordinate system moving with the center of the TC. In such a model, the axisymmetric component of the TC outside the radius of maximum winds (R_M.) may be regarded as a radially sheared NDBT "basic state" that is time-invariant in the moving reference frame, and the asymmetric component of the vortex may be regarded as a perturbation to the symmetric basic state. If the axisymmetric basic state has constant vorticity, then an initial perturbation can be expected to damp completely as it is tilted in the direction of the symmetric radial shear (Fig. 3.1b). A vortex model based on a constant vorticity basic state and initial perturbations is clearly a special case, and the implications of such approximations will be addressed explicitly below.

2. Model formulation

The analysis of Chapter 1 Section C.3 showed that shearing of symmetric TC vorticity by $\dot{V}_E$ is to first order a wavenumber two process. It is desirable to include this physically-based process in the present analysis by rewriting (2.32) as

$$\frac{\partial \zeta_A}{\partial t} + \frac{v_S}{r}\frac{\partial \zeta_A}{\partial \theta} + [u_A - \hat{C}\cos(\theta - \alpha)]\frac{\partial \zeta_S}{\partial r} =$$

$$-\hat{u}_E\frac{\partial \zeta_S}{\partial r}\cos\theta - \hat{v}_E\frac{\partial \zeta_S}{\partial r}\sin\theta + v_S\beta_{eff}\sin(\theta - \phi),\qquad(3.1)$$

where the first two terms on the right side have been obtained from (2.23). The governing equation for the unforced initial value problem related to (3.1) is

29

$$\frac{\partial \zeta_A}{\partial t} + \frac{v_S}{r}\frac{\partial \zeta_A}{\partial \theta} + [u_A - \hat{C}\cos(\theta - \alpha)]\frac{\partial \zeta_S}{\partial r} = 0. \qquad (3.2)$$

$$\text{(a)} \qquad \text{(b)} \qquad \text{(c)}$$

Equation (3.2) describes the evolution of an asymmetric perturbation initially imposed on a symmetric "basic state" vortex in a quiescent environment and on an f-plane. With the addition of two homogeneous boundary conditions at specified radii, (3.2) becomes the homogenous counterpart to (3.1) over the enclosed domain. Since these equations are linear with respect to the asymmetric perturbation flow, linear differential equation theory can be employed to show that certain relationships exist between the free-perturbation response and the forced-perturbation response. This issue will be specifically addressed in Section D.1 within the context of the free-perturbation behavior illustrated in Section B below.

The advection of perturbation vorticity by the radially variable symmetric flow in term (b) of (3.2) is analogous to the shearing process that causes perturbation damping in the Couette flow model. In addition to manifesting vortex motion through the advection of symmetric vorticity, term (c) permits the propagation of neutral and possibly exponentially growing discrete normal modes on the radial gradient of ζ_S. This term represents a serious obstacle to an analytical solution approach since ζ_S has a strong radial dependence that varies with the particular vortex structure. To facilitate analysis of the damping process associated with term (b), term (c) will be removed by: i) requiring that v_S has a Rankine radial dependence over a horizontal area bounded on the inside by the radius of maximum winds (R_M); and ii) limiting the domain of the imposed perturbation to that region. To facilitate specification of initial conditions in Subsection 3 below, the modified Rankine profile (see Anthes 1982, p. 22) will be used

$$v_S = r^{-X} \qquad r \geq 1. \qquad (3.3)$$

The Rankine profile is the limiting value of (3.3) as $X \to 1$. Substituting (3.3) into (3.2) gives

$$\frac{\partial \zeta_A}{\partial t} + \omega_S \frac{\partial \zeta_A}{\partial \theta} = 0 \qquad r \geq 1 \qquad (3.4a)$$

$$\omega_S \equiv \frac{v_S}{r} = \frac{1}{r^2}, \qquad (3.4b)$$

where ω_s represents the symmetric angular wind.

Choosing v_s to be Rankine not only eliminates any discrete normal mode components from solutions to (3.2), but also may have a significant impact on the continuous spectrum response. Both these issues must be addressed before the results of this model can be used to interpret the numerical studies cited earlier that used non-Rankine vortices. The impact on the continuous spectrum can be assessed by drawing an analogy between (3.2) and NDBT Couette flow on a rotating sphere in the sense that the radial gradient of ζ_s has an influence analogous to the latitudinal variation of the Coriolis parameter. For a β-plane approximation, Kao (1955) and Boyd (1983) have shown that β has no influence on the rate of continuous spectrum damping, but rather causes the continuous spectrum wave to retrogress proportional to β in a manner related to the familiar discrete mode propagation. Because the retrogression is independent of latitude for a constant β, the damping rate depends only on the magnitude of the Couette flow shear. Since the radial gradient of ζ_s is inward in the inner part of a typical vortical flow and decreases rapidly with increasing radius, it is anticipated that a continuous spectrum wave will retrogress (*i.e.*, clockwise for a cyclonic vortex) faster at smaller radii than it would at larger radii. The result would be slower damping since the retrogression would tend to counter the tilting induced by v_s. This effect should be negligible for any modified Rankine vortical flow with $X \approx 1$. In Section C.2, the numerical results of McCalpin (1987) will presented to show that significant perturbation retrogression can occur for a vortex that has a large and highly variable symmetric vorticity gradient. In addition, comparison of the results of this model with those of FE and DM will suggest that the symmetric vorticity gradient of a tangential wind profile that approximates a TC causes only minor slowing of perturbation damping due to variable retrogression. Finally, analysis of McCalpin's results will also suggest that virtually no energy from an initial perturbation projects onto any discrete modes. Thus, the use of a Rankine vortex will be shown to be reasonable for analysis of unforced perturbation responses.

The model may now be solved by defining a perturbation streamfunction

$$\mathbf{V}_A = \mathbf{k} \times \nabla \psi_A \qquad \zeta_A = \nabla^2 \psi_A , \tag{3.5a,b}$$

and assigning homogeneous boundary conditions

$$\psi_A(a, \theta, t) = \psi_A(b, \theta, t) = 0, \tag{3.6a,b}$$

31

where $a = 1$ and b must be chosen to confine the perturbation to the Self-advection Region. Although the analysis of Chapter II defined the outer boundary of the Self-advection Region to be a specific transition radius, here a convenient choice of $b = 10$ will be used. The justification for this approach is that the Self-advection Region depends on perturbation magnitude, and the Self-advection Region in an unforced model can be made arbitrarily large by choosing sufficiently small perturbations. The azimuthal dependence of ψ_A will also be expressed in terms of the complex Fourier series

$$\psi_A(r, \theta, t) = \text{Re}\left\{ \sum_{k=1}^{\infty} \Psi^k(r,t) e^{ik\theta} \right\}. \tag{3.7}$$

Substituting (3.5b) and the kth term of (3.7) into (3.4a) and integrating with respect to time gives

$$\left[\frac{\partial^2}{\partial r^2} + \frac{1}{r}\frac{\partial}{\partial r} - \frac{k^2}{r^2} \right]\Psi^k(r,t) = \zeta_o^k e^{-ikt\omega_s} \tag{3.8a}$$

$$\zeta_o^k \equiv \left[\frac{\partial^2}{\partial r^2} + \frac{1}{r}\frac{\partial}{\partial r} - \frac{k^2}{r^2} \right]\Psi^k(r,0). \tag{3.8b}$$

Substituting (3.7) into (3.6a,b) gives

$$\Psi^k(a,t) = \Psi^k(b,t) = 0, \tag{3.8c,d}$$

where ζ_o^k is the radial structure of the azimuthal wavenumber k component of the initial asymmetric vorticity.

Equations (3.8a-d) constitute a fully specified boundary value problem. The solution may be formally written in terms of a Green's function

$$\Psi^k(r,t) = \int_a^b G(r, \rho)\, \zeta_o^k(\rho)\, e^{-ikt\omega_s(\rho)}\, d\rho. \tag{3.9}$$

Using standard techniques (Case 1960), the Green's function is calculated to be

$$G(r, \rho) = \begin{cases} \dfrac{a^{2k} - r^{2k}}{2kr^k(a^{2k} - b^{2k})}\, (\rho^{k+1} - b^{2k}\rho^{-k+1}) & a \le r \le \rho \\[3ex] \dfrac{b^{2k} - r^{2k}}{2kr^k(a^{2k} - b^{2k})}\, (\rho^{k+1} - a^{2k}\rho^{-k+1}) & \rho \le r \le b \end{cases} \tag{3.10}$$

32

Finally, substituting (3.9) into (3.7) gives

$$\psi_A(r, \theta, t) = \text{Re}\left\{\sum_{k=1}^{\infty}\int_a^b G(r, \rho)\, \zeta_o^k(\rho)\, e^{-ik(\theta - t\omega_S(\rho))}\, d\rho\right\}, \qquad (3.11)$$

which represents a formal solution for the time evolution of the perturbation streamfunction. Although exact solutions to (3.11) do exist for certain initial conditions, the integral generally must be evaluated numerically. A simple trapezoidal scheme will be used.

3. Initial condition specification

To evaluate (3.11), an appropriate functional form and scale for ζ_o^k must be specified. It is not immediately clear what combination of radial and azimuthal dependencies to associate with asymmetries generated by the interaction of a TC with its environmment. The right side of (3.1) is used for this purpose by writing

$$\frac{\partial \zeta_A}{\partial t} \propto v_S\beta_{eff}\sin(\theta - \phi) - \hat{u}_E\frac{\partial \zeta_S}{\partial r}\cos\theta - \hat{v}_E\frac{\partial \zeta_S}{\partial r}\sin\theta$$

$$+ \hat{c}_X\frac{\partial \zeta_S}{\partial r}\cos\theta + \hat{c}_Y\frac{\partial \zeta_S}{\partial r}\sin\theta, \qquad (3.12)$$

where $\hat{c}_x \equiv \hat{C}\cos\alpha$ and $\hat{c}_y \equiv \hat{C}\sin\alpha$ are the zonal and meridional components of the TC propagation velocity respectively. Advection by $\hat{C}$ has been included from the left side of (3.1) since the propagation induced by u_A is also an asymmetry-inducing influence (cf. Willoughby 1988). Since asymmetries associated with the two environmental shearing terms will differ only with respect to phase, which is unimportant in the unforced response analysis, only the first term will be utilized here. Applying similar logic to the two propagation terms in (3.12) results in the simplified form

$$\frac{\partial \zeta_A}{\partial t} \propto v_S\beta_{eff}\sin(\theta - \phi) - \hat{u}_E\frac{\partial \zeta_S}{\partial r}\cos\theta + \hat{c}_X\frac{\partial \zeta_S}{\partial r}\cos\theta. \qquad (3.13)$$

$$\text{(a)} \qquad\qquad \text{(b)} \qquad\qquad \text{(c)}$$

To determine the spatial structure of the forcing terms in (3.13), the radial gradient of symmetric vorticity first is written in terms of (3.3). Now a Rankine profile ($X = 1$) has zero vorticity as desired to delete term (c) from (3.2). As noted in the Section A.2 above, a small perturbation away from ($X = 1$) may also be considered as a valid

33

model extension since the radial shear of v_S would be essentially unchanged, and the associated damping should be little affected by the small radial gradient of ζ_S that would be introduced. Thus, using (3.3) with $X \approx 1$ gives

$$\frac{\partial \zeta_S}{\partial r} \approx \frac{X^2 - 1}{r^3} . \tag{3.14}$$

Second, let $\hat{u}_E$ be approximated by a truncated Taylor series expansion about the present position of the symmetric cyclone center

$$\hat{u}_E(y) = S_E y = S_E r \sin\theta , \tag{3.15a}$$

$$S_E \equiv \left. \frac{\partial \hat{u}_E}{\partial y} \right|_{y=0} \tag{3.15b}$$

where S_E represents the nondimensionalized linear shear component of the environmental wind, and any zonal dependence of $\hat{u}_E$ has been ignored due to the phase argument mentioned above.

Considering only term (a) of (3.13), substituting (3.3) gives

$$\frac{\partial \zeta_A}{\partial t} \propto \frac{\beta_{eff}}{r} \sin(\theta - \phi) , \tag{3.16}$$

which represents the generation of a wavenumber one asymmetry from the advection of environmental absolute vorticity by the symmetric vortex. Such asymmetries represent the large gyres that have been identified in numerical models (FE) and in observations (Chan 1986). An initial condition with equivalent spatial structure (hereafter referred to as a "vorticity-induced asymmetry") for use in this unforced model would be

$$\zeta_o^k(r) = \frac{-\varepsilon}{r} \qquad k = 1 \tag{3.17}$$

$$\varepsilon \equiv \frac{Z_{A*}}{V_{M*}/R_{M*}} , \tag{3.18}$$

where a poleward gradient of absolute vorticity has been assumed ($\phi = 90°$), and Z_{A*} represents a scale for the perturbation vorticity that remains to be specified.

34

Considering only term (b) of (3.13), substituting (3.14) and (3.15a) gives

$$\frac{\partial \zeta_A}{\partial t} \propto (1 - X^2)\frac{S_E}{2r^2}\sin 2\theta , \qquad (3.19)$$

in which the identity $2\sin\theta\cos\theta \equiv \sin 2\theta$ has been used. The right side of (3.19) represents the generation of a wavenumber two asymmetry due to linear shearing of symmetric vorticity by the TC-relative environmental wind. An initial condition with equivalent spatial structure (hereafter referred to as a "shear-induced asymmetry") for use here is

$$\zeta_o^k(r) = \frac{-i\varepsilon}{r^2} \qquad k = 2 , \qquad (3.20)$$

where it is has been assumed that S_E is positive corresponding to anticyclonic shear equatorward of the subtropical ridge.

Considering only term (c) of (3.13), substituting (3.14) gives

$$\frac{\partial \zeta_A}{\partial t} \propto (X^2 - 1)\frac{\hat{c}_X}{r^3}\cos\theta . \qquad (3.21)$$

An initial condition with equivalent spatial structure (hereafter referred to as a "motion-induced asymmetry") for use here is

$$\zeta_o^k(r) = \frac{\varepsilon}{r^3} \qquad k = 1 , \qquad (3.22)$$

where it is assumed that $\hat{c}_X$ is negative, which corresponds to the generally westward movement of TC's relative to environmental steering documented by composite studies (Chan and Gray 1982; Holland 1984). In both (3.20) and (3.22), it has been assumed that X is slightly less than one so that the symmetric TC flow has cyclonic vorticity.

It is inappropriate in this simple model to assign an individual perturbation vorticity scale Z_A to each of the above initial conditions based on the scales of the associated forcing terms. Instead, all but one of the following model solutions will use a value for Z_A such that $\varepsilon = 0.1$ to facilitate analyzing the dependence of vortex stability on perturbation spatial structure. The radial structures of the four initial perturbations defined above are shown in Fig. 3.2.
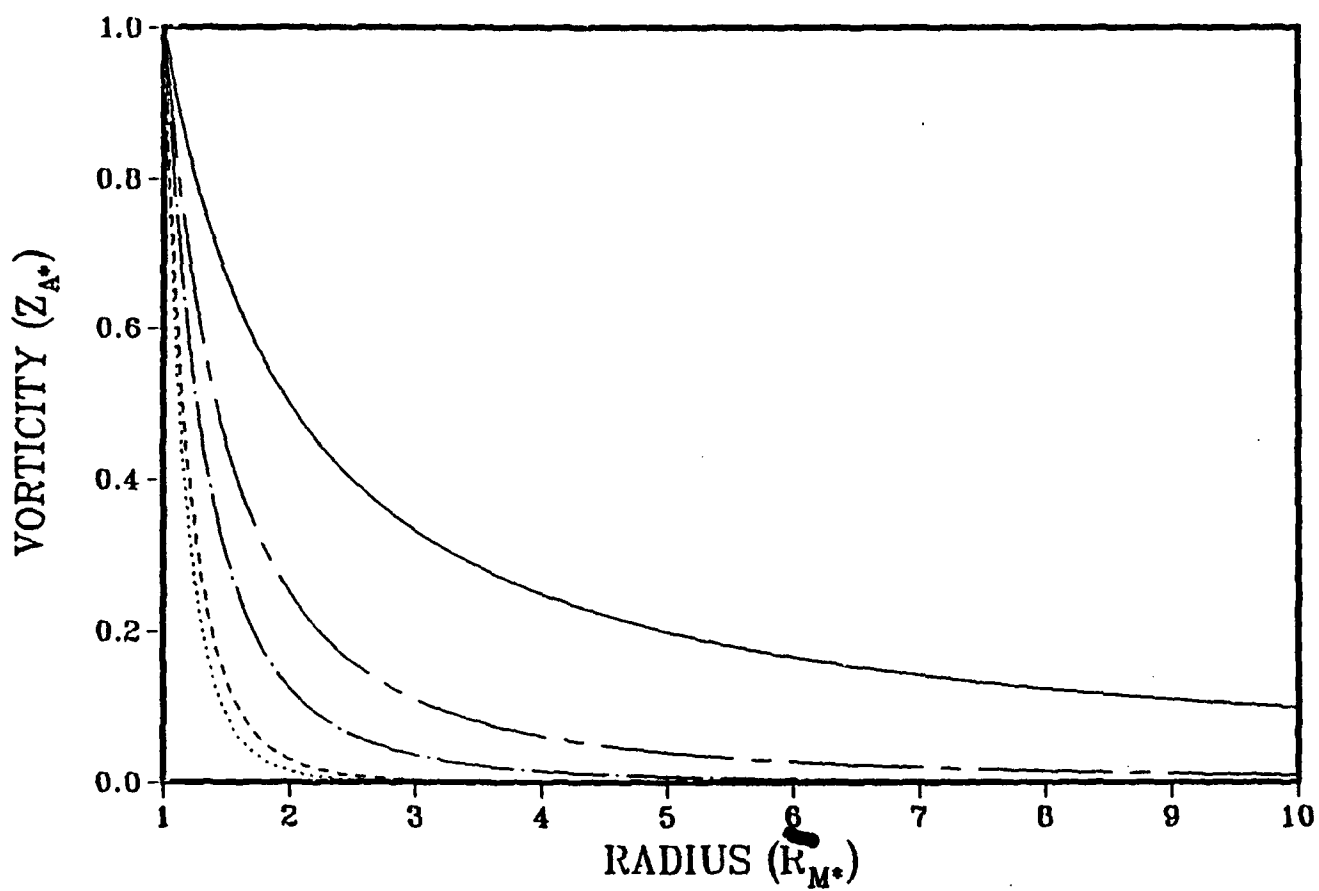
Fig. 3.2 Radial dependence of initial perturbation vorticity (Z_A, ζ_o^k) for convection-induced (k = 2, dot; k = 1, dash), motion-induced (chaindot), shear-induced (chaindash) and β-induced (solid) asymmetries.

B. MODEL RESULTS

1. Perturbation damping

Before numerically evaluating (3.11) using the initial conditions developed above, it is useful to obtain exact solutions by choosing initial conditions of the form

$$\zeta_o^k(r) = \frac{\varepsilon}{r^{k+4}} . \tag{3.23}$$

An asymmetry of this type may be viewed as an approximation to the wavenumber k component of a perturbation produced by localized asymmetric convection in a TC eyewall cloud (hereafter refered to as a "convection-induced asymmetry"). Initial condition (3.23) for $k = 1$ and $k = 2$ is also shown in Fig. 3.2, and results in solutions to (3.11) of

$$\psi_A(r, \theta, t) = \frac{\varepsilon}{4t^2} \left[\frac{a^2(r^2 - b^2)}{r(a^2 - b^2)} \cos(\theta - t/a^2) \right.$$

$$\left. + \frac{r^2(b^2 - a^2)}{r(a^2 - b^2)} \cos(\theta - t/r^2) + \frac{b^2(a^2 - r^2)}{r(a^2 - b^2)} \cos(\theta - t/b^2) \right]. \tag{3.24}$$

and

$$\psi_A(r, \theta, t) = \frac{\varepsilon}{16t^2} \left\{ \frac{a^4(r^4 - b^4)}{r^2(a^4 - b^4)} \left[\frac{1}{a^2} \cos 2(\theta - t/a^2) + \frac{1}{2t} \sin 2(\theta - t/a^2) \right] \right.$$

$$+ \frac{r^4(b^4 - a^4)}{r^2(a^4 - b^4)} \left[\frac{1}{r^2} \cos 2(\theta - t/r^2) + \frac{1}{2t} \sin 2(\theta - t/r^2) \right] \tag{3.25}$$

$$\left. + \frac{b^4(a^4 - r^4)}{r^2(a^4 - b^4)} \left[\frac{1}{b^2} \cos 2(\theta - t/b^2) + \frac{1}{2t} \sin 2(\theta - t/b^2) \right] \right\}$$

respectively.

Both (3.24) and (3.25) damp algebraically with time as is characteristic of continuous spectrum mode solutions. It should be noted that the wavenumber two perturbation damps four times as rapidly as the wavenumber one perturbation. which suggests that the damping rate is proportional to the square of perturbation wavenumber. This result is analogous to the dependence of damping on the perturbation zonal wavenumber for plane Couette flow (Case 1960). The evolution of (3.24) and (3.25) over a 2 hour period are shown in Fig. 3.3a-c and Fig. 3.3d-f respectively. Unless otherwise
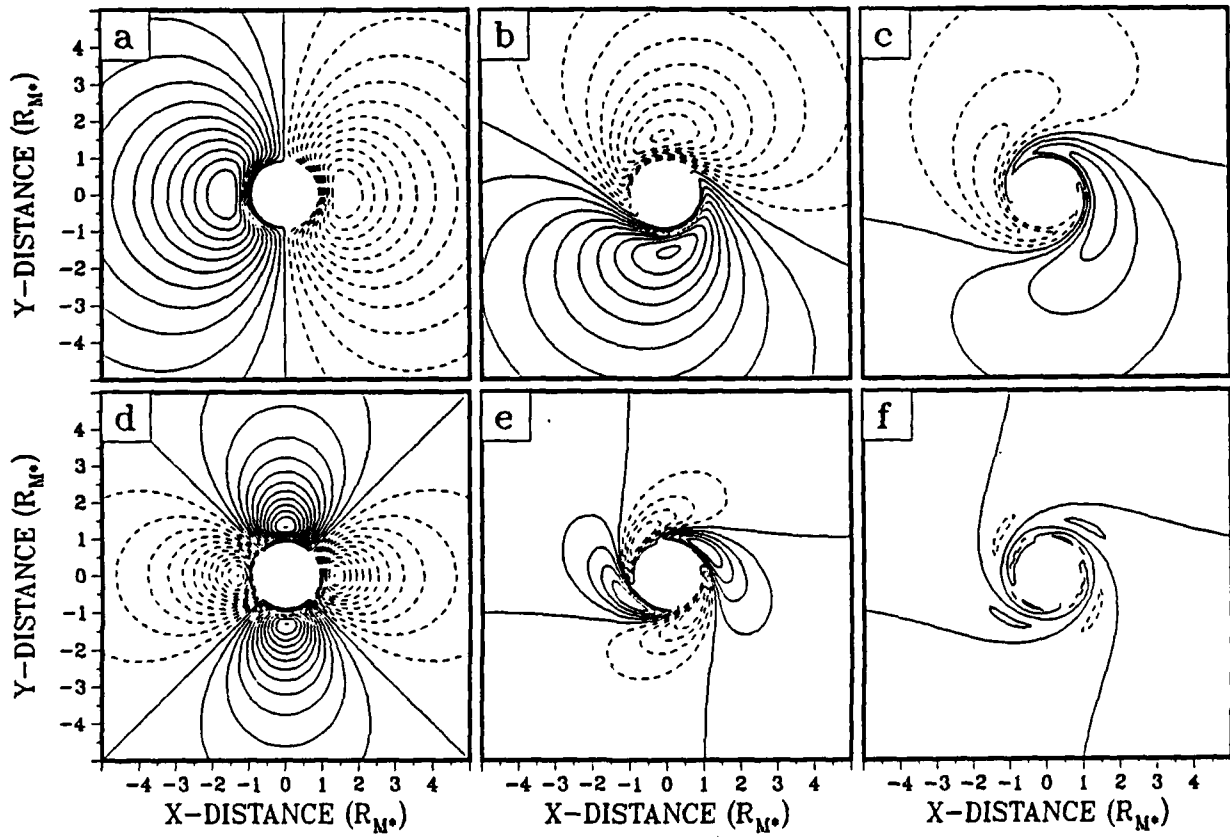
Fig. 3.3 (a)-(c) Perturbation streamfunction (solid, positive; dashed, negative) for a $k = 1$ convection-induced asymmetry at $t = 0$, 1 and 2 hours respectively. Contour interval is $9.6 \times 10^2 \, m^2/s$. (d)-(f) Same as (a)-(c) except for a $k = 2$ convection-induced asymmetry, and a contour interval of $4.3 \times 10^2 \, m^2/s$.

38

noted, all illustrated solutions use the following parameter specifications: $a = 1$, $b = 10$, $V_M = 50$ m/s, $R_M = 50$ km and $\varepsilon = 0.1$. The contour interval is the same for each row of panels to show clearly the damping process. This comparison emphasizes the strong dependence of the damping process on perturbation wavenumber, and also clearly illustrates how the radial variability of v_s tilts the perturbations downshear.

The perturbation streamfunctions for the motion-induced and shear-induced asymmetries (not shown) undergo a similar, but slower shearing and damping process. A quantitative comparison of damping rates is facilitated by Fig. 3.4a, which shows the decay of perturbation kinetic energy with time for each of the four cases. Although perturbations of the same wavenumber damp at nearly the same rate initially, the damping rates quickly diverge. As will be shown in Section C.1, this property is due significant differences in the radial dependences of the initial conditions, e.g., r^{-6} for a wavenumber two convection-induced asymmetry as compared to r^{-2} for the shear-induced asymmetry. Thus, NDBT vortex stability to asymmetric perturbations is quite sensitive to the radial as well as azimuthal structure of the perturbation.

The kinetic energy decay for a vorticity-induced asymmetry is shown in Fig. 3.4b. Perturbation kinetic energy decays by approximately 80% in 24 h, which agrees quite well with the adjustment period observed in the NDBT numerical models of TC motion cited earlier. The much slower damping rate in Fig. 3.4b is consistent with the discussion in the preceding paragraph since the perturbation vorticity associated with a vorticity-induced asymmetry decreases significantly slower with increasing radius than any of the previous initial conditions (Fig. 3.2). The evolution of both the total and perturbation streamfunction components over a 36-hour period is shown in Fig. 3.5. The value of ε has been increased to 0.5 in Fig. 3.5 to emphasize how an initially perturbed NDBT vortex is restored to axisymmetry. By 8 h, the inner part of the vortex has already regained an essentially axisymmetric structure (Fig. 3.5b), while the outer vortex remains appreciably distorted. No analogy to this behavior exists in horizontal plane Couette flow, since the linear shear in that model renders the damping process independent of latitude.

2. Influence of boundary conditions

Boundary conditions (3.6a,b) were chosen to facilitate development of the model and are clearly nonphysical. Thus, it is important to determine the extent to which the boundary conditions may have influenced the results presented above. Two aspects of this problem must be addressed.
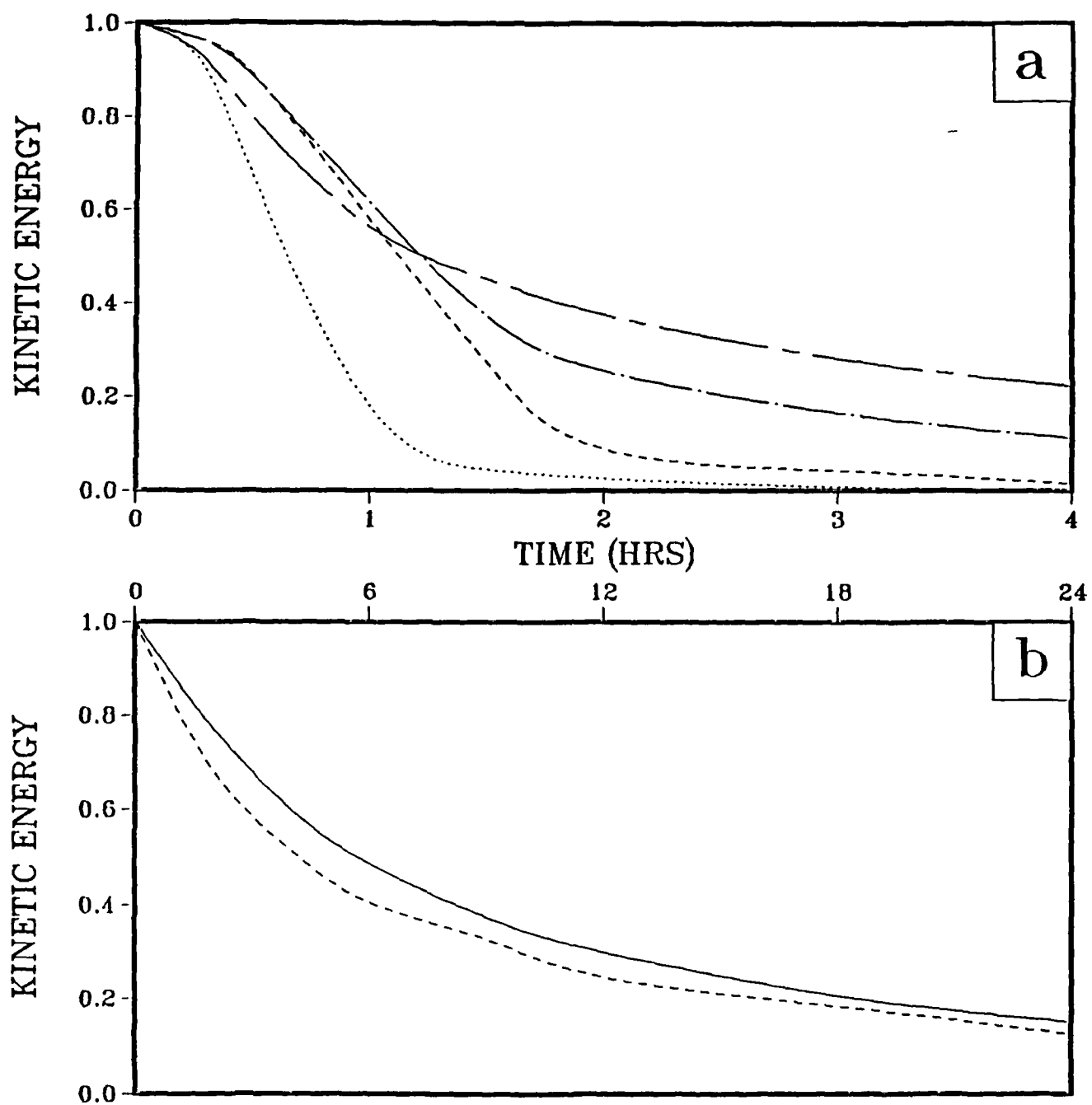
Fig. 3.4 (a) Decay of perturbation kinetic energy (normalized by initial value) with time for convection-induced (k = 2, dot; k = 1, dash), motion-induced (chaindot) and shear-induced (chaindash) asymmetries. (b) Same as (a), except for a β-induced (solid) and a modified β-induced (dash) asymmetry.
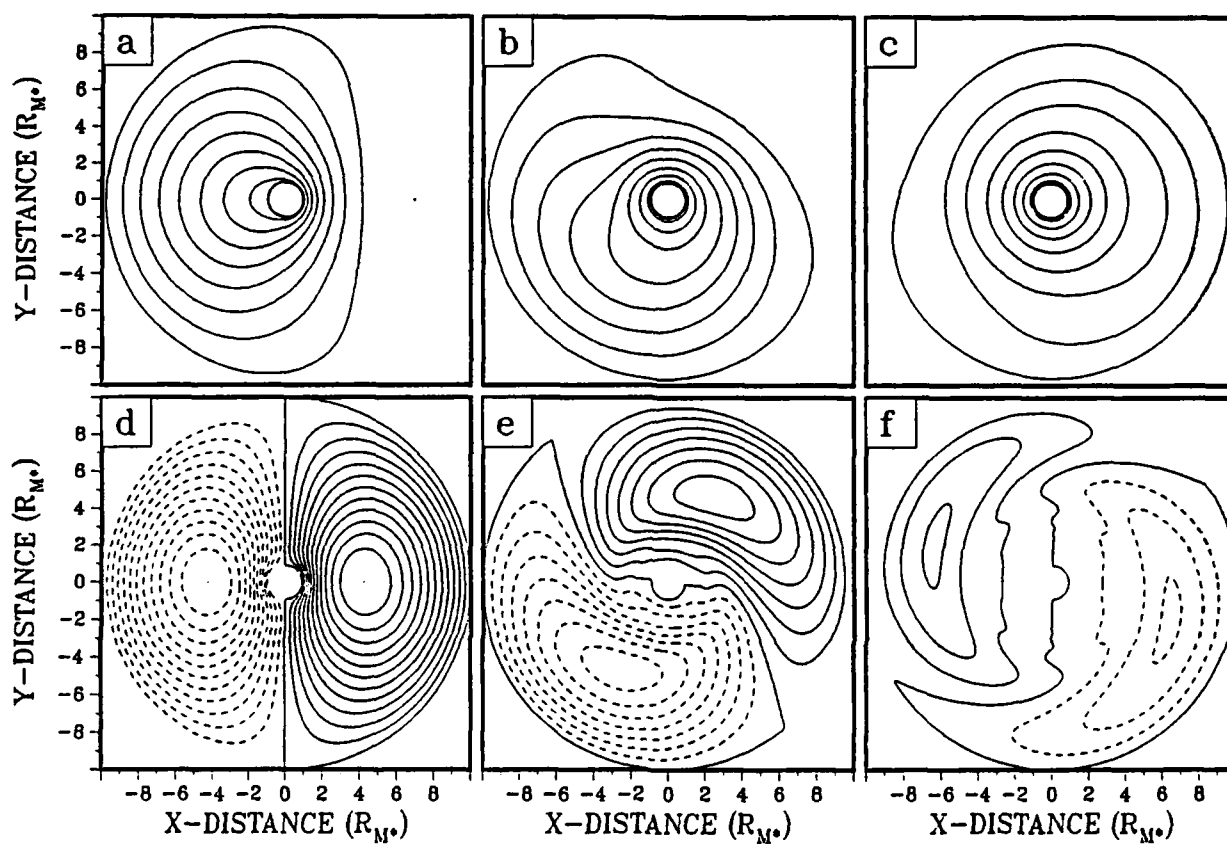
Fig. 3.5 (a)-(c) Perturbation plus symmetric streamfunction for a β-induced asymmetry at $t = 0$, 8 and 36 hours respectively. Contour interval is $7.4 \times 10^5 \ m^2/s$. (d)-(f) Same as (a)-(c) except showing just the perturbation streamfunction (solid, positive; dashed, negative), and using a contour interval of $1.7 \times 10^5 \ m^2/s$.

First, boundary influences will become increasingly significant with time if there is a tendency for perturbation energy to propagate radially and cause a concentration at either boundary. This problem may be formally addressed by considering

$$\zeta_A(r, \theta, t) = \mathrm{Re}\{\zeta_o^k(r)e^{ik(\theta - \omega_s t)}\},\qquad(3.26)$$

which is obtained by substituting (3.5b) and (3.8a,b) into the Laplacian of (3.7). Equation (3.26) indicates that perturbation vorticity is conserved following the symmetric angular wind, which is a purely azimuthal motion. This result depends on the model being linear and the symmetric vortex being Rankine, but does not depend on boundary conditions. Thus, no mechanism exists in this model to propagate perturbation energy radially, nor does an examination of Fig. 3.3 or 3.5 indicate that such a process is taking place.

Second, the presence of the inner domain boundary at the location of maximum perturbation vorticity may produce nonphysical results. A nonzero inner boundary was used because a Rankine vortex is singular at the origin. The inner boundary may be moved to the origin if the singularity is removed by modifying the wind profile to be solid body rotation at all radii less than R_M. Recall that the choice of radial structure for the various initial perturbations depends on the symmetric vortex. Thus, the radial structure for a vorticity-induced asymmetry associated with a Rankine vortex altered as just suggested would be

$$\zeta_o^k(r) = \begin{cases} -r & 0 \leq r < 1 \\ \dfrac{-1}{r} & 1 \leq r \leq b \end{cases}.\qquad(3.27)$$

Fig. 3.4b shows that the kinetic energy for such an initial perturbation decays at virtually the same rate as the original vorticity-induced asymmetry.

Modifying the symmetric wind as described above causes the radial gradient of ζ_s to be singular at $r = 1$. This singularity is equivalent to a large radial gradient of vorticity, which would tend to cause clockwise retrogression and somewhat slower damping of the continuous spectrum solution as discussed earlier. Although the present model cannot give a quantitatively precise solution for the response of a perturbation to a Rankine vortex with solid body inner rotation, the response of the model to (3.27) is useful for demonstrating that solutions are not unduly sensitive to the location of the inner boundary.

C. MODEL INTERPRETATION

1. The stabilization mechanism

Within the context of fluid dynamical instability theory, the present stability of a linear perturbation with respect to some "basic state" may be assessed by computing the domain-averaged local time tendency of perturbation energy. For the particular boundary conditions used in this model, the familiar NDBT result is that domain-averaged perturbation kinetic energy must be presently increasing (decreasing) with time if the perturbation tilts against (with) the horizontal shear of the basic state. Such a result is readily obtainable for this model by substituting (3.5b) into (3.4a), multiplying by ψ_A, integrating over the domain, and performing a number of integrations by parts. Using (3.5a), the result may be expressed as

$$\frac{\partial E}{\partial t} = - \int_a^b \overline{(v_A u_A)} \frac{\partial \omega_S}{\partial r} r^2 \, dr \tag{3.28a}$$

$$E \equiv \int_a^b \frac{1}{2} \overline{(u_A^2 + v_A^2)} r \, dr \tag{3.28b}$$

$$\overline{(\ )} \equiv \frac{1}{2\pi} \int_0^{2\pi} (\ ) \, d\theta . \tag{3.28c}$$

Equation (3.28a) is analogous to the familiar result for stationary cartesian coordinates (e.g., Farrell 1987), except that in this case it is the shear of the axisymmetric *angular* wind that controls the energy transfer process. In (3.28a), a positive correlation develops between the perturbation momentum flux and the symmetric angular wind shear when initially "upright" perturbations are tilted downshear. Since the radial shear of ω_S is negative for a cyclone, the average perturbation momentum flux must also be negative. This flux represents an inward transport of cyclonic momentum that tends to accelerate the symmetric "basic state" at the expense of asymmetric perturbation kinetic energy.

Because the analysis thus far has been strictly linear, the symmetric vortex has been regarded as steady in the moving reference frame. However, using the azimuthal momentum equation and (3.28), the influence of perturbation momentum flux on the symmetric basic state is described by

$$\frac{\partial v_S}{\partial t} = - \overline{(u_A v_A)} . \tag{3.29}$$

This expression may be evaluated to lowest order in ε using (3.11) and (3.26), and then integrated with respect to time to give

$$\Delta v_S = \frac{1}{2r}\, \zeta_o^k(r) \int_a^b \frac{G(r,\rho)\, \zeta_o^k(\rho)}{\omega_S(r) - \omega_S(\rho)}\, [\cos\, kt(\omega_S(\rho) - \omega_S(r)) - 1]\, d\rho\,, \quad (3.30a)$$

$$\Delta v_S(r,t) \equiv v_S(r,t) - v_S(r,0)\,. \quad (3.30b)$$

The time evolution of Δv_S is illustrated in Fig. 3.6 using the same initial condition as in Fig. 3.5, except that ε has been reduced to 0.1, which corresponds to a more realistic asymmetric windspeed of approximately 2.8 m/s near the domain center. Although a nearly complete transfer of perturbation kinetic energy occurs by 48 h, the majority of the transfer has taken place by 24 h as anticipated from the damping rate in Fig. 3.4b. The domain-averaged sign of Δv_S is positive as required, but a slight decrease is evident for $r \gtrsim 6$. Interestingly, the radius at which Δv_S changes sign corresponds precisely with the maximum in perturbation streamfunction at any time (see Fig. 3.5f). It is also evident that the energy transfer begins initially at small radii and spreads outward with time. This aspect will be explained later in this subsection.

The momentum flux asssociated with the convection-induced, motion-induced and shear-induced asymmetries (not shown) had a similar impact on the symmetric basic state, with the changes in Δv_S becoming smaller, more concentrated at small radii and occurring over a shorter period of time for an initial condition that decreases more rapidly with radius. The extent to which perturbation flux tends to alter the basic state is one measure of model linearity. Thus, the results here show that the assumptions made in Section A.3 ($\varepsilon \leq 0.1$, $r \leq 10$) were reasonable. This demonstration of how perturbation flux transfers energy to the symmetric vortex will be particularly useful in Section D.2 for understanding how a barotropic vortex achieves a quasi-steady asymmetric structure in the presence of steady asymmetric forcing.

The availability of exact solutions to this model permits valuable insights into the local dynamics of the stability process that are not readily evident from the "domain-averaged" analysis conducted above. Note that by virtue of the identity

$$\nabla^2 \left[r^{\pm k} e^{ik(\ell + \phi(t))} \right] \equiv 0\,, \quad (3.31)$$

44
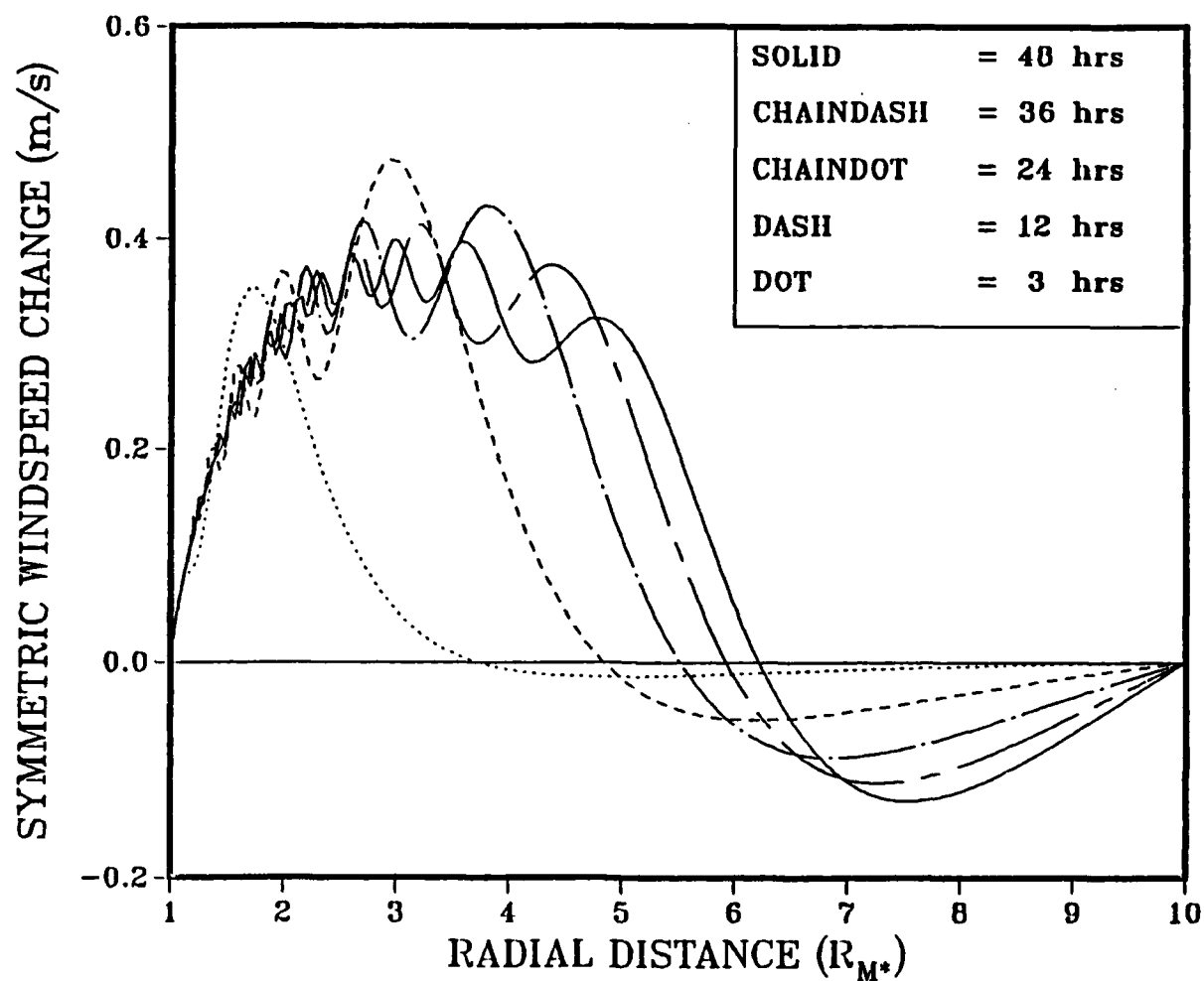
Fig. 3.6 Change in symmetric vortex windspeed with time (see legend) as a function of radius due to a convergence of momentum flux associated with a β-induced asymmetry. The windspeed of the mean symmetric vortex is 50 m/s at the radius of maximum winds and decreases with inverse dependence on radius to 5 m/s at ten times the radius of maximum winds.

the first and third terms on the right side of (3.24) and (3.25) have no vorticity, and thus are necessary solely to satisfy the boundary conditions. Therefore, substituting either of the exact solutions into (3.5b) results in a form

$$\zeta_A(r, \theta, t) = \nabla^2 \operatorname{Re} \left\{ A(r,t) \, e^{ik(\theta - \omega_S t)} \right\}, \tag{3.32}$$

where $A(r,t)$ is an appropriate amplitude function based on the second term on the right side of either (3.24) or (3.25). Since ω_S is a function of radius, (3.32) will include an explicit time dependence in some of the terms associated with radial derivatives of the Laplacian. For sufficiently large t, only the term possessing the highest order explicit dependence on t needs to be retained, which gives

$$\zeta_A(r, \theta, t) \approx - \operatorname{Re} \left\{ \left[\left(kt \frac{\partial \omega_S}{\partial r} \right)^2 + \left(\frac{k}{r} \right)^2 \right] A(r,t) e^{ik(\theta - \omega_S t)} \right\}, \tag{3.33}$$

in which the term generated by the azimuthal derivatives in the Laplacian has been retained for comparison. Note that the expression k/r inside the brackets represents the inverse of the perturbation azimuthal length scale at radius r. If the first term in brackets is treated similarly, and the length scales are defined as

$$L_\theta = \frac{r}{k} \qquad L_R = \frac{1}{kt \dfrac{\partial \omega_S}{\partial r}}, \tag{3.34a,b}$$

then (3.33) may be expressed as

$$\zeta_A(r, \theta, t) \approx - \operatorname{Re} \left\{ \left[\frac{A(r,t)}{L_R^2} + \frac{A(r,t)}{L_\theta^2} \right] e^{ik(\theta - \omega_S t)} \right\}. \tag{3.35}$$

The local dynamics of the damping process may be explained in terms of (3.35) as follows. Under the influence of the radial shear of ω_S, the radial length scale of the perturbation at any point in the domain exhibits an inverse dependence on t, while the azimuthal length scale remains unaltered. Since this model conserves perturbation vorticity, the left side of (3.35) maintains a constant magnitude. A continuing decrease in L_R thus requires the amplitude of the perturbation streamfunction to decrease proportional to r^2 so that the right side of (3.35) maintains a constant magnitude. This constraint may also be argued conceptually from the viewpoint that vorticity is a velocity change over some length scale. If the length scale is decreasing, then the velocity

change must also decrease to conserve vorticity. This process is shown in Fig. 3.7 which is a time sequence of perturbation vorticity using (3.26) with a vorticity-induced initial asymmetry. The reduction in the radial length scale due to the shearing process is clearly illustrated by the decreasing radial spacing of the isolines of vorticity with time.

The results in Section B.1 show that vortex stability to asymmetric perturbations is strongly dependent on the spatial structure of the initial perturbation. From (3.34b), this behavior can be associated with two factors that influence L_R's inverse dependence on t. The first is the perturbation wavenumber k, which results in perturbations with a higher wavenumber damping faster than those with a low wavenumber, if the radial structures are similar. This is the case for the wavenumber one and two convection-induced asymmetries (Fig. 3.3), which differ little in radial dependence (Fig. 3.2). The second factor in (3.34b) is the radial shear of the symmetric angular wind, which is strongly dependent on radius. Thus, the shearing process reduces L_R much more rapidly in the inner part of the vortex relative to the outer regions, which explains why the perturbed vortex in Fig. 3.5b has achieved an essentially axisymmetric state in the inner region while the outer region remains distorted. This shearing distribution also explains why the speed of the damping process depends on the radial structure of the perturbation vorticity. An initial perturbation that decreases in magnitude more slowly with increasing radius has a greater fraction of its kinetic energy at larger radii than does a perturbation that decreases rapidly with radius. Since the radial shear of ω_S decreases rapidly with radius, it will take longer to transfer the same amount of kinetic energy from the first perturbation. Nevertheless, energy transfer still takes place rapidly near the inner boundary. This is illustrated in Fig. 3.6 since the symmetric vortex windspeed increases almost immediately near the inner boundary and is followed by speed increases at larger radii with increasing time.

2. Verification with independent numerical results

Insight into the impact of using a Rankine basic state vortex in this model can be gained by comparing the present results with a similar model that uses a non-Rankine vortex. McCalpin's (1987) quasi-geostrophic reduced-gravity numerical model of an initially perturbed ocean eddy will be used for this purpose. The difference between the dynamical frameworks of the two models is not a significant issue since this NDBT model can be readily reformulated as a quasi-geostrophic reduced-gravity model. The result is that ζ_A is replaced by perturbation potential vorticity in (3.4a) and that v_S becomes a K_1 exponential Bessel function having zero potential vorticity.
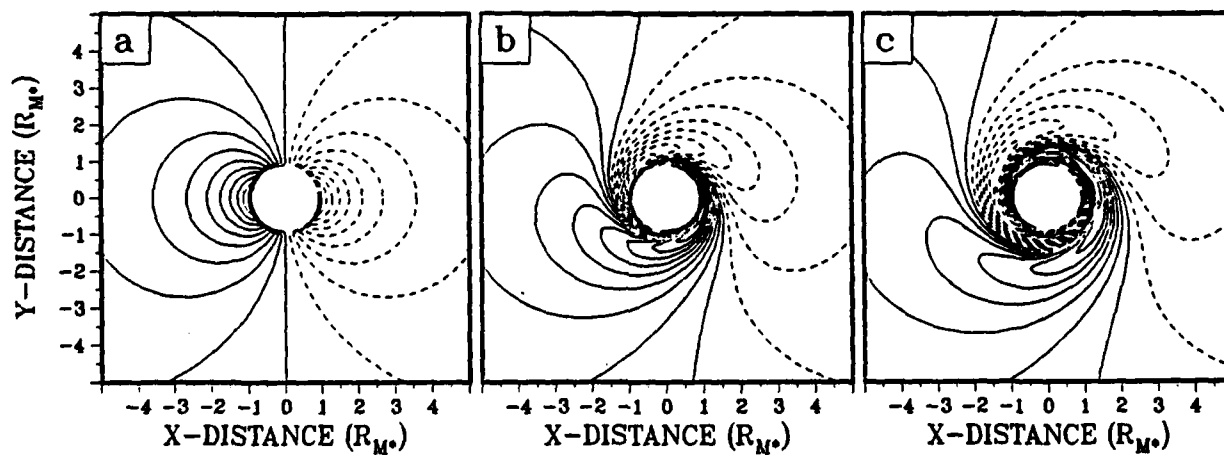
Fig. 3.7 (a)-(c) Perturbation vorticity (solid, cyclonic; dashed, anticyclonic) for a β-induced asymmetry at $t = 0$, 1 and 2 hours respectively. Contour interval is $9.1 \times 10^{-6} s^{-1}$.

The main difficulty in comparing the two models is McCalpin's choice of Gaussian radial dependence for both the symmetric and asymmetric components of the eddy. Additionally, McCalpin characterized the damping of perturbation energy in terms of an exponential decay time scale, whereas the continuous spectrum response in this model is algebraic in time. Nevertheless, if the convection-induced asymmetries used here are considered to be roughly equivalent to Gaussian perturbations, then McCalpin's wavenumber two decay time scale of 1.5 times the symmetric flow circulation time (at the radius of maximum velocity) may be compared to the 0.8 h "exponential" time scale given by Fig. 3.4a for a wavenumber two convection-induced asymmetry. Using the 1.75 h circulation time for v_{s^*} at $r_* = R_{M^*}$ in this model, the damping rate here is approximately 3 times faster than in McCalpin's model. This difference is not surprising since a Gaussian vortex has an extremely strong and rapidly decreasing radial gradient of symmetric vorticity just outside R_{M^*}, that should cause a significant, radially variable retrogression that can substantially reduce the rate of perturbation tilting by the symmetric flow. This assertion is supported by McCalpin's observation that perturbations were advected around the eddy at only 20% of the maximum tangential velocity. Tangential winds in a TC decay much more slowly with increasing radius than a Gaussian vortex, and thus will have a symmetric vorticity gradient that is comparatively much smaller and decreases more slowly with radius. Thus, it may be reasonably argued that the damping rates of this model are more representative of those associated with typical TC wind profiles. This argument is also suported by the good agreement between the 24 h adjustment period cited in NDBT numerical studies of TC motion on a β-plane and the kinetic energy transfer rates in Figs. 3.4b and 3.6. With regard to the influence of perturbation wavenumber, McCalpin's wavenumber three decay time scale is 2.6 times shorter than the wavenumber two time scale, which indicates a wavenumber dependence similar to that above.

Earlier it was noted that choosing Rankine symmetric vortex excludes potentially important discrete normal modes. When McCalpin's model was run on an f-plane, approximately 99% of the energy initially present in the imposed perturbation was transferred to the symmetric component. Such a response indicates that virtually no perturbation energy was projected onto any discrete normal modes that might exist due to the presence of a symmetric vorticity gradient. Thus, the exclusion of discrete mode processes by the choice of a Rankine vortex for this model appears justifiable for transient perturbation analysis. However, this does not rule out the potential importance of discrete modes in the steady-state component of a forced perturbation response.

D. MODEL APPLICATION

1. Free versus forced system relationships

The motivation for the present modeling approach has been to exploit the analytical tractability of an unforced model for analyzing transient responses. The closed-form solutions obtained via this technique have permitted a rigorous and illuminating analysis of the perturbation damping process. To apply these results to the forced problem, it is necessary to establish what aspects of a forced-perturbation response can be reasonably inferred from the free-perturbation response.

First, it can be shown by superposition that the full solution of a linear partial differential equation with steady forcing and nonhomogeneous boundary conditions can be represented as a sum of a steady-state part that satisfies the original equation with forcing and boundary conditions, and a transient part that satisfies the homogeous equation and that results from an initial condition that is different from the steady-state solution. Implicit in such a partitioning of the full solution is the assumption that the dynamical system actually supports a non-trivial steady-state condition. In the case of vorticity-induced asymmetries, the NDBT numerical study of FE indicates that the asymmetric component of the vortex does tend toward a steady-state condition over the region where the symmetric vortex is significantly stronger than the asymmetric component (i.e., over the region where the present linear model is valid). Although DM did not comment on vortex asymmetries, his illustration of a slowly varying TC motion track after 24 h indicates that vortex asymmetries associated with steady, spatially variable environmental winds also tend toward a quasi-steady-state. Thus, the properties (*e.g.*, damping time scales, azimuthal wavenumber dependence, etc.) of the unforced transient responses shown here may be expected to be relevant to the initial adjustment phase of a symmetric NDBT vortex on a β-plane with steady environmental winds.

Second, in a linear dynamical system that is first order in time and exhibits a damped transient response to steady forcing, the magnitude of the steady-state condition can be expected to be proportional to the magnitude of the forcing, but inversely proportional to the magnitude of any parameter that acts to increase the rate of transient damping. Such an assertion is formally verifiable in the case of a constant coefficient ordinary differential equation, and may be reasonably extended to NDBT vortex dynamics for situations where numerical evidence (*i.e.*, FE; DM) confirms a damped transient response to steady asymmetric forcing. Thus, the impact of perturbation azimuthal and radial structure on the damping process in this model can be expected to influence the steady-state response to asymmetric forcing.

2. Barotropic vortex adjustment to steady forcing

The process by which vortex adjustment to steady asymmetric forcing occurs in the various NDBT simulations of TC motion (Anthes and Hoke 1975; Kitade 1981; DM; CW; FE) may be explained as follows. As the initially symmetric vortex advects planetary and environmental vorticity or is distorted by environmental wind shear and vortex motion, an asymmetric component of vortex vorticity is generated from the symmetric component as indicated in (3.12). This process is a transfer of kinetic energy from the symmetric vortex to the growing asymmetry. If the self-advection process is omitted as in CW, then the energy transfer continues unchecked and causes rapid dispersion of the vortex. However, the analysis in Section C.1 showed that advection of the asymmetric vortex vorticity by the radially sheared symmetric angular wind acts to transfer perturbation energy to the symmetric vortex (Fig. 3.6) in this model. In the NDBT models just cited, the rate of energy transfer to the symmetric vortex apparently grows as the forced asymmetry grows until a quasi-steady balance is achieved over the region in which the symmetric vorticity is significantly greater than the asymmetric vorticity. This balance is in large measure achieved by about 24 h for asymmetries associated with vortex advection of environmental absolute vorticity (Fig. 3.4b), and occurs much faster for asymmetries associated with distortion of the vortex by the environment, vortex motion, or asymmetric convection (Fig. 3.4a). This variability in adjustment time scale for different asymmetries is due primarily to the difference in radial dependence between v_s (r^{-1}) and the radial gradient of ζ_s (r^{-3}) from which the asymmetries are generated. Although these particular dependences are specific to a near-Rankine vortex, the principal applies generally since the symmetric vorticity gradient must decrease faster than the symmetric wind for all vortical flows that tend toward zero with increasing radius.

The steady-state phase and amplitude toward which the asymmetric structure tends clearly cannot be addressed with a homogeneous model that also excludes the potentially important influence of discrete normal modes. However, two aspects of the steady state may reasonably be inferred. First, the steady-state asymmetry will likely retain a down-shear tilt to maintain the vortex against the continuous dispersive effect of the asymmetric forcing. Such a feature was noted by FE in the structure of a vorticity-induced asymmetry. The second inference concerns the combination of radial and azimuthal dependence that is likely to be present in the steady-state asymmetry. In the absence of environmental winds, the β-effect results in a quasi-steady vortex asymmetry that is essentially wavenumber 1 in structure (FE). However, as shown in Chapter II, a horizontally variable environmental windfield will act to induce higher wavenumbers

51

through distortion of the symmetric vortex. The spatial structure of the resultant asymmetry will depend on both the spatial structure of the environmental forcing and the dependence of the damping mechanism on perturbation structure. The author is not aware of any detailed analyses of the wavenumber distribution and radial structure of TC asymmetries in either composite observations or model runs using realistic windfields. Thus, it is merely noted that the wavenumber and radial dependences of the stabilization mechanism shown here should contribute to the predominance of low wavenumbers and increasing axisymmetry toward the vortex center respectively.

E. SUMMARY AND DISCUSSION

The principal objective of this chapter has been to identify the asymmetry-damping influence of symmetric angular windshear as the mechanism by which a NDBT vortex counters dispersive and distorting influences over the region dominated by nonlinear self-advection. The present "linear" model captures the essence of the self-advection process by linearizing with respect to a nonzero symmetric basic state. In the NDBT models cited in Section D.2, the asymmetry-damping mechanism acts as a negative feedback process in which a kinetic energy transfer from the asymmetric to the symmetric component of the vortex occurs as a result of, but in opposition to, the kinetic energy transfer from symmetric to asymmetric component induced by external forcing.

In the previous section, the stabilization mechanism was applied to the initial adjustment of a symmetric NDBT model vortex subjected to steady asymmetric forcing. However, the principle can also explain NDBT vortex adjustment to changes in the external forcing with time. For example, assume that a quasi-steady vortex asymmetry exists due to previously steady asymmetric forcing, and that a change now occurs in the environmental windfield, e.g., in β_{eff} (3.16) or S_E (3.19). If the change is such that the magnitude of asymmetric forcing at a particular wavenumber is reduced (increased), then the shear-induced feedback of energy from the existing asymmetry to the symmetric vortex will be greater (less) than the environmentally-forced transfer of energy from the symmetric vortex to the asymmetry. As a result, the vortex will adjust toward a less (more) asymmetric state at that particular wavenumber until a quasi-steady balance is reestablished. A similar adjustment process would take place if the radial distribution of the forcing at any wavenumber is altered by changes in symmetric vortex structure. If the duration of the external forcing change is brief compared to the time scale of the stabilization mechanism (i.e., approximating a step-function), then the adjustment time should be on the order of the stabilization time scale. Conversely, if the forcing is slowly

varying in time compared to the stabilization time scale (*e.g.*, a TC propagating poleward through a steady, but latitudinally variable windfield as in DM), then the adjustment process should have a time scale appropriate to the "apparent variability" of the environment from a reference frame moving with the vortex. Such a scenario is not intended to be all inclusive, since dynamical situations may exit in which the vortex might be barotropically unstable to asymmetric forcing, or in which temporary continuous spectrum growth might occur analogous to the temporary baroclinic growth mechanism studied by Farrell (1982).

Symmetric angular windshear outside the radius of maximum winds can be expected to exert a dominant influence on the stability of any barotropic vortex. Shapiro and Ooyama (1989) have shown that divergence had negligible influence on TC propagation, and thus stability to asymmetric forcing within a barotropic context. In baroclinic model vortices or in a TC, the role of a barotropic stability mechanism in influencing vortex asymmetries will depend on the competing influence of the inertial stability/instability made possible by the introduction of a secondary circulation into the dynamics. Modeling studies of ocean eddies indicate that coupling between vertical modes can also be expected to alter vortex stability and associated motion (McWilliams and Flierl 1979). Significant radial shear in the tangential winds exists to large heights in a mature TC (*e.g.*, Hawkins and Imbembo 1976, their Fig. 13; Frank 1977, his Fig. 9). Thus, the essential element that enables the barotropic vortex stability mechanism to operate is certainly present in TC's. As mentioned earlier, the qualitative similarity of TC motion tracks in baroclinic models (Madala and Piacsek 1975; Kitade 1980) to barotropic results provides at least circumstantial evidence to suggest that baroclinic vortex stability is a modification to, rather than being fundamentally different from, barotropic vortex stability. Since, the magnitude of TC tangential windshear decreases with height above the boundary layer and with increasing radius outside the radius of maximum winds, a barotropic stability mechanism should be most influential in the region where the TC's convective forcing is initiated.

IV. BAROTROPIC VORTEX SELF-ADVECTION

In this chapter, an analytical NDBT model of TC propagation due to planetary and environmental influences will be developed from the Self-advection Region and Dispersion Region equations of Chapter II. The three principal obstacles that must be overcome are: i) the temporal dependence of the equations; ii) the strong radial variability of the symmetric flow variables; and iii) the additional unknowns represented by the speed and direction of TC propagation.

The problem of temporal variability will be eliminated by seeking only a steady-state solution for TC propagation. Thus, it will be assumed that the model TC is fully adjusted to the asymmetric forcing of the environment at any time. The complex radial variability of the symmetric flow will be simplified by approximating the tangential wind by "piecewise-defined" function. The presence of the propagation velocity in the Self-advection Region equation will be addressed in two ways: i) using externally generated values for $\hat{C}$ and α; and ii) devising an internal closure scheme that will enable the present model to predict $\hat{C}$ and α.

A. MODEL DEVELOPMENT

1. Solution for the Self-advection Region

The analysis of Chapter III has shown that the damping influence of symmetric angular windshear will permit (2.36) to evolve toward a steady-state from an unbalanced initial condition. Thus, the analysis here will focus on solving

$$\frac{v_S}{r}\frac{\partial \zeta_A}{\partial \theta} + u_A \frac{\partial \zeta_S}{\partial r} = v_S \beta_{eff}\sin(\theta - \phi) + \hat{C}\frac{\partial \zeta_S}{\partial r}\cos(\theta - \alpha). \qquad (4.1)$$

The propagation term appears as a forcing process in (4.1), and thus introduces the unknown parameters $\hat{C}$ and α as noted above. The streamfunction and complex Fourier series definitions of Chapter III will also be used here. Thus, substituting (3.5a,b) and (3.7) for $k=1$ into (4.1) gives

$$\frac{i\,v_S}{r}\left[\frac{\partial^2}{\partial r^2} + \frac{1}{r}\frac{\partial}{\partial r} - \frac{1}{r^2}\right]\Psi'(r) - \frac{i}{r}\frac{\partial \zeta_S}{\partial r}\Psi(r)$$

$$= -i\,v_S\,\beta_{eff}\,e^{-i\phi} + \hat{C}\frac{\partial \zeta_S}{\partial r}e^{-i\alpha}. \qquad (4.2)$$

54

in which the identities

$$\cos \theta = \text{Re}\{e^{i\theta}\} \qquad \sin \theta = \text{Re}\{-i\,e^{i\theta}\}, \qquad (4.3a,b)$$

have been used, and the superscript on Ψ has been omitted since all subsequent analysis will deal exclusively with wavenumber one asymmetries. Equation (4.2) is put in standard form by dividing through by $\frac{iv_S}{r}$, which gives

$$\left[\frac{\partial^2}{\partial r^2} + \frac{1}{r}\frac{\partial}{\partial r} - \frac{1}{r^2} \right]\Psi(r) - \frac{1}{v_S}\frac{\partial \zeta_S}{\partial r}\Psi(r)$$

$$= -r\beta_{eff}\,e^{-i\phi} - \frac{i\hat{C}r}{v_S}\frac{\partial \zeta_S}{\partial r}e^{-i\alpha}. \qquad (4.4)$$

To obtain closed-form analytical solutions to (4.4), a convenient but realistic functional form must be found for the symmetric flow. In particular, requiring

$$\frac{1}{v_S}\frac{\partial \zeta_S}{\partial r} \propto \frac{1}{r^2}, \qquad (4.5)$$

has the desirable property of making the left side of (4.4) equidimensional similar to (3.8a). It may be readily verified that

$$v_S(r) = A_n r^{X_n} + B_n r^{-X_n}, \qquad (4.6)$$

has an associated vorticity gradient

$$\frac{\partial \zeta_S}{\partial r}(r) = \frac{X_n^2 - 1}{r^2}v_S(r), \qquad (4.7)$$

and that the product of (4.6) and (4.7) satisfies (4.5). Thus, substituting (4.6) and (4.7) into (4.4) gives

$$\left[\frac{\partial^2}{\partial r^2} + \frac{1}{r}\frac{\partial}{\partial r} - \frac{X_n^2}{r^2} \right]\Psi(r) = \Gamma_1(r), \qquad (4.8a)$$

$$\Gamma_1(r) \equiv -r\beta_{eff}\,e^{-i\phi} - \frac{i\hat{C}(X_n^2 - 1)}{r}e^{-i\alpha}. \qquad (4.8b)$$

It is important to note that the radial gradient of the symmetric component of the vorticity for any finite vortex such as a TC must change sign at least once. Subsequent calculations of R_T will show that a vorticity gradient sign change occurs within the Self-advection Region for TC wind profiles typically used in barotropic models. In contrast, the vorticity gradient given by (4.7) is monodirectional for a single value of X_n in a region where v_s is purely cyclonic. Thus, at least two segments of v_s as defined by (4.6) for different parameters (*i.e.*, n = 1,2, . .) must be combined to approximate a TC symmetric windfield. The two linear (A_n and B_n) and one nonlinear (X_n) degrees of freedom in (4.6) permit such a "piecewise-defined" vortex to have continuous values of velocity and vorticity, but a only piecewise-continous vorticity gradient. As a result, (4.8a,b) must be solved in at least two annular regions for particular values of X_n, and then a total solution must be constructed by applying matching conditions at the interface(s) as shown in Subsections A.3 and A.4 below. The approach here is to circumvent the difficulty in obtaining closed-form analytic solutions (*i.e.*, all derivatives continuous) to (4.4), by seeking piecewise-analytic solutions based on a piecewise-analytic approximation for the symmetric TC.

Consider one of the annular regions with r = a and r = b representing the inner and outer boundary respectively. Within this region, a solution of (4.8a) may be obtained by noting that the functions r^{-X_n-1} are integrating factors for the left side. Multiplying (4.8a) by r^{X_n-1} and integrating from a to r gives

$$\int_a^r \frac{\partial}{\partial \rho}\left[\rho^{X_n+1}\frac{\partial \Psi_n}{\partial \rho} - X_n\rho^{X_n}\Psi_n\right]d\rho = \int_a^r \rho^{X_n+1}F_1(\rho)d\rho, \qquad (4.9)$$

and multiplying (4.8) by r^{-X_n-1} and integrating from r to b gives

$$\int_r^b \frac{\partial}{\partial \rho}\left[\rho^{-X_n+1}\frac{\partial \Psi_n}{\partial \rho} + X_n\rho^{-X_n}\Psi_n\right]d\rho = \int_r^b \rho^{-X_n+1}F_1(\rho)d\rho, \qquad (4.10)$$

in which a n-subscript has been added to Ψ to denote the nth annulus. Performing the indicated integrations and eliminating $\partial \Psi_n/\partial r$ from the equations gives

$$\Psi_n(r) = \frac{r^{2X_n}}{2X_n r^{X_n}}\left[+b^{-X_n+1}\frac{\partial \Psi_n}{\partial r}\bigg|_b + X_n b^{-X_n}\Psi_n\big|_b\right]$$

56

$$+ \frac{1}{2X_n r^{X_n}} \left[-a^{X_n+1} \frac{\partial \Psi_n}{\partial r} \Big|_a + X_n a^{X_n} \Psi_n \Big|_a \right]$$

$$+ \frac{1}{2X_n r^{X_n}} G_1(X_n, a, r, b) \qquad\qquad a \leq r \leq b, \qquad (4.11a)$$

in which G_1 results from the right sides of (4.9) and (4.10), and is defined by

$$G_1(X_n, a, r, b) = + \beta_{eff} e^{-i\phi} \left[\frac{r^{X_n+3} - a^{X_n+3}}{X_n + 3} + r^{2X_n} \frac{b^{-X_n+3} - r^{-X_n+3}}{-X_n + 3} \right]$$

$$+ \hat{C}(X_n^2 - 1) e^{-i\alpha} \left[\frac{r^{X_n+1} - a^{X_n+1}}{X_n + 1} + r^{2X_n} \frac{b^{-X_n+1} - r^{-X_n+1}}{-X_n + 1} \right]. \quad (4.11b)$$

Solutions for as many annulae as necessary to approximate the symmetric wind profile with segments defined by (4.6) may be constructed from (4.11).

2. Solution for the Dispersion Region

Since (2.37) is a first-order hyperbolic equation in variable ζ_A, the method of characteristics may be used to give an initial value solution of

$$\zeta_A(r, \theta, t) = \frac{2 v_S \beta_{eff}}{Z_E} \left[\cos(\theta - \frac{Z_F t}{2} - \phi) - \cos(\theta - \phi) \right], \qquad (4.12)$$

in which $\zeta_A(r, \theta, 0) = 0$ has been assumed. The response is an undamped oscillation with period $4\pi/Z_E$ about the steady-state solution to (2.37), which is

$$\zeta_A(r, \theta) = - \frac{2 v_S \beta_{eff}}{Z_E} \cos(\theta - \phi). \qquad (4.13)$$

It should be noted that no steady solution exists in the limit as $Z_E \to 0$, and that (4.12) then reduces to

$$\zeta_A(r, \theta, t) = t v_S \beta_{eff} \sin(\theta - \phi), \qquad (4.14)$$

with $\beta_{eff} = \beta$ and $\phi = 90°$.

In view of abundant numerical evidence for quasi-steady TC propagation, the physical relevance of (4.12) and (4.14) for large t is doubtful. Such continually evolving solutions are consistent with the Dispersion Region assumption that completely excludes the stabilizing influence of self-advective processes. Within the present modeling con-

57

text, asymmetry damping due to self-advection can impact the Dispersion Region only via dynamical matching conditions at the transition radius. Consequently, the evolution of (4.12) will limited by determining an "adjustment time" (T_{adj}) such that the Dispersion Region solution obtained below and the solution for the outermost annulus in the Self-advection Region satisfies an appropriate matching condition at the transition radius (Subsection 3).

Making the substitution $t = T_{adj}$, and applying the streamfunction (3.5a,b) and complex Fourier series definitions (3.7) to (4.12) gives

$$\left[\frac{\partial^2}{\partial r^2} + \frac{1}{r} \frac{\partial}{\partial r} - \frac{1}{r^2} \right] \Psi(r) = F_2(r) \qquad (4.15a)$$

$$F_2(r) \equiv \frac{2 \, v_S(r) \, \beta_{eff}}{Z_E} e^{-i\phi} \left[e^{-i \frac{Z_E T_{adj}}{2}} - 1 \right]. \qquad (4.15b)$$

Given an appropriate form for v_S in the Dispersion Region, (4.15) may be solved using the integrating factors r^2 and r^n. A convenient choice is

$$v_S(r) = A_n r^{-4} + B_n r^{-5}, \qquad (4.16)$$

since A_n and B_n provide the necessary degrees of freedom to match both the value of the function and the first derivative of (4.6) and (4.16) at $r = R_T$. Also, the choice of exponents in (4.16) ensures closed-form solutions to (4.15) that remain bounded as $r \to \infty$. By the same procedure used for (4.11), the solution to (4.15) is

$$\Psi_n(r) = \frac{r^2}{2r} \left[\left. \frac{\partial \Psi_n}{\partial r} \right|_b + \frac{1}{b} \left. \Psi_n \right|_b \right] + \frac{1}{2r} \left[-a^2 \left. \frac{\partial \Psi_n}{\partial r} \right|_a + a \left. \Psi_n \right|_a \right]$$

$$+ \frac{1}{2r} G_2(a,r,b) \qquad a \leq r \leq b, \qquad (4.17a)$$

$$G_2(a,r,b) \equiv \frac{2\beta_{eff}}{Z_E} e^{-i\phi} \left[e^{-i \frac{Z_F T_{adj}}{2}} - 1 \right] \left[\frac{A_n(a-r)}{ar} + \frac{B_n(a^2 - r^2)}{2a^2 r^2} \right.$$

$$\left. + \frac{A_n(r^3 - b^3)}{3rb^3} + \frac{B_n(r^4 - b^4)}{4r^2 b^4} \right]. \qquad (4.17b)$$

58

Only one annulus will be used to represent the Dispersion Region. Thus, $r = a$ is the transition radius and $r = b$ is the outer boundary of the model in (4.17a,b). In the case of a quiescent environment, evaluating the limit of (4.17b) as $\dot{Z}_E \to 0$ gives

$$G_2(a,r,b) \equiv -\beta T_{adj} \left[\frac{A_n(a-r)}{ar} + \frac{B_n(a^2 - r^2)}{2a^2 r^2} + \frac{A_n(r^3 - b^3)}{3rb^3} + \frac{B_n(r^4 - b^4)}{4r^2 b^4} \right].$$

3. Matching annular solutions

The solutions presented in Section B below will use at most three annular regions to define the model domain. Fig. 4.1 gives a schematic view of the model domain and annular subregions, and also shows the notation to be used to denote radial boundaries. Limiting values for R_0 and R_3 are the origin and infinity respectively. With $R_2 = R_T$, two of the annulae are within the Self-advection Region, and the transition radius is a matching interface. The alternate use of the symbol R_2 for the transition radius will permit a concise statement of the matching conditions in the following subsection.

a. Transition radius specification

A scale analysis of (2.36) will be used to provide an empirical formula for R_T. Implicit in the transition radius concept is the existence of an annular region about R_T where interaction and symmetric flow variables are roughly equal. For $r \approx R_T$, let

$$v_S, \hat{C}, u_A \approx v_S(R_T) \qquad \zeta_S, \zeta_A \approx \frac{v_S(R_T)}{R_T}.$$

Substituting these relationships into (2.36) and assuming a quasi-steady balance gives

$$\frac{v_S}{r} \frac{\partial \zeta_A}{\partial \theta} + [u_A - \hat{C} \cos(\theta - \alpha)] \frac{\partial \zeta_S}{\partial r} = v_S \beta_{eff} \sin(\theta - \phi)$$

$$\frac{v_S^2(R_T)}{R_T^2} \qquad\qquad \frac{v_S^2(R_T)}{R_T^2} \qquad\qquad v_S(R_T) \beta_{eff}$$

where the scales are shown below the respective terms. Assuming that the two self-advection terms do not cancel, it is necessary that

$$\frac{v_S(R_T)}{R_T^2} \approx \beta_{eff}. \tag{4.18}$$
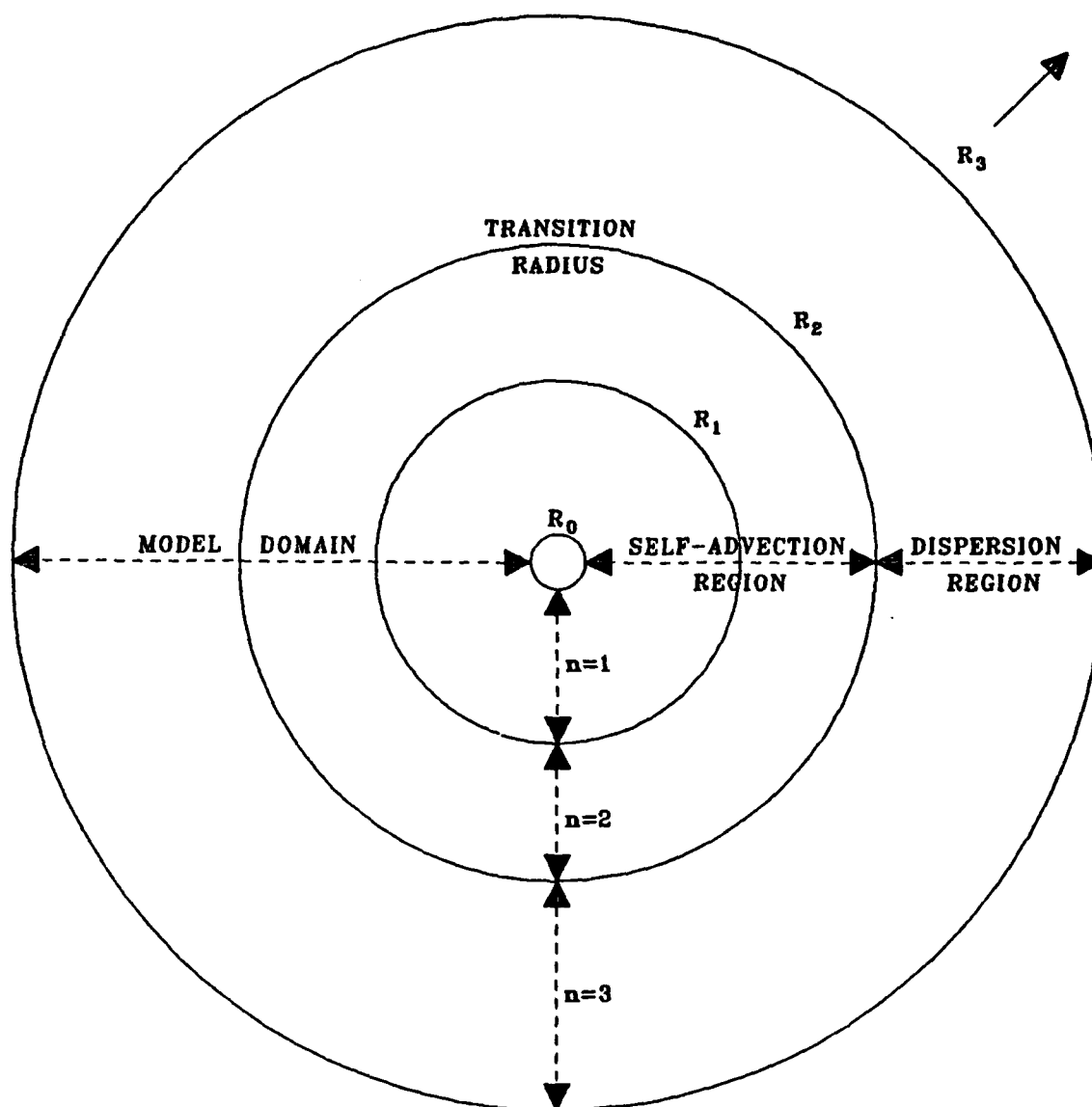
Fig. 4.1 An illustration of the model domain and three annular subdomains. The inner and outer boundaries of the model domain are denoted by R_0 and R_3 respectively. The interface between the inner ($n=1$) and outer ($n=2$) annulus of the Self-advection Region is denoted by R_1. The interface between the Dispersion Region annulus ($n=3$) and the inner annulae is denoted by R_2 and corresponds to the transition radius.

from which the empirical formula

$$R_T = \delta\left[\frac{v_S(R_T)}{\beta_{eff}}\right]^{\frac{1}{2}} \tag{4.19}$$

is obtained. Given an observed or specified radial profile of TC tangential winds and the magnitude of the environmental absolute vorticity gradient in the vicinity of the TC, a transition radius may be calculated from (4.19).

The parameter δ has been included in (4.19) to reflect the approximation in (4.18), as well as the uncertainty that will accompany any estimate of β_{eff}. Thus, δ is a "tunable" factor that could be adjusted in an "propagation + advection" forecasting model to minimize forecast error in some statistical sense. The extent to which a statistically determined δ approximates unity would tend to provide operational confirmation of the dynamical validity of the transition radius and Self-advection/Dispersion Region concepts. It will be shown below that assuming $\delta = 1$ provides realistic results, and will be altered only to test model sensitivity in Section C.3 below.

b. Boundary/Interface Condition Specifications

Eight boundary and interface conditions must be specified to construct a solution for the entire model domain from solutions to (4.11a) or (4.17a) in three annular subregions. The asymmetric streamfunction will be set to be zero at the boundaries of the model domain, R_0 and R_3, and the asymmetric streamfunction and velocity will be made continuous at the interface radii R_1 and R_2. The inner boundary condition is dynamically required if R_0 is the origin. The rationale for displacing R_0 from the origin is related to functional properties of (4.6), as will be explained later.

These conditions may be concisely expressed in terms of the complex variable Ψ as

$$\left.\Psi_1\right|_{R_0} = 0 \qquad \left.\Psi_3\right|_{R_3} = 0 \tag{4.20a,b}$$

$$\left.\Psi_n\right|_{R_n} = \left.\Psi_{n+1}\right|_{R_n} \qquad \left.\frac{\partial\Psi_n}{\partial r}\right|_{R_n} = \left.\frac{\partial\Psi_{n+1}}{\partial r}\right|_{R_n} \qquad n = 1,2. \tag{4.20c,d}$$

Practical implementation of conditions (4.20a-d) involves evaluating (4.11a,b) and (4.17a,b) at radii R_1, R_2, and R_3 to form a 6x6 linear system of equations in the variables

$$\left.\frac{\partial\Psi_1}{\partial r}\right|_{R_0}, \quad \left.\Psi_{1,2}\right|_{R_1}, \quad \left.\frac{\partial\Psi_{1,2}}{\partial r}\right|_{R_1}, \quad \left.\Psi_{2,3}\right|_{R_2}, \quad \left.\frac{\partial\Psi_{2,3}}{\partial r}\right|_{R_2}, \quad \left.\frac{\partial\Psi_3}{\partial r}\right|_{R_3},$$

in which double subscripts denote a matched quantity. The linear equation system will be solved using a standard computer algorithm.

Because (4.8a) and (4.15a) are second order in Ψ, the associated boundary/interface conditions provide only enough degrees of freedom to achieve continuous asymmetric streamfunction and velocity at R_1 and R_2. Thus, ζ_A is free to be piecewise-continuous at the interface radii, which is generally the case to dynamically balance (4.1) given the piecewise-continuous nature of the vorticity gradient associated with (4.6) and (4.16). As discussed above, the parameter T_{adj} provides an additional degree of freedom to permit matching of asymmetric vorticity at R_T. In general, it will be possible to match only the magnitude of ζ_A at R_T, since varying T_{adj} only influences G_2, and because the interface condition term in (4.17a) is irrotational. Nevertheless, the additional degree of smoothness given to model solution at R_T should be beneficial. To be consistent with this quasi-matching of ζ_A at R_T, parameters in (4.6) and (4.16) should be chosen to eliminate any discontinuity in $\partial \zeta_S / \partial r$ there. Not only is it possible to do this, but it is also desirable to facilitate closure of the model.

4. Outline of Solution Procedure

A NDBT solution for the propagation-inducing wavenumber one gyre streamfunction associated with known symmetric TC and environmental windfields has been obtained for an arbitrarily large domain $R_0 \leq r \leq R_3$ by matching three partial solutions that are separately valid in annular subdomains. In terms of the real streamfunction variable ψ_A, the solution is

$$\psi_A(r, \theta) = \text{Re}\{\Psi_n(r)e^{i\theta}\} \qquad R_{n-1} < r \leq R_n \qquad n = 1,2,3 \qquad (4.21)$$

where Ψ_1 and Ψ_2 are defined by (4.11a,b) and Ψ_3 is defined by (4.17a,b). The procedure to compute the model results shown in the remainder of this dissertation is:

1. Given an analytic function that approximates a TC symmetric wind profile, determine R_1 and R_T ($= R_2$) based on where the symmetric vorticity gradient changes sign and where the TC winds satisfy (4.19) respectively. Also, determine values for R_M and V_M.

2. Determine parameters A_n, B_n and X_n by constructing from (4.6) and (4.16) a piecewise-analytic approximation to the wind profile used in Step 1. Because of the irrational function form of (4.6), this task is accomplished by successive trials using interactive computer graphics. The procedure is outlined in Appendix B.

3. Assign values to the environmental parameters β_{eff}, ϕ and Z_F.

62

4. Determine propagation parameters $\hat{C}$ and α using either external information, or a closure scheme internal to the dynamics of this model.

5. Solve the 8x8 linear system of equations for the value and first derivative of the complex streamfunction as determined by the boundary/interface conditions (4.20a-d).

6. Iteratively compute the complete model solution (4.21) by varying T_{adj} until the magnitude of asymmetric vorticity is continuous at $r = R_T$.

B. MODEL RESULTS PART I: EXTERNAL CLOSURE

As indicated in Chapter I, many observations of TC propagation are clearly suggestive of the barotropic theories, although little or no information is available concerning the TC characteristics or the environmental windfields associated with those vectors. Additional problems are the unknown influence of baroclinic processes on TC propagation and possible random/systematic errors associated with the compositing process. Thus, only numerical predictions of TC propagation are suitable for externally closing this model to the degree of accuracy that accurate interpretation and analysis of the results can be made. The NDBT results of Fiorino and Elsberry (FE) (1989) will be used since that study provides both an accurate calculation of TC propagation with which to close this model, and detailed illustrations of the interaction flow from which the accuracy of closure can be evaluated. Since FE used only a quiescent environment, the parameter assignments $\beta_{eff} = \beta$, $\phi = 90°$ and $Z_E = 0$ will apply throughout this section. The response of the model to environmental forcing will be addressed within the context of the internal closure scheme developed in Section C below.

1. Symmetric TC Specification

The analytic function used by FE to approximate the symmetric windfield of a TC is

$$v_S(r) = r\, e^{(1-r^b)/b}, \tag{4.22}$$

in which the parameter b varies the strength of the TC, but not the maximum intensity. The windspeed and vorticity gradient given by (4.22) for FE's "basic vortex" (b = 0.96) are shown in Fig. 4.2a and 4.2b respectively. According to (4.18), the function $\beta_{eff}\, r^2$ (Fig. 4.2a) intersects $v_S(r)$ at the transition radius $R_T = 4.75$. The sign change of vorticity slope in Fig. 4.2b provides a good first estimate for R_1. The location of the inner boundary R_0 depends on properties of the piecewise-analytic wind profile as described below.

63
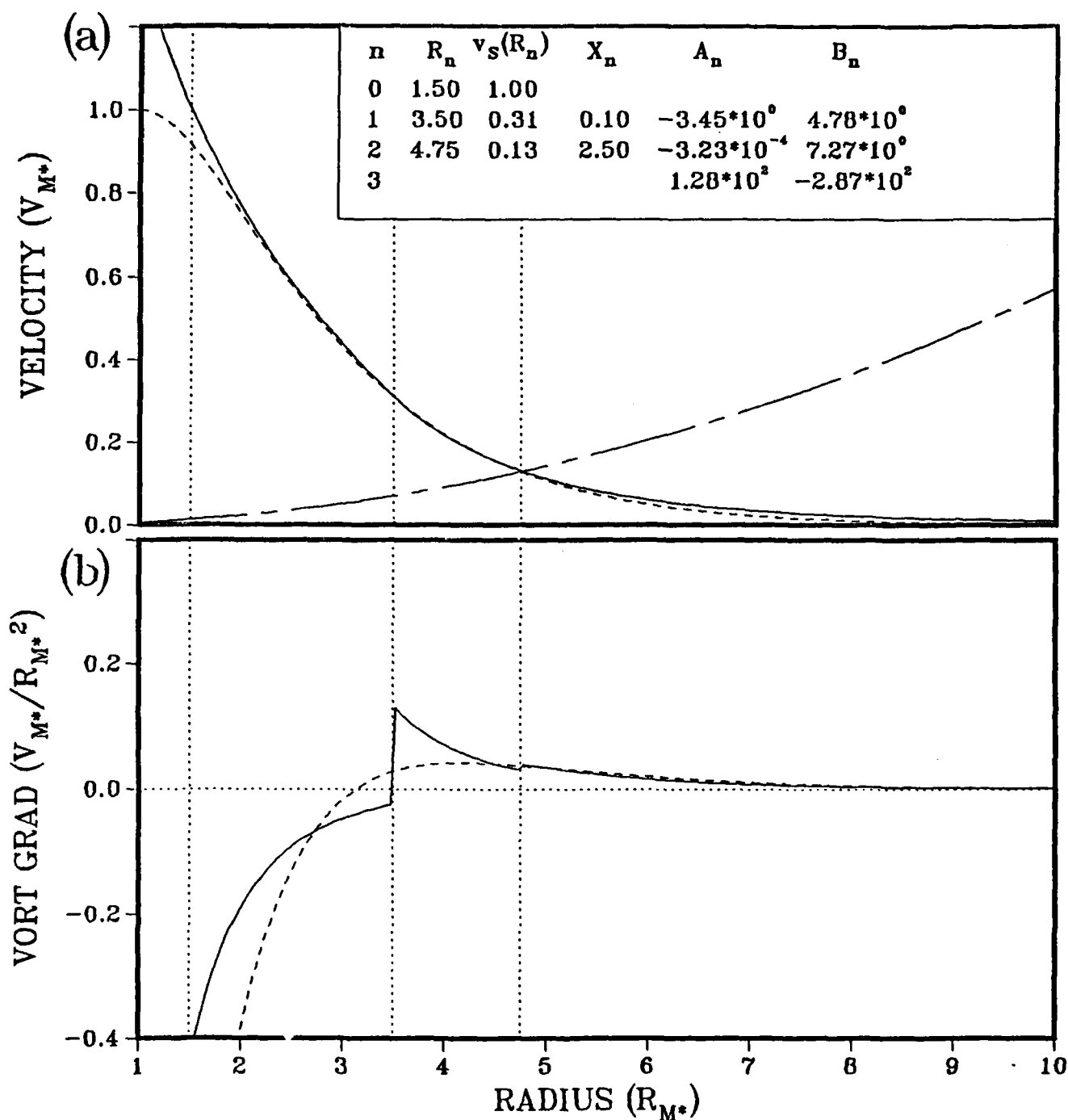
Fig. 4.2 (a) Radial profiles of the analytic TC windfield for the Fiorino and Elsberry (1989) basic vortex (dashed) and the piecewise-analytic function used (solid) to approximate it. Parameters that define the piecewise-analytic function according to (4.6) and (4.16) are shown in the inset. Vertical dotted lines (left to right) correspond to the radial boundaries/interfaces R_0, R_1 and R_2 ($= R_r$). The chain-dashed curve represents the function $\beta_{eff} r^2$. (b) The analytic and piecewise-analytic vorticity gradient profiles associated with the wind profiles in (a).

64

A piecewise-analytic wind profile is defined by (4.6) and (4.16) for the parameters shown in the inset in Fig. 4.2a. Because the functional properties of (4.6) do not permit the piecewise-analytic wind to have negative curvature, the two wind curves depart markedly near the radius of maximum winds. As a result, the values for R_0 and $v_S(R_0)$ have been chosen to improve the fit of the two curves at larger radii at the expense of poor fit at small radii, which is justified based on the insensitivity of TC propagation on TC intensity demonstrated by FE. It should be noted that the negative curvature region given by (4.22) near $r = 1$ is not generally representative of TC winds, which are much better fit by modified Rankine profiles just outside the TC eye (Anthes 1982; p. 24). Adjusting the piecewise-analytic profile to accomodate such an uncharacteristic wind curvature is at present justified by the need to compare this theoretical model with the results of FE that were based on (4.22).

The fit of the corresponding analytic and piecewise-analytic vorticity gradient profiles is illlustrated in Fig. 4.2b. As discussed earlier, the piecewise-analytic curve has a discontinuity at R_1 due to the change in X_n in (4.7) at that location. In contrast, the piecewise-analytic vorticity gradient is nearly continuous at the transition radius $(R_T = R_2)$ in anticipation of matching the magnitude of the wavenumber one gyre vorticity there. The choice of $R_1 = 3.5$, instead of where the analytic vorticity gradient changes sign ($r = 3$), was made to facilitate the matching of gyre vorticity at R_T. As in Fig. 4.2a, the piecewise-analytic curve in Fig. 4.2b accurately approximates the analytic profile at larger radii at the expense of a good fit at smaller radii. Because the vorticity gradient depends on the second derivative of the corresponding windfield, two very similar wind profiles can have quite dissimilar vorticity gradients. This fact has important implications for the dependence of TC propagation on outer wind strength, and will be addressed in Section C.3.b of this chapter and in Chapter V.

2. β-induced gyre structure

Using an initial symmetric TC wind defined by (4.22) with $b = 0.96$, and choosing $V_M = 35$ m/s, $R_M = 100$ km and $\beta = 2 \times 10^{-11} m^{-1}s^{-1}$, FE noted a β-induced propagation velocity of 2.65 m/s at 330° measured clockwise from North. Using their parameter specifications and the piecewise-analytic symmetric TC parameters in Fig. 4.2a, the present theoretical model for gyre structure may be "closed" by requiring $\hat{C} = 2.65$ m s and $\alpha = 120°$ (measured counterclockwise from East). The resulting asymmetric streamfunction for an outer model boundary at 10,000 km ($R_3 = 100$) is shown in Fig. 4.3 for the central 2400x2400 km of the domain. For comparison, the gyre structure extracted from FE's numerical model after 48 h is shown in Fig. 4.4.
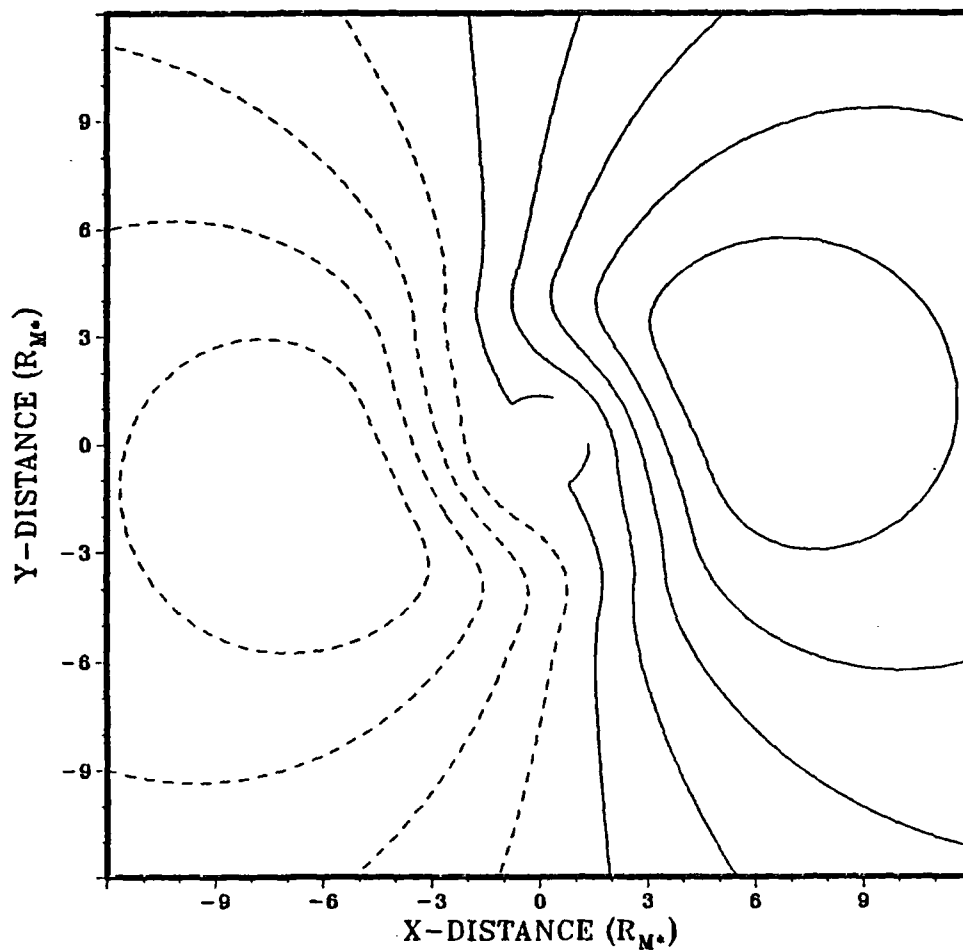
Fig. 4.3 Model-predicted wavenumber one gyre streamfunction (solid, positive; dashed, negative) using the piecewise-defined wind profile of Fig. 4.2a, and the parameter specifications: $V_{M*} = 40$ m/s, $R_{M*} = 100$ km, $\beta_* = 2 \times 10^{-11}$ $m^{-1}s^{-1}$, $\phi = 90$, $R_0 = 1.5$, $R_3 = 100$, $\hat{C}_* = 2.65$ m/s and $\alpha = 120$. The contour interval is $2 \times 10^5 m^2/s$, and only the inner 2400×2400 of the domain is shown to correspond to the illustration from FE in Fig. 4.4.
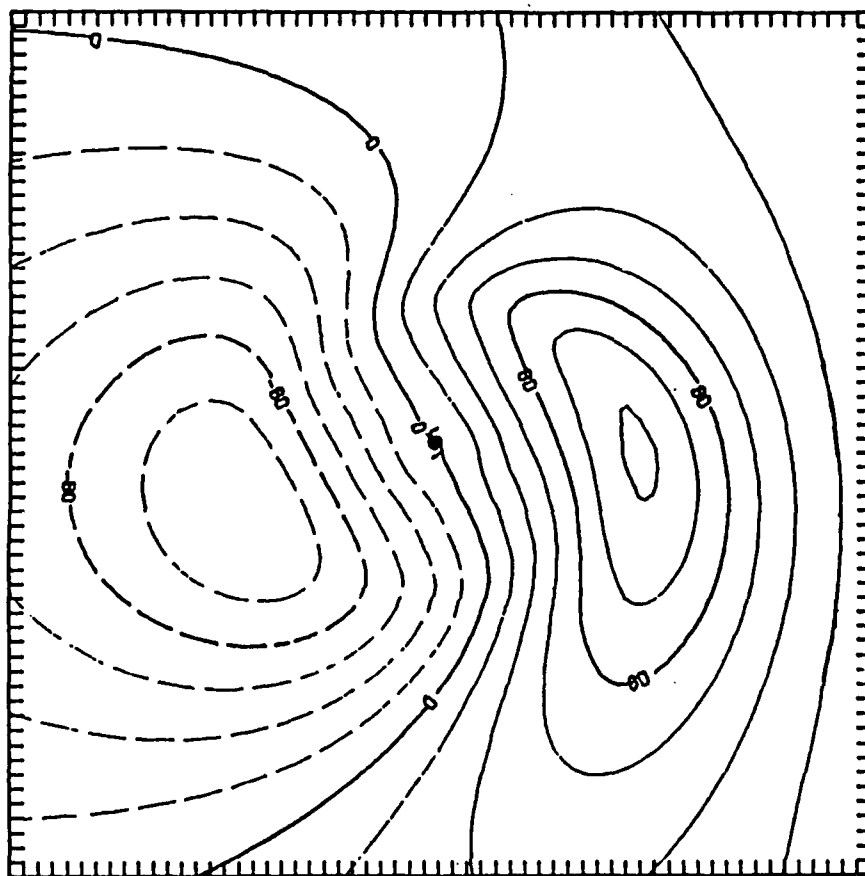
Fig. 4.4 Numerically predicted asymmetric streamfunction at 48 h due to β-induced distortion of a TC wind profile initially defined as in Fig. 4.2a. Contour interval is $2 \times 10^5 m^2/s$, and the distance between axis tick marks is 40 km (Fiorino and Elsberry 1989).

The analytically and numerically generated gyres have central uniform flow regions that agree quite closely with regard to flow strength and orientation, although some distortion due to $R_0 \neq 0$ is evident in Fig. 4.3. Such agreement is of fundamental importance for the analytical gyres to be consistent with the propagation velocity input from the FE numerical model. The radial positions of the streamfunction extrema are also accurate. However, the magnitudes of the extrema are about 20% less in Fig. 4.3. This is still a rather remarkable degree of agreement considering that the two potentially adjustable parameters R_T and T_{adj} have not been adjusted to improve the fit. Thus, the accuracy of the analytical gyre of Fig. 4.3 provides preliminary evidence that the concepts on which this model is based are dynamically sound. Further evidence will be provided in Chapter V by showing that wavenumber one gyres generated from this analytical model can accurately initialize a numerical model so that steady TC propagation begins almost immediately.

One of the differences between Figs. 4.3 and 4.4 is that the analytical gyres are symmetric relative to a line drawn between the extrema and antisymmetric relative to the zero contour line, whereas the numerical solution deviates somewhat from these conditions. The first-order wavenumber one approximations in the theoretical model and the cyclic east-west boundary conditions used in the numerical model are likely responsible for this dissimilarity. By retaining only the wavenumber one processes, the theoretical analysis has excluded the interaction process

$$\frac{\partial \psi_A}{\partial t} \propto -V_A \cdot \nabla f, \tag{4.23}$$

which results in a westward propagation of the interaction flow on the gradient of planetary vorticity. Such a propagation could explain the stretching weakening of the cyclonic gyre and compressing strengthening of the anticyclonic gyre in Fig. 4.4. This process is in effect generating a wavenumber two component from the wavenumber one gyres. The cyclic boundary condition in the numerical model artificially enhances this process by enabling the opposing gyres to interact in the eastern portion of the anticyclonic gyre, which is displaced southward relative to the analytical counterpart in Fig. 4.3. However, FE noted essentially negligible impact of these wavenumber two processes on TC propagation out to 144 hrs, which is further confirmation that a barotropic theory of TC propagation needs to retain only wavenumber one processes.

3. Influence of boundary conditions

As noted above, the choice of a nonzero inner boundary for the model has perturbed the uniform-flow region of the analytical gyre (Fig. 4.3). It is desirable to eliminate such an unphysical disturbance by moving R_0 to the origin. For a wind profile defined by (4.6), it is not possible to require the associated vorticity to be continuous for all $r>0$ and also be nonsingular at $r=0$. As in a geostrophic point vortex, the velocity in (4.6) and the higher derivatives are singular at the origin. Moving R_0 to the origin can be justified by noting that it is the ratio of the symmetric vorticity gradient to the symmetric velocity that influences the interaction flow within the Self-Advection Region (4.4). Since the ratio of (4.6) and (4.7) contributes to a regular singular point at the origin, the interaction flow streamfunction remains defined as $r \to 0$, even though v_s as defined by (4.6) is singular at the origin. The predicted gyre structure for $R_0 \approx 0$ (Fig. 4.5) eliminates the disturbed portion of the uniform flow region, but leaves the rest of the gyre structure essentially unchanged from that in Fig. 4.3. Since the TC associated with Fig. 4.5 has essentially infinite intensity, this result is in effect the ultimate extension of FE's numerical demonstration that barotropic TC propagation is virtually independent of TC intensity. The inner boundary of this model will be placed at the origin for all subsequent solutions.

The outer boundary of the theoretical model ($R_3 = 100$) is much larger than that typically used by numerical models. The impact of choosing $R_3 = 28$, which is about the distance from the center to the corners of the 4000x4000 km domain used by FE, is shown in Fig. 4.6. Although the peak values of the gyre streamfunction have been reduced about 8% compared to Fig. 4.5, the uniform flow region of Fig. 4.6 is virtually unchanged, which confirms the domain size tests of Fiorino (1987). Increasing the outer boundary of the theoretical model had no significant effect on the gyre structure, which indicates the $R_0 = 100$ is effectively infinity as far as the theoretical model response is concerned.

C. INTERNAL CLOSURE FORMULATION

In the absence of external information on TC propagation under given environmental conditions, determining the correct wavenumber gyre structure depends on a closure scheme to predict the associated propagation. Such a scheme will be termed "internal closure" since it is based solely on inherent dynamical characteristics of the theory. The analysis that follows is founded on the basic hypothesis that the "correct" propagation velocity will be associated with a particular gyre structure that is unique and

69
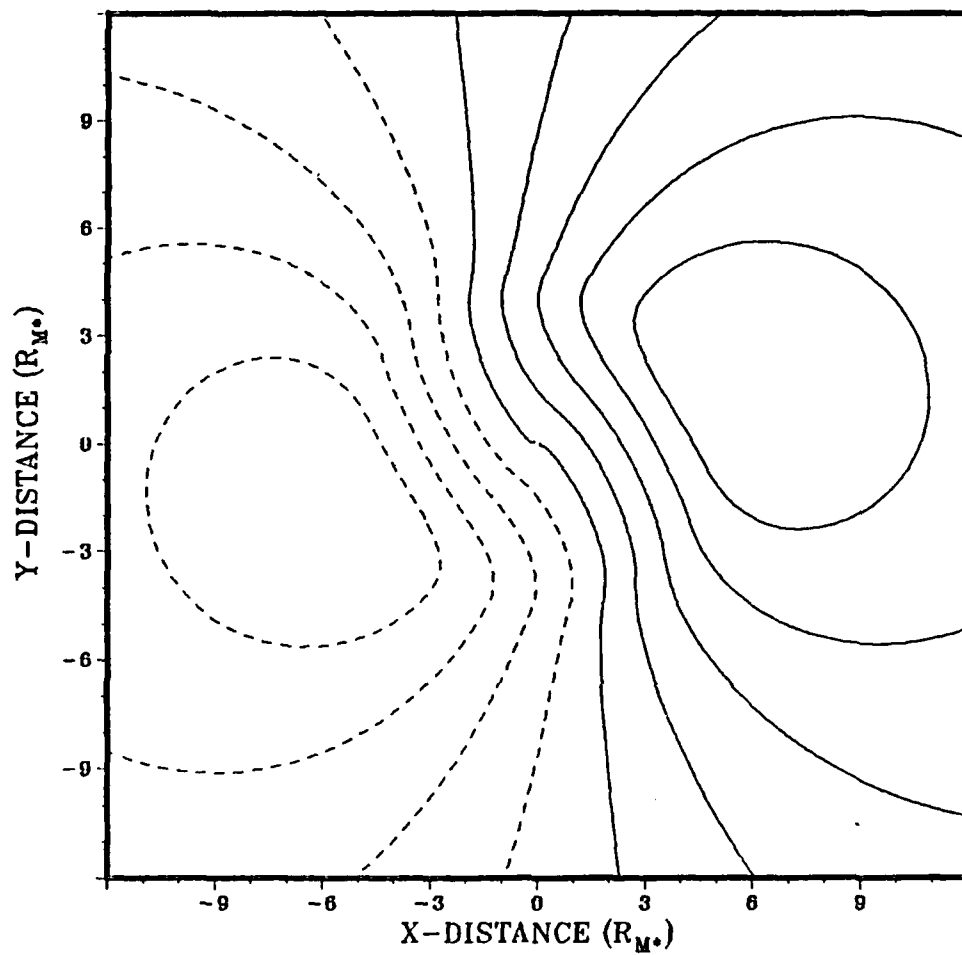
Fig. 4.5 As in Fig. 4.3, except for $R_0 \approx 0$.
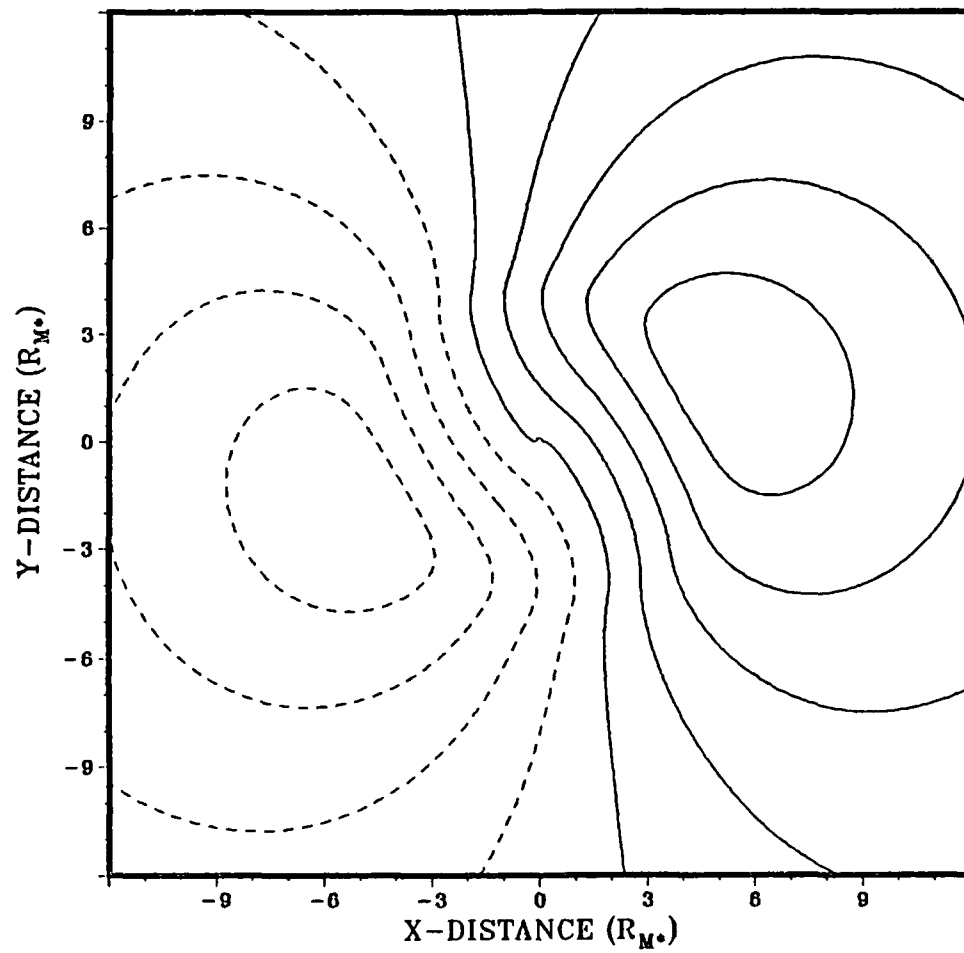
Fig. 4.6 As in Fig. 4.5, except for $R_3 = 28$.

readily discernable. Since the work of FE will be used to provide both motivation for and validation of this approach, the closure scheme will be developed within the context of TC propagation in a quiescent environment, and then applied in Section D below to illustrate the response of the model to variable environmental winds.

1. Preliminary Analysis

As noted in Chapter I, FE found that the advection of the wavenumber one gyre by the symmetric winds of the TC produces a streamfunction tendency that nearly cancels the tendency associated with the advection of planetary vorticity by the symmetric winds. Shapiro and Ooyama (1989) have recently refined this concept further by showing that tangential windshear produces nearly uniform asymmetric absolute vorticity within ≈ 350 km of the TC center. As shown in Chapter II, this process is fundamentally a kinetic energy feedback loop in which a transfer of energy from the asymmetry to the symmetric TC due to symmetric angular windshear occurs as a result of, and in opposition to, the transfer of energy from symmetric TC to the asymmetry induced by a gradient of planetary vorticity (β).

The closure scheme developed here will implement the above concepts by seeking a particular balance among the various processes that contribute to interaction flow vorticity tendency. Using (4.1), the balance in the Self-Advection region must be

$$- \frac{v_S}{r} \frac{\partial \zeta_A}{\partial \theta} - v_S \beta \cos \theta - u_A \frac{\partial \zeta_S}{\partial r} + \hat{C} \frac{\partial \zeta_S}{\partial r} \cos(\theta - \alpha) = \frac{\partial \zeta_A}{\partial t} \equiv 0, \quad (4.24)$$

in which a quiescent environment has been assumed, and the identity on the right emphasizes the steady-state nature of the present model. In light of Shapiro and Ooyama's observation, (4.24) will be scaled by $-\partial \zeta_S/\partial r$ to give

$$\left[\frac{1}{r} \frac{\partial \zeta_A}{\partial \theta} + \beta \cos \theta \right] \frac{v_S}{\partial \zeta_S/\partial r} + u_A - \hat{C} \cos(\theta - \alpha) = 0, \quad (4.25)$$

$$\text{(a)} \qquad\qquad \text{(b)} \qquad\qquad \text{(c)} \qquad \text{(d)}$$

which is valid at all radii except where the symmetric vorticity gradient goes to zero. Terms (a)-(c) of (4.25) represent contributions to the vorticity tendency of the interaction flow associated with symmetric angular windshear, β-induced dispersion, and advection of symmetric TC vorticity by the uniform portion of this interaction flow respectively (hereafter the "Shear", "Beta" and "Advection" terms). Term (d) represents a vorticity tendency that is an artifact of the movement of the model reference frame with

72

the propagating TC (hereafter the "Motion" term). The quantity within the brackets in (4.25) is in fact the asymmetric absolute vorticity gradient, which according to Shapiro and Ooyama must become nearly zero inside about 350 km for a TC undergoing quasi-steady propagation. Thus, the cancellation of the Shear and Motion terms results in the Motion term being balanced solely by the Advection term, as observed by FE.

Since all the terms on the left side of (4.25) are wavenumber one processes, a particular direction may be associated with the maximum vorticity tendency of each term at any radius. The vectors in Fig. 4.7a,b show the magnitude and direction of such vorticity tendency maxima at $r = 2$ and 4 respectively associated with the wavenumber one gyre streamfunction (Fig. 4.5) predicted by this model using a piecewise-analytic approximation to FE "basic" vortex (Fig. 4.2a) and their reported propagation velocity of 2.65 m/s at 330° ($\alpha = 120$). Since (4.25) has been scaled by the symmetric vorticity gradient, the Shear, Beta and Advection terms appear in Fig. 4.7a,b as velocity components that must together balance the imposed Motion vector. Since the symmetric vorticity gradient changes sign in the Self-advection Region, two radii have been chosen to permit comparison of the balance between the inner ($r = 2$) and outer ($r = 4$) annulus of the Self-advection Region.

A radial profile (Fig. 4.7c) of the amplitude and phase of the interaction flow vorticity (ζ_A) corresponding to the streamfunction in Fig. 4.5 highlights distinct amplitude and phase changes between the inner and outer annulus of the Self-advection Region. Identifying specific patterns in both this profile of interaction flow vorticity and the orientation of vorticity tendency vectors above is the basis for the following closure scheme.

2. The Closure Scheme

Because the Shear and Beta vector tend to oppose each other in Fig. 4.7a and b, the Advection vector balances most of the imposed Motion vector. Such a vector pattern may be regarded as roughly consistent with FE's observation that the streamfunction tendencies associated with the Shear and Beta terms of (4.25) nearly cancel in their numerical solutions. If barotropic TC propagation is indeed precisely steady propagation, then the Beta and Shear vector would be expected to cancel exactly. The inexact cancellation in Fig. 4.7 may be attributed to inaccuracies in the theoretical model and or the possibility that barotropic TC propagation is more a quasi-steady process than a truly steady process. Assuming that the second factor is primarily responsible for the vector pattern in Fig. 4.7, a closure scheme based on precisely steady propagation will be feasible if: i) a propagation velocity can always be found such that

SHEAR TERM MOTION TERM
BETA TERM ADVECTION TERM
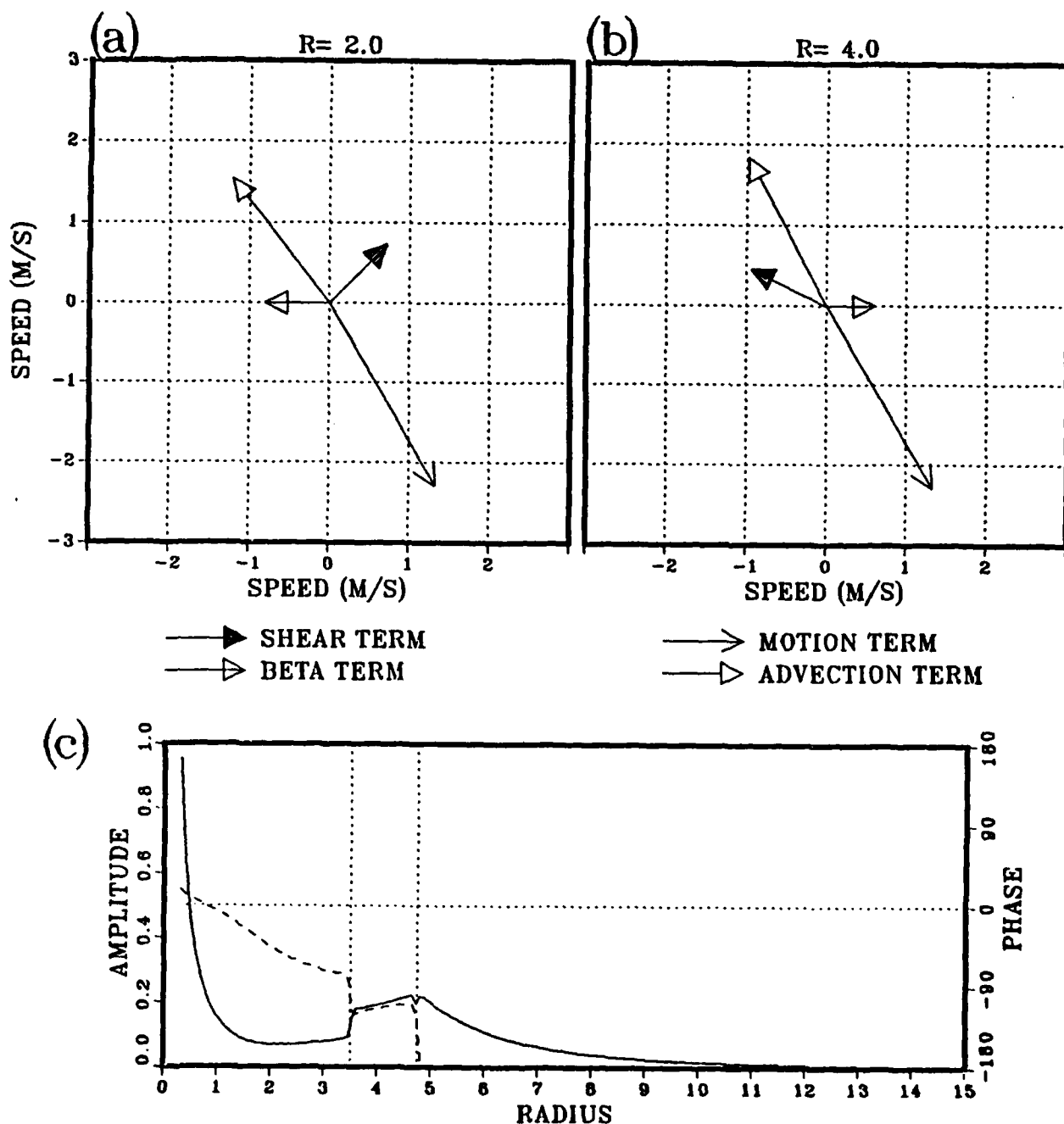
FIG. 4.7 (a)-(b) Vector diagrams showing direction and magnitude of ζ_A tendency maxima that have been scaled by $-\partial\zeta_s/\partial r$ at (a) $r=2$ and (b) $r=4$ respectively. The vectors represent the terms of (4.24) (see key above), and were computed using the piecewise-defined symmetric TC wind profile of Fig. 4.2a and the wavenumber one gyre solution of Fig. 4.5. (c) Radial profiles of the amplitude (solid) and phase (dashed) of ζ_A corresponding to the streamfunction field of Fig. 4.5. The amplitude curve has been scaled by the amplitude of ζ_A at $r=0.2$. Vertical dotted lines (left to right) correspond to R_1 and R_2.

74

theoretical model predicts precise cancellation of the Shear and Beta vectors; and ii) such a propagation velocity is a reasonable approximation to the quasi-steady result obtained from a dynamically equivalent numerical model. As shown in Fig. 4.8a, the propagation velocity $\hat{C} = 1.9$, $\alpha = 130$ satisfies the first of the above conditions. Such a closure scheme is clearly radius dependent since the Shear and Beta terms in Fig. 4.8b are opposite in phase, but are somewhat unequal in magnitude. Although the theoretically predicted propagation direction differs by only 10° from the propagation direction reported by FE, the speed difference of 0.75 m/s represents a significant error.

Both the speed error and the radius dependent nature of the above closure scheme may be addressed by recalling FE's demonstration that TC propagation and advection by V_A in the uniform flow region are nearly, but not precisely equal. They observed vector differences between the propagation velocity of the TC and the uniform portion of the interaction flow (their "ventilation flow") that are persistently westward at about 0.3 m/s (Fig. 4.9). This difference is readily evident quite early (12 h) in the integration, which suggests a linear Rossby wave-type propagation associated with the subsynoptic scale Fourier components of the symmetric TC. Such a hypothesis is supported by Shapiro and Ooyama's (1989) Fourier-Bessel spectral analysis, which showed that the squared angular momentum spectrum for a typical TC wind radial profile has a distinct peak at a radial length scale of 200 km. If this radial length scale is regarded as approximately equivalent to the inverse of a sinusoidal wavenumber, then it may be shown that a symmetric nondivergent Rossby wave of such a length scale will propagate westward at 0.4 m/s.

The requirement that the Shear vector exactly cancels the Beta vector in the closure scheme is inconsistent with these numerical results that only the component of the Beta vector over about 0.4 m/s actually contributes to distortion of the TC circulation. That is, only the relative linear propagation speeds of the large and small scale Fourier components contributes to the distortion of the TC circulation. Thus, a better closure formulation is to choose $\hat{C}$ and α so that at a radial location 200 km from the TC center the Beta and Shear vectors are 180° out of phase and differ in magnitude by 0.4 m/s (Fig. 4.10a). The resulting values for $\hat{C}$ and α for this closure scheme are 2.4 m/s and 132° respectively, which reduces the speed error to 0.25 m/s. Such an error is considered quite acceptable in view of the typical magnitudes of total TC motion (advection + propagation). The Beta and Shear vectors in Fig. 4.10b also differ by about 0.4 m/s, which results in Advection and Motion vectors at $r = 4$ that closely approximate those at $r = 2$. In contrast to Fig. 4.7c, the phase of interaction flow vorticity
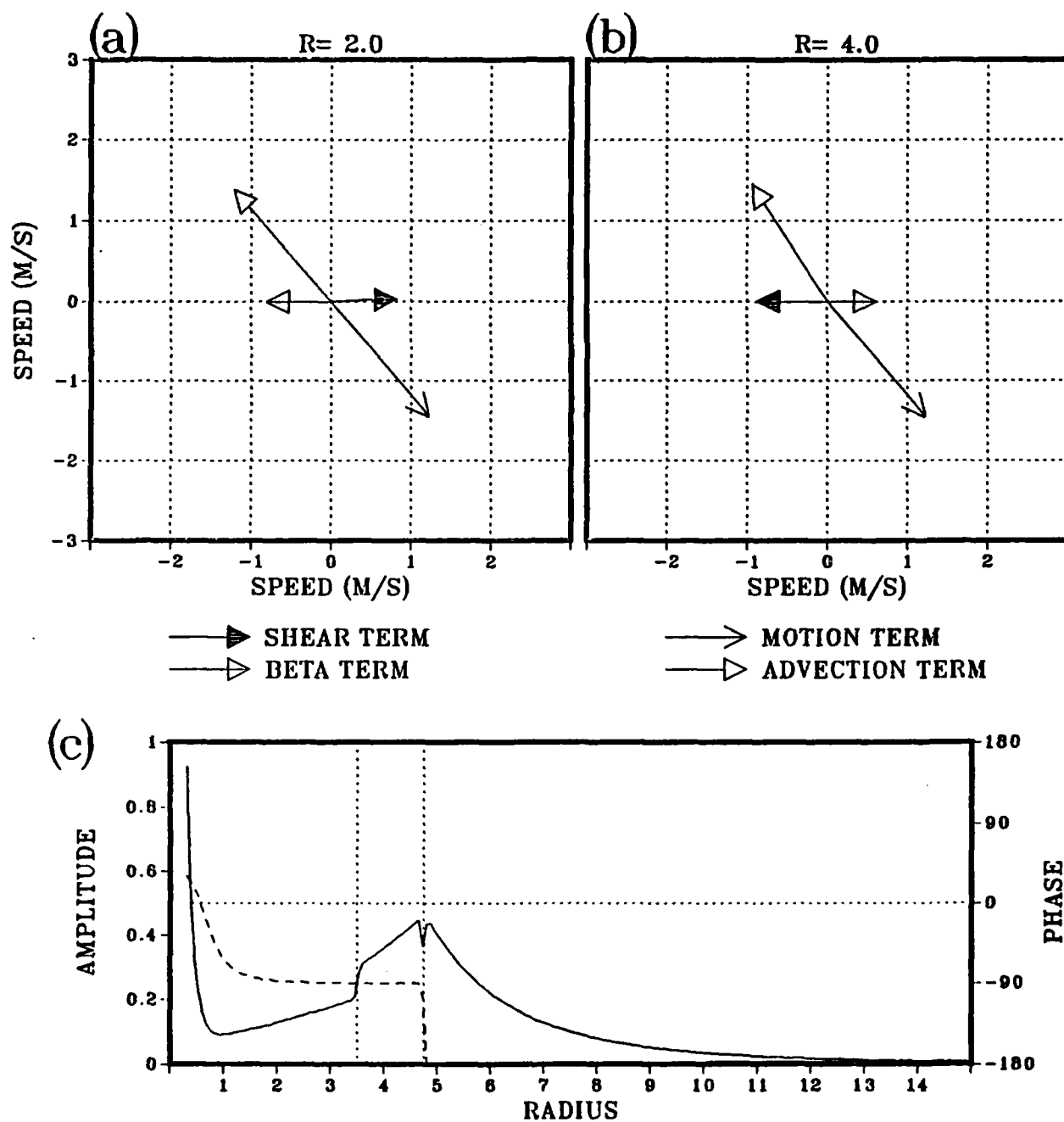
Fig. 4.8 (a)-(c) As in Fig. 4.7, except using the analytical model solution based on $C_* = 1.9$ m/s and $\alpha = 130$.
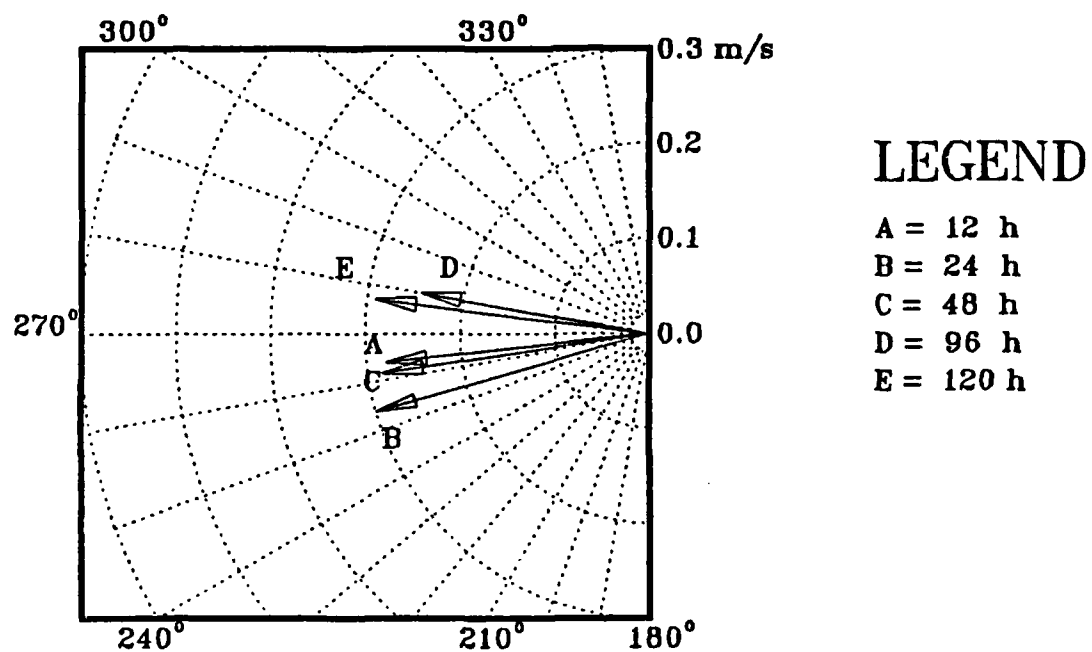
Fig. 4.9 Vector differences between the TC propagation and an averaged interaction flow velocity (0-300 km) at various times (see legend) during a 120 h integration of a barotropic numerical model (Fiorino and Elsberry 1989).
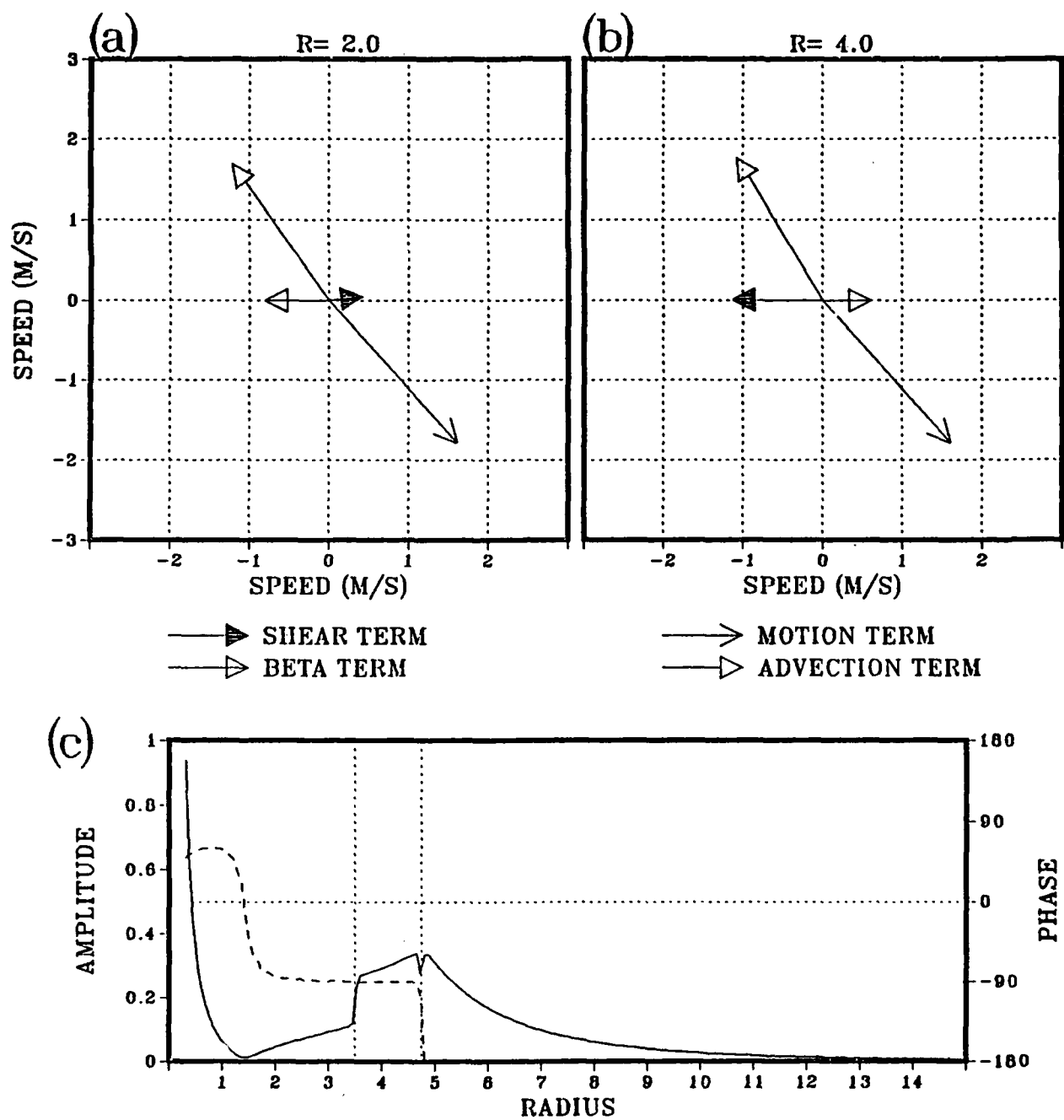
Fig. 4.10 As in Fig. 4.7, except using the analytical model solution based on $\hat{C}$. = 2.4 m/s and $\alpha = 132$.

is constant for $1.5 \leq r \leq R_T$ in Fig. 4.10c, which indicates that the vector patterns in Fig. 4.10 are characteristic of most of the Self-advection Region. Such consistency of the vorticity tendency balance is to be expected for a TC propagating as a quasi-steady entity, and supports the dynamical validity of both the theoretical model and the modified closure scheme.

It should be noted that the phase of ζ_A changes abruptly for $r<1.5$. In addition, the amplitude of ζ_A increases quite rapidly and actually becomes singular at the origin. Both of these properties are characteristic of an intense "inner gyre" in the vorticity field of the interaction flow, which must exist to balance the singular nature of the piecewise-analytic symmetric flow at the origin. Thus, the inner vorticity gyre may be purely an artifact of this theoretical model. By contrast, numerical modeling studies suggest that such inner vorticity gyres result from a dynamical instability which is supported by the barotropically unstable structure of typical TC tangential wind profiles (e.g., Willoughby 1988; Peng and Williams 1989). Similar gyre patterns have been suggested by aircraft observations of the inner wind fields of a TC, although these may be to some extent due to mislocating the TC center. In this model, the inner gyres have no significant impact on the propagation prediction capability of the internal closure scheme just demonstrated.

The usefulness of the internal closure scheme depends on the "closure" vector pattern (i.e., Fig. 4.10a) occurring at a well-defined and unique location in the $\hat{C}$ and α parameter space. By showing that the vorticity tendency vector pattern changes distinctly in response to small adjustments of $\hat{C}$ and α away from the "closure" values, Figs. 4.11-4.14 verify that the closure point may be quite precisely located. Changes in α to 137° (Fig. 4.11) and 127° (Fig. 4.12) induce a meridional component into the Shear vector. In contrast, changes in $\hat{C}$ to 2.1 m/s (Fig. 4.13) and to 2.7 m s (Fig. 4.14) tend to alter the relative magnitudes of the Beta and Shear vectors, although the processes are coupled to a moderate extent. The phase uniformity of ζ_A in the Self-advection Region is rapidly altered (Fig. 4.11c and 4.12c) when the specified propagation direction differs by only ±5° from the correct value. Although all closures in this research are obtained via interactive computer graphics, the well-defined nature of the closure vector pattern should be amenable to computer automation. A formal proof that only one closure pattern exists for a particular set of TC and environment parameters has not been attempted. However, a careful search over a wide range of imposed propagation velocities has never revealed more than one closure point in $\hat{C}$ and α parameter space.

(a) R= 2.0

(b) R= 4.0

SHEAR TERM   MOTION TERM
BETA TERM   ADVECTION TERM

(c)
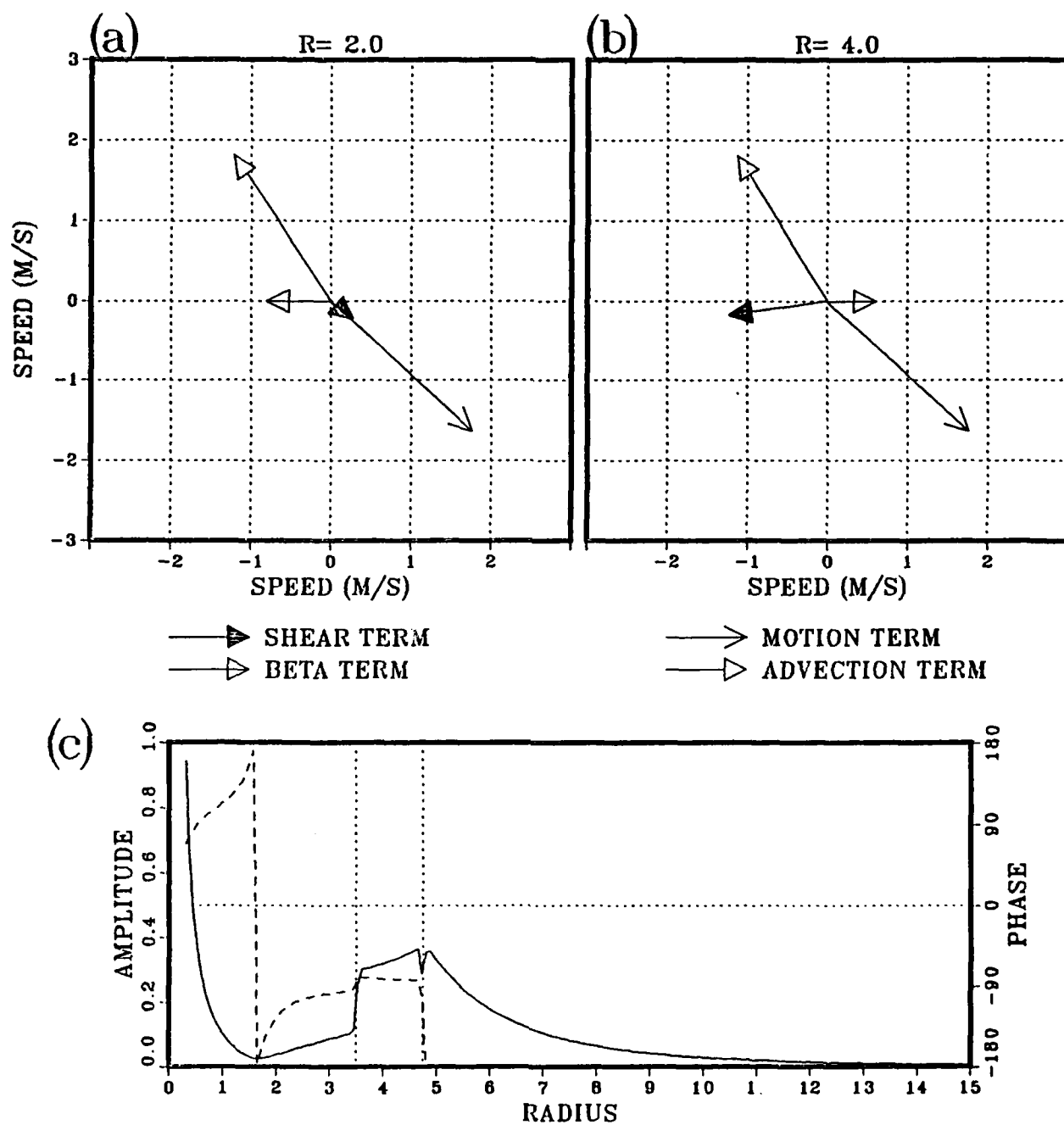
Fig. 4.11 As in Fig. 4.10, except using $\hat{C}_* = 2.4$ m/s and $\alpha = 137$.

80
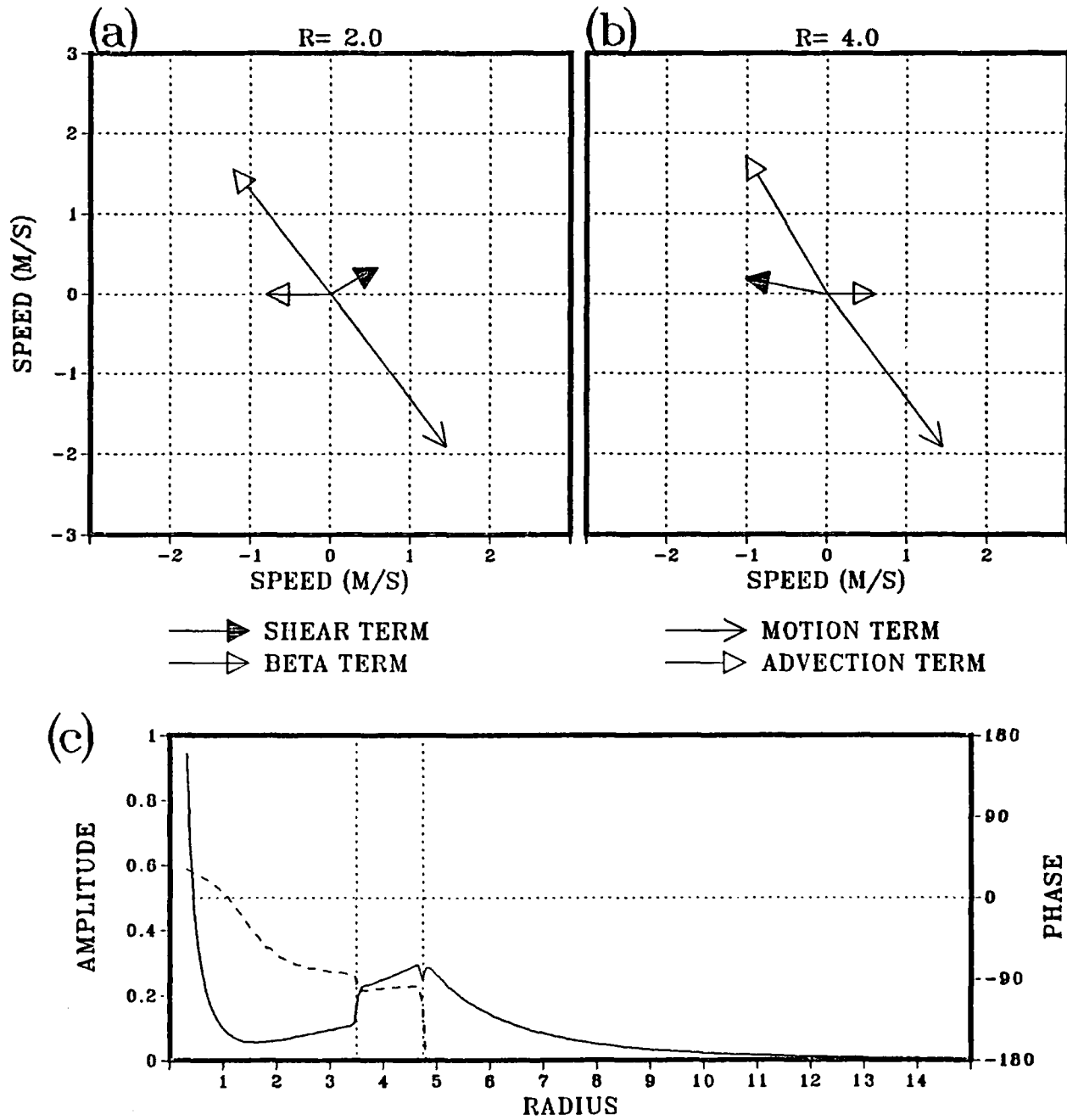
Fig. 4.12 As in Fig. 4.10, except using $\hat{C}_* = 2.4$ m/s and $\alpha = 127$.
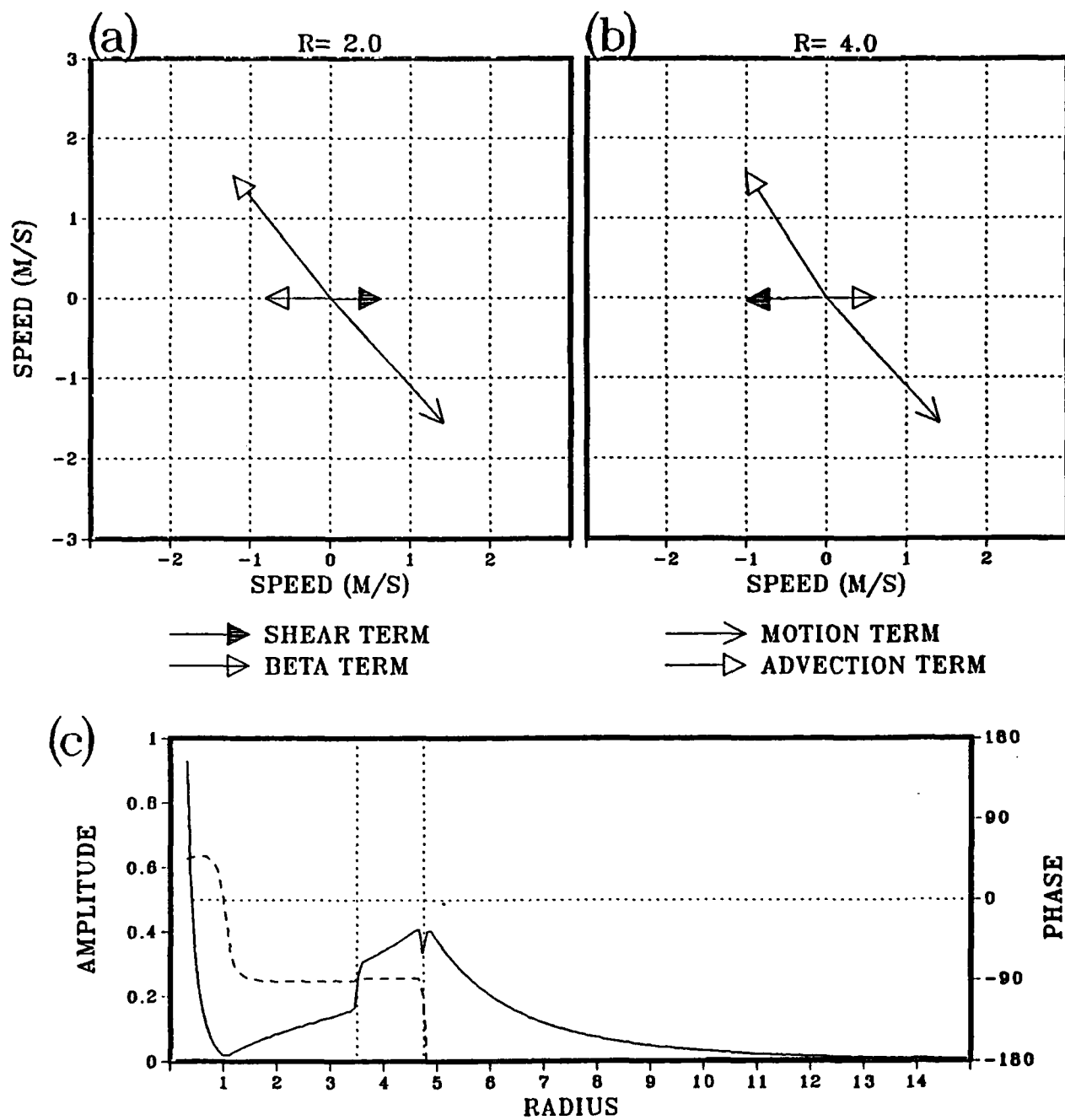
Fig. 4.13 As in Fig. 4.10, except using $\hat{C}_* = 2.1$ m/s and $\alpha = 132$.
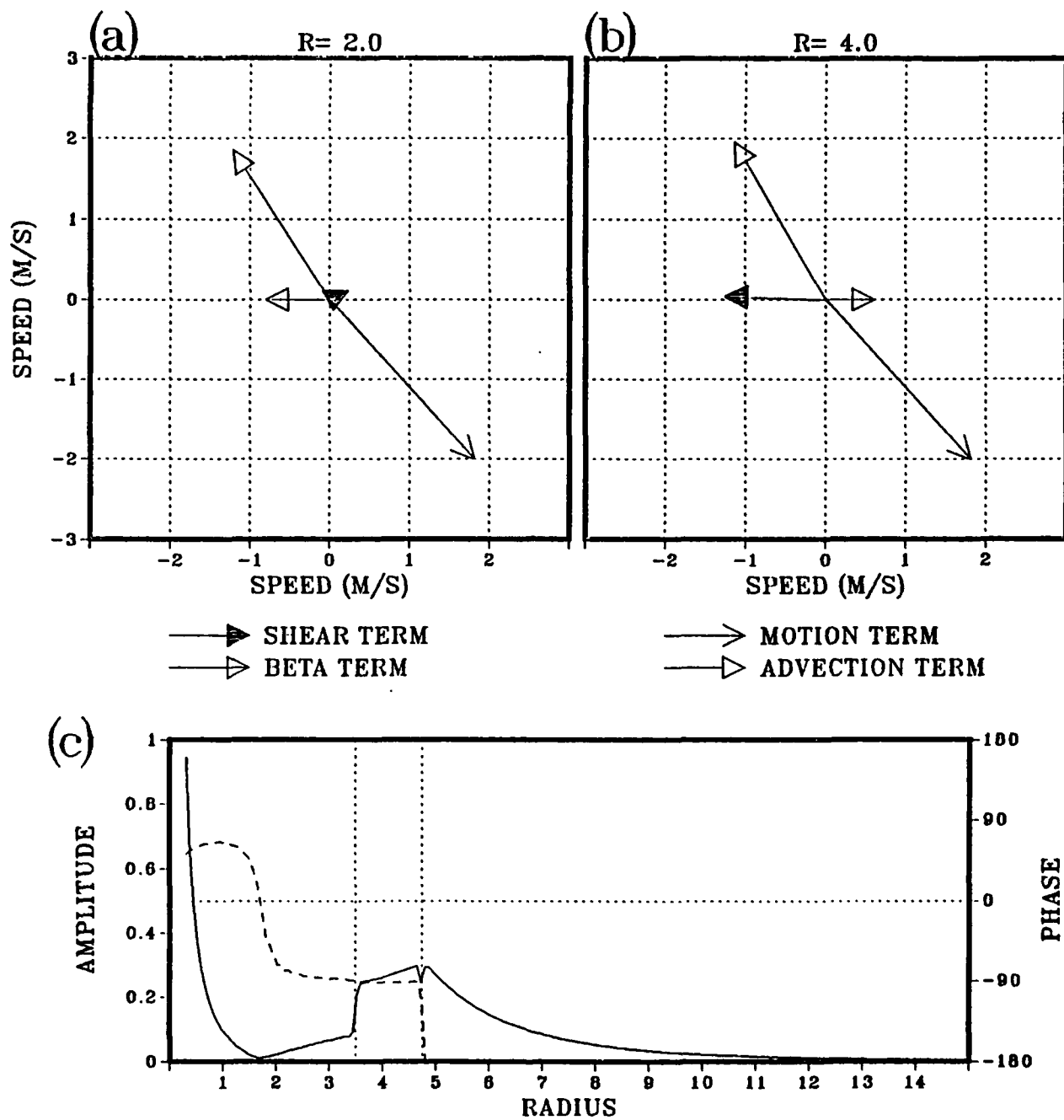
Fig. 4.14 As in Fig. 4.10, except using $\hat{C}_* = 2.7$ m/s and $\alpha = 132$.

The closure scheme quite precisely locates a "predicted" direction of propagation that is 12° to the left of the actual value found by FE. The cause for most of this bias is that the phase of ψ_A converges to a value of 9° at large radii (Fig. 4.15), rather than to zero, as would occur in a quiescent environment if the Dispersion Region equation was solved over the entire model domain. The mathematical basis for this property of the solution is that in (4.17a) the terms associated with the inner boundary condition and to first order the forcing term $G_2/2r$ both decay proportional to r^{-1} for $r \gg R_T$. As a result, the symmetric angular windshear that produces the barotropically stable downshear phase shift in and near the Self-advection Region (Fig. 4.15; $r \lesssim 8$) still has a small but measureable influence in the Dispersion Region at large radii. Since the phase shift of ψ_A at large radii may always be computed from the model solution, the closure-predicted propagation direction could be corrected by this angle to increase the accuracy of the model for applications in which a precise direction prediction would be of particular importance (*e.g.*, a propagation + advection track forecasting aid). Such directional corrections will not be used here. As will be shown in Chapter V, the corrections are not required when using this model to initialize a numerical model.

The accuracy of the internal closure scheme developed above may be put into perspective by computing the 24 h forecast errors that would result solely from speed and direction errors of 0.25 m s and 12°, which represent the difference between the propagation predicted here via the internal closure scheme and that observed by FE. The speed error translates into ≈ 25 km of forecast error. Assuming a typical TC propagation velocity of 2.5 m s, the direction error can cause ≈ 45 km of forecast error. These errors are about one quarter of the typical 24 h official forecast error (*e.g.*, Thompson *et al.* 1981), and thus would be of secondary importance compared to errors induced by poor, inadequate observations.

3. Sensitivity testing

a. Transition radius adjustments

This model contains two potentially adjustable features: the location of the transition radius as determined by δ in (4.19), and the requirement for a relatively small change in $|\zeta_A|$ at $r = R_T$, which may be defined in terms of the parameter γ by

$$\gamma \equiv \lim_{r \to R_T} \frac{|\zeta_A(r_+)|}{|\zeta_A(r_-)|} .$$

(4.26)
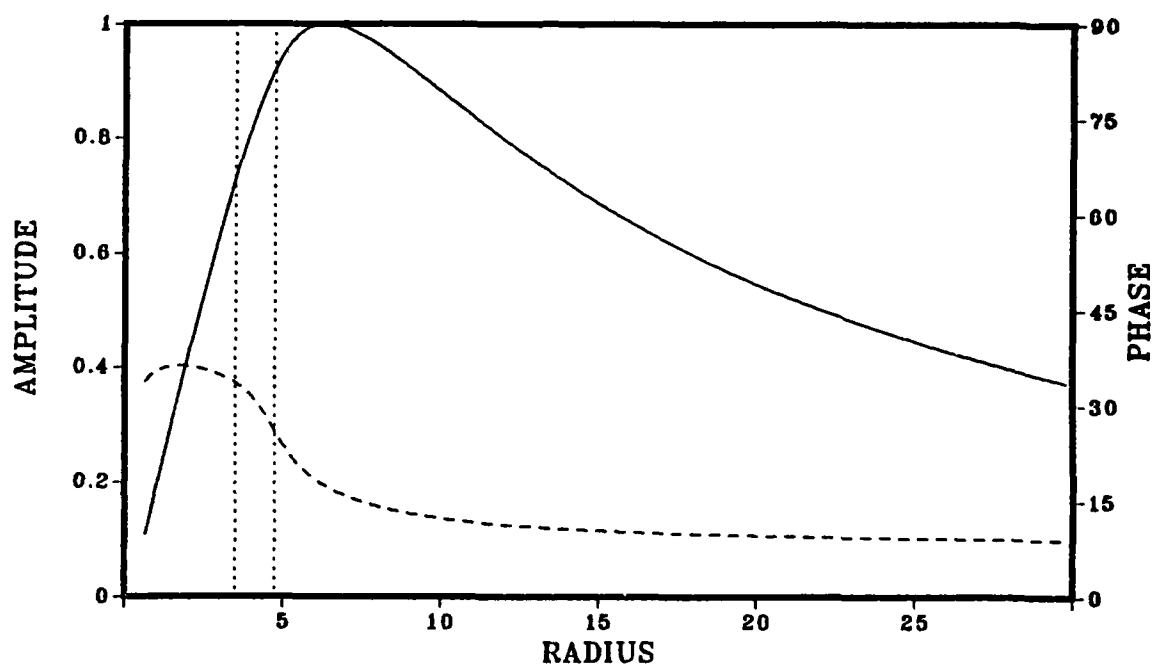
Fig. 4.15 Radial profile of streamfunction amplitude (solid) and phase (dashed) corresponding to vorticity profile shown in Fig. 4.10c. The amplitude curve has been normalized by the maximum amplitude of the streamfunction.

Thus, it is important to test the sensitivity of the closure scheme to moderate adjustments of these conditions, and also to determine whether any physically unreasonable changes occur in the predicted wavenumber one gyre structure.

Table 4.1 is a summary of the sensitivity tests performed, including the resultant changes in T_{adj}. Test 1 and (2) shows that decreasing (increasing) R_T results in a less (more) westward direction of propagation, and a slower (faster) speed of propagation. In contrast, decreasing (increasing) γ in Test 3 (4) results in a less (more) northward direction of propagation, and a slower (faster) speed of propagation. Since changes in γ are accomplished by adjusting T_{adj} in (4.17b), Table 4.1 includes the values of T_{adj} to show that changes in T_{adj} are approximately proportional to the changes in $\hat{C}$, which is consistent with the idea that a stronger outer gyre structure will contribute to stronger interaction flow across the center of the TC. In each test, the phase of ψ_A at large radii was found to be similar in magnitude to that noted above (e.g., Test 3, 11.1°; Test 4, 7.5°). In Test 4, the predicted propagation speed and direction are quite close to FE's 2.65 m/s at 330° ($\alpha = 120°$). The wavenumber one gyre structure associated with the $\hat{C}$ and α of Test 4 is shown in Fig. 4.16. If the wavenumber two component

Table 4.1 Response of the model-predicted propagation velocity (columns 5,6) to four combinations of the parameters δ (column 2) and γ (column 3) as defined by (4.19) and (4.26) respectively.

Test	δ	γ	T_{adj} (h)	$\hat{C}$ (m/s)	α (deg)
1	0.95	1.0	40.3	2.20	130
2	1.05	1.0	62.0	2.60	135
3	1.00	0.8	39.3	2.15	139
4	1.00	1.2	59.3	2.65	128
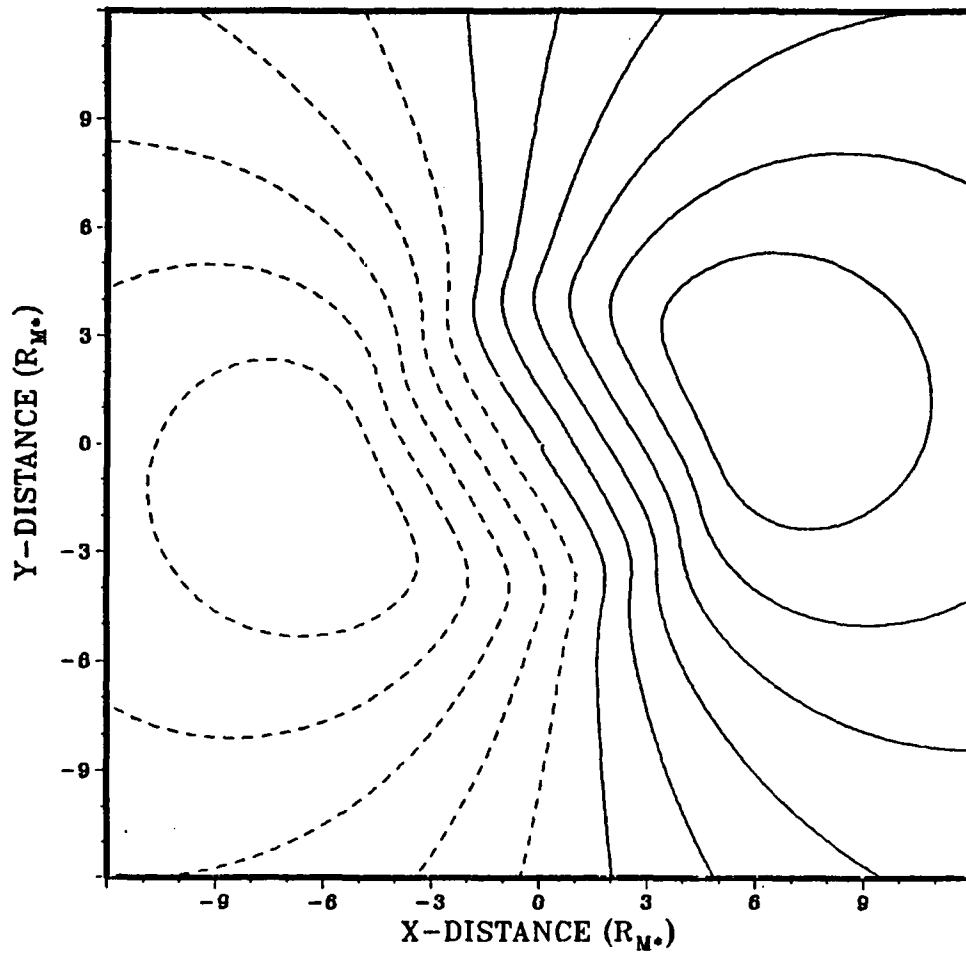
Fig. 4.16 As in Fig. 4.5, except using the parameter specifications of Test 4 of Table 4.1.

is ignored, then the numerical result of FE (Fig. 4.4) is quite closely approximated by the theoretical result in Fig. 4.16. Thus, the sensitivity tests demonstrate that the theoretical model depends of the adjustable parameters in a well-defined and physically reasonable manner.

b. Piecewise-analytic symmetric TC specification

The piecewise-analytic TC winds profile (Fig. 4.2a) used above was constructed so that the associated vorticity gradient (Fig. 4.2b) is continuous and equal to the analytic vorticity gradient at the transition radius. In contrast, the piecewise-analytic vorticity gradient is discontinuous at the interface R_1 and only approximates the analytic vorticity gradient in an average sense. The motivation for approximating the analytic vorticity profile in this manner may be illustrated by determining the model-predicted propagation for the piecewise-analytic profiles in Fig. 4.17. Note that the piecewise-analytic wind profile approximates the analytic wind profile more closely than in Fig. 4.2a. In contrast, the piecewise-analytic vorticity gradient is now discontinuous and only poorly approximates the analytic profile at both R_1 and R_T. The model-predicted propagation using the parameters of the figure inset is $\hat{C} = 1.75$ and $\alpha = 144°$, which deviates significantly from FE's results of 2.65 m s and 330° ($\alpha = 120$).

The cause of this important error in model-predicted propagation may be determined by eliminating the processes that cannot be responsible. Since the piecewise-analytic wind profiles in Figs. 4.2a and 4.17a are nearly identical, the change in predicted propagation cannot be attributed to the Beta or Shear terms of (4.25). That is, the asymmetric forcing associated with a planetary vorticity gradient and the symmetric angular windshear-induced stability of the TC remain essentially unchanged. The change in the piecewise-analytic vorticity gradient in the Dispersion Region cannot be responsible since self-advection processes are excluded there. The rough agreement between the piecewise-analytic and analytic vorticity profiles inside R_1 are also quite similar in Figs. 4.2b and 4.17b, and FE have shown conclusively that changes in the symmetric TC inside 300 km have a negligible effect on propagation. Thus, it must be concluded that the significant reduction in the average magnitude of the piecewise-analytic vorticity gradient in the outer annulus of the Self-advection Region must be responsible for the change in predicted propagation. Since the piecewise-analytic vorticity gradient roughly brackets the analytic curve in Fig. 4.17b near R_1, the underestimation of the analytic vorticity gradient just inside the transition radius is inferred to be the source of the error in predicted propagation.

88
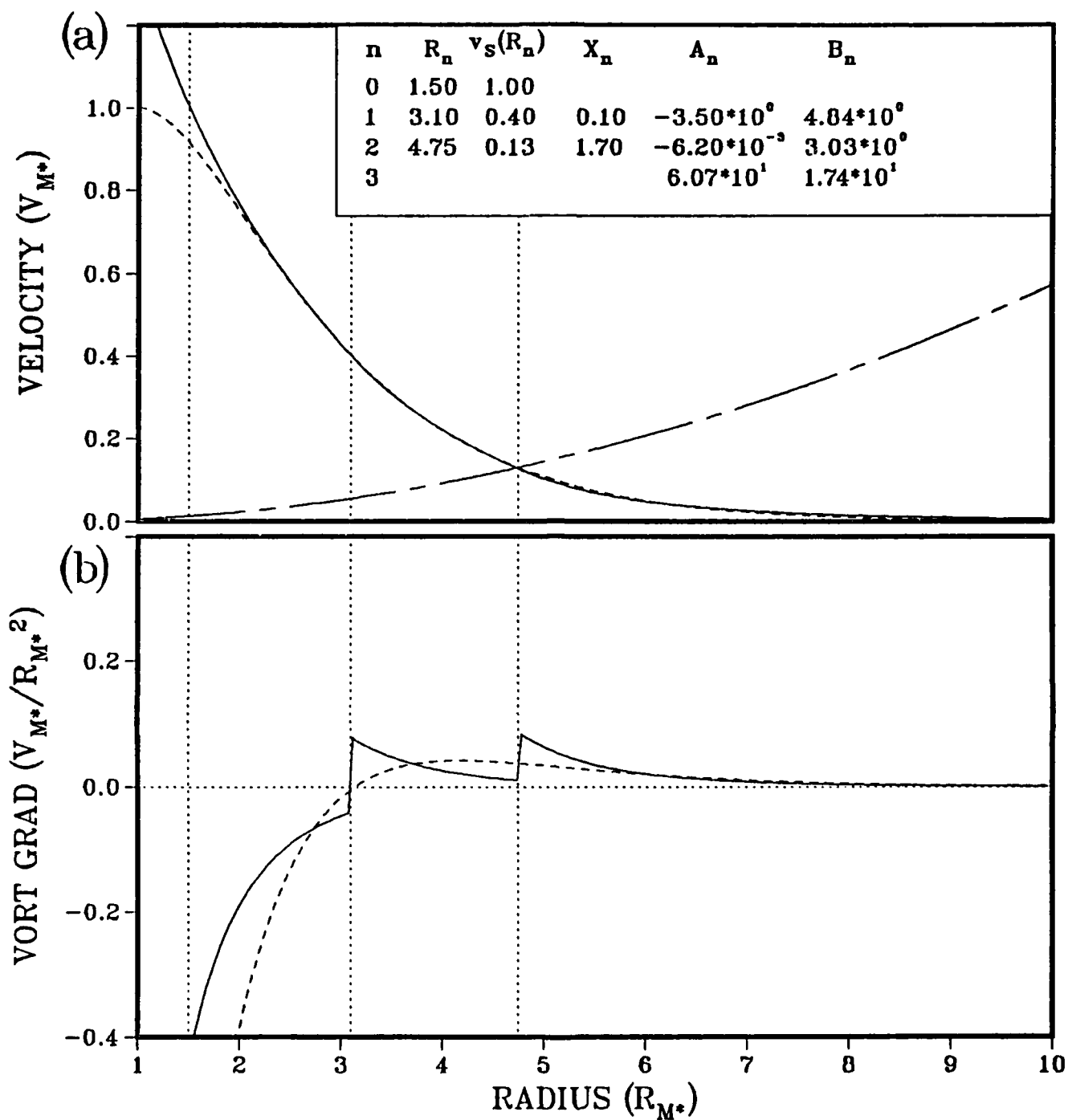
Fig. 4.17 (a)-(b) As in Fig. 4.2, except that the parameters (inset) of the piecewise-analytic TC wind structure have been changed so that the associated vorticity gradient is no longer continuous and equal to the analytic value at the transition radius (r = 4.75).

This analysis suggests that the sensitivity of TC propagation on wind strength in a 300-800 km "critical annulus" demonstrated by FE is actually a manifestation of the sensitivity of the self-advection process to the radial gradient of symmetric TC vorticity via the Advection term of (4.25). Thus, barotropic TC propagation actually depends on the second derivative of the symmetric windfield in the critical annulus, which explains why seemingly modest changes in outer wind strength as used by FE can cause significant changes in propagation. The piecewise-defined nature of the present theoretical model tends to concentrate this dependence near the transition radius, and also exaggerate the dependence by enabling very similar piecewise-analytic wind profiles to have associated vorticity profiles that differ more severely than similar analytic profiles.

D. MODEL RESULTS PART II: INTERNAL CLOSURE

The availability of an internal closure scheme permits this model to predict TC propagation for various TC wind profiles and environmental influences. Efforts are presently underway to compute TC propagation relative to horizontally variable environmental winds from numerical models (personal communication, R. T. Williams 1989). However, no published results are available against which the above internal closure may be compared. Thus, it will be assumed that the closure scheme with $\delta = 1$ and $\gamma = 1$ will give results of comparable accuracy when applied with spatially variable environmental winds. An internal check of the likely accuracy of the prediction can be made by comparing the closure vector plot for dynamical consistency with the associated gyre structure predicted by the model for various environmental windfields.

1. Influence of TC structure change

Chan and Williams (1987; CW) also used (4.22) to specify the initial TC windfield, and varied TC intensity and strength simultaneously by adjusting the parameter V_M with $b = 1$. Three of their parameter specifications (Table 4.2; columns 2-4) will be used here. In light of the closure testing above, the piecewise-analytic profiles (Figs. 4.18-4.20) have been constructed so that the analytical vorticity gradients are accurately approximated near the transition radius. Note also the increase in the transition radius (Table 4.2; column 5) in response to larger values of V_M. The comparison of the theoretically-predicted propagation speeds and directions with those reported by CW (Table 2; columns 6,7) reveals slow speed biases and left direction biases quite similar to those in Section C above, which indicates that the model results are quite consistent with regard to changes in TC structure. As shown in subsection 3.a above, the persistent
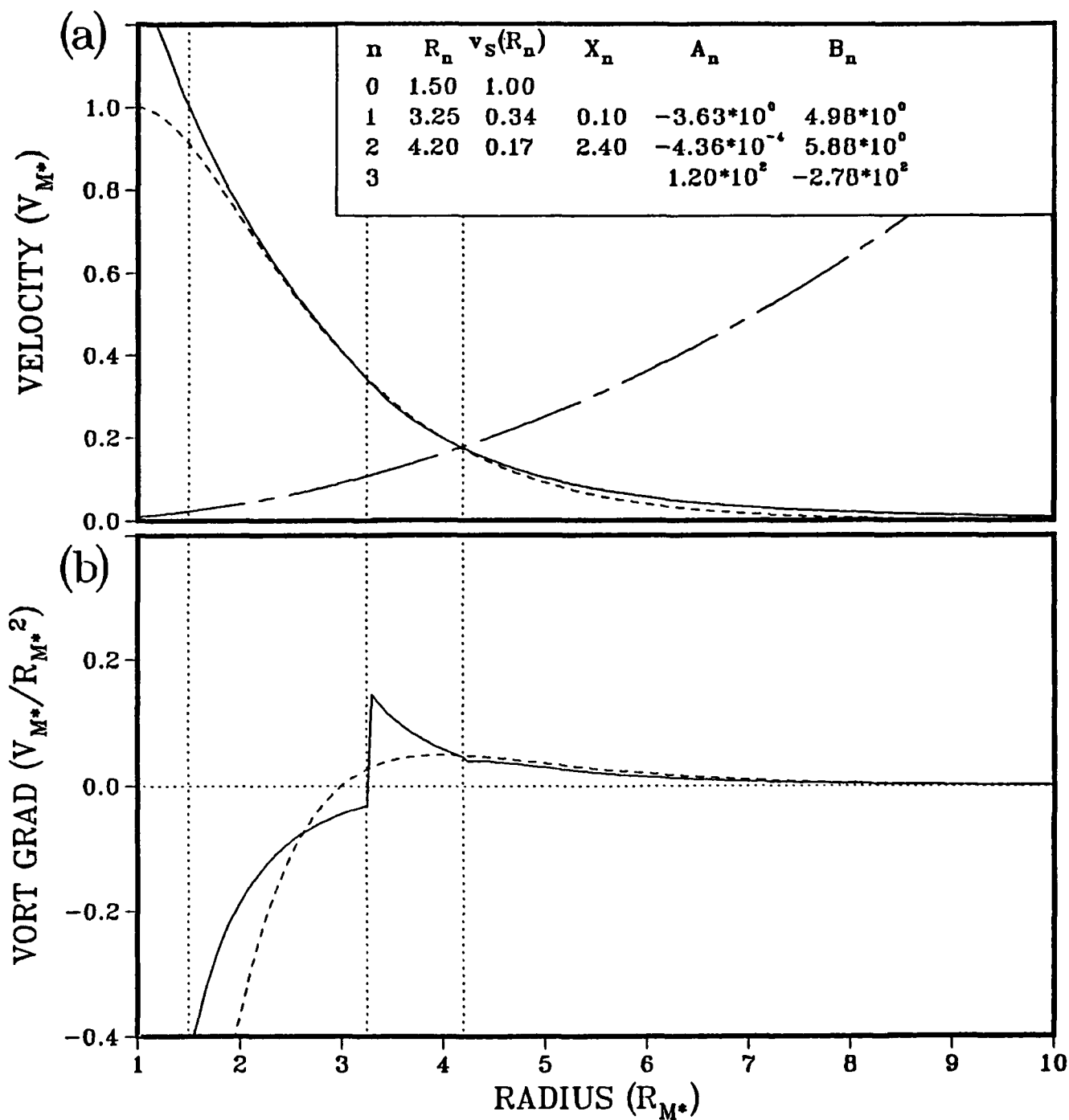
Fig. 4.18 As in Fig. 4.2, except using Chan and Williams (1987) analytic TC wind profile parameters of $V_{M^*} = 20$ m/s, $R_{M^*} = 100$ km and $b = 1.0$.
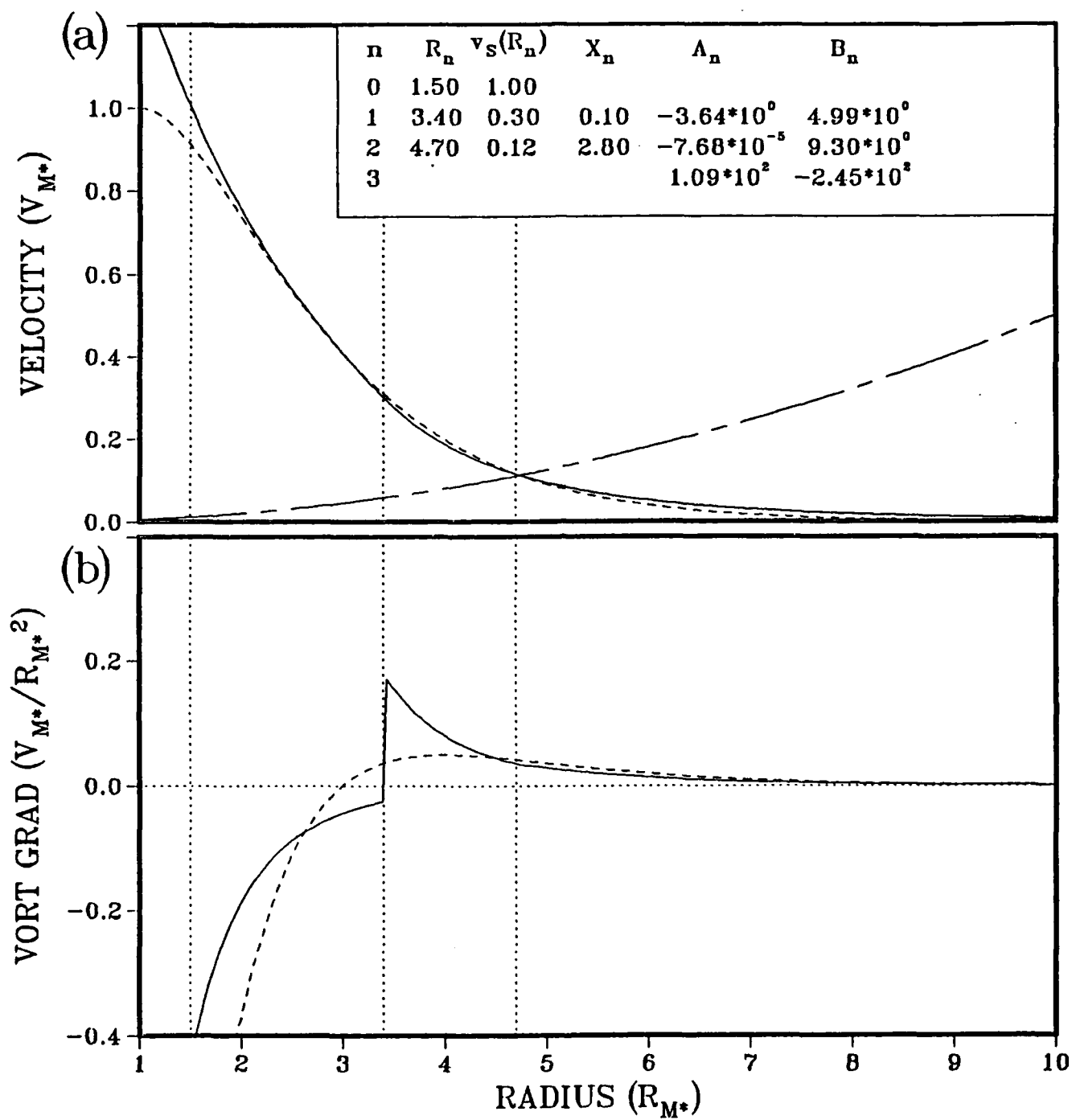
Fig. 4.19 As in Fig. 4.17, except for $V_{M*} = 40$ m/s.

n	R_n	$v_S(R_n)$	X_n	A_n	B_n
0	1.50	1.00			
1	3.50	0.28	0.10	$-3.62*10^0$	$4.96*10^0$
2	5.10	0.09	3.00	$-2.94*10^{-5}$	$1.21*10^1$
3				$1.02*10^2$	$-2.20*10^2$
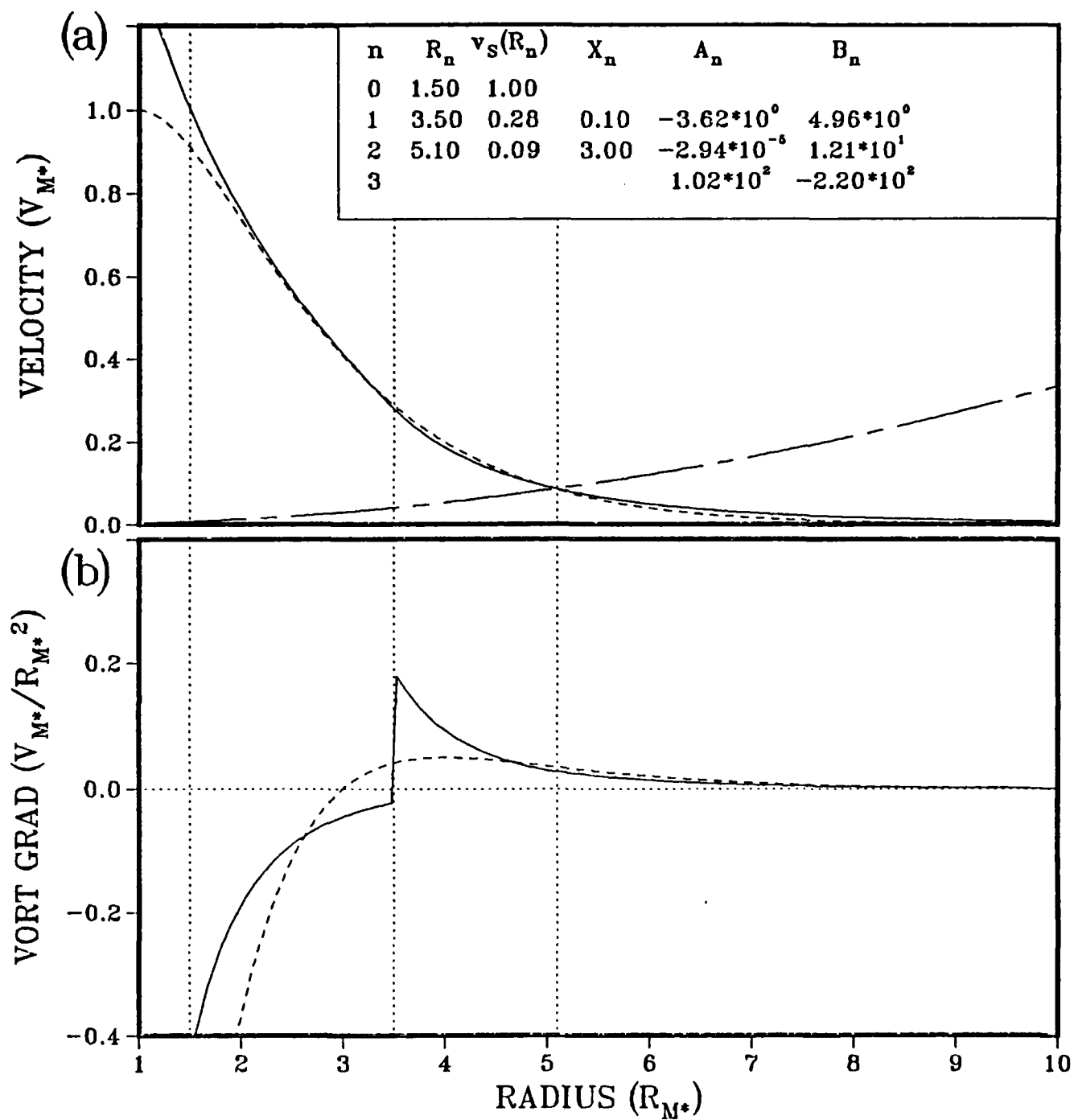
Fig. 4.20 As in Fig. 4.17, except for $V_{M^*} = 60$ m/s.

speed and direction biases could be reduced by moderately adjusting the parameters δ and γ.

It should be noted that the theoretically-predicted propagation directions in Table 4.2 are essentially independent of changes in TC structure, whereas FE noted a more westward propagation direction in response to increases in TC outer wind strength. The track of FE's "large-weak vortex" matched closely that of the "basic vortex" for the first 24 h, but became increasingly westward as the integration proceeded. Thus, it is possible that the numerical model includes some non-steady propagation process that is excluded from this steady-state model. An alternate explanation is that cyclic boundary conditions in the numerical model may have a significant impact on the propagation vector associated with a large and purely cyclonic vortex that radiates substantial amounts of Rossby wave energy (cf. Shapiro and Ooyama 1989). Althougth domain size tests were conducted by FE with the basic vortex, it does not appear that such tests were conducted for the large-weak vortex. The combined evidence of the theoretical results here and the numerical results of CW suggest that changes in TC strength result primarily in changes in propagation speed, but not propagation direction.

Table 4.2 TC propagation velocity (columns 6,7) predicted by the theoretical model and the numerical model (in parentheses) of Chan and Williams (1987) for three values of maximum symmetric wind (column 2). The analytic and piecewise-analytic curves used by the numerical and theoretical models respectively are shown in Figs. 4.18-4.20.

Case	V_M (m s)	R_M (km)	b	R_T	$\dot{C}$ (m s)	α (deg)
1	20	100	1.0	4.2	1.95 (2.0)	130 (121)
2	40	100	1.0	4.7	2.65 (2.8)	132 (121)
3	60	100	1.0	5.1	3.35 (3.75)	132 (118)

2. Influence of uniform environmental vorticity

The next step in complexity from β-induced TC propagation in a quiescent environment is to include a uniform environmental vorticity field, *i.e.*, $Z_E \neq 0$, $\nabla \zeta_E' = 0$. Examples of this situation would be: i) approximating the trade winds as a nondivergent zonal flow with linear meridional shear; and ii) approximating the subtropical ridge (monsoon trough) region as a large-scale anticyclone (cyclone) that is in solid body rotation (cf. Willoughby 1988).

Table 4.3 is a summary of the closure results for four different values of environmental relative vorticity using the same piecewise-analytic TC as in Case 2 of Table 4.2. Recalling that closure occurs at $\hat{C}_\bullet = 2.65$ m/s, $\alpha = 132°$ for Case 2 of Table 4.2, a cyclonic (anticyclonic) environmental vorticity induces a counterclockwise (clockwise) adjustment in the direction of TC propagation that is proportional to the magnitude of Z_E. Note that the theoretical model also predicts a greater TC propagation speed as Z_E progresses from anticyclonic to cyclonic, which suggests that TC propagation may be a more dominant component of total TC motion in regions of large-scale cyclonic vorticity such as the monsoon trough. Although no numerical model confirmation exists for this

Table 4.3 Theoretically-predicted propagation velocity (columns 3,4) for four values of uniform environmental vorticity (column 2).

Case	Z_E ($\times 10^{-5}$ s^{-1})	$\hat{C}_\bullet$ (m s)	α (deg)
1	-0.5	2.30	122
2	+0.5	3.00	141
3	+1.0	3.30	150
4	+1.5	3.55	162

aspect of the prediction, it is consistent with the faster propagation of westward moving TC's in composite data (Fig. 1.1b). The wavenumber one gyre patterns associated with Cases 1 and 4 of Table 4.3 are shown in Fig. 4.21a and b respectively. Chan and Williams (1989) have noted gyre orientation and propagation changes in an equivalent numerical simulation that are consistent with the results given here.

It is important to note that this model cannot be internally closed if Z_{E^*} is much less or greater than the range of values in Table 4.3. The mathematical explanation for this problem is that the solution for ζ_A in the Dispersion Region depends inversely on Z_{E^*}. For sufficiently large values of environmental vorticity, it becomes impossible to iterate to a value of T_{adj^*} such that the magnitude of ζ_A is continuous at the transition radius. From a dynamical perspective, the assumptions $V_E \ll V_S$ and $\zeta_E \ll \zeta_S$ become unacceptably inaccurate in the outer part of the Self-advection Region. As a result, the present form of the theoretical model can accomodate only moderate values of large-scale vorticity, and should not be applied to situations involving interaction of the TC with an intense cyclonic system such as another TC. Such situations might be addressed by extending the model to include some of the higher-order wavenumber one processes that were excluded here (Chapter II).

3. Influence of environmental vorticity gradients

To determine the model response to gradients of absolute vorticity, combinations of Z_{E^*}, β_{e^*} and ϕ are devised that approximate the horizontal variability of the typical large-scale environments through which TC's move. Figs. 4.22a and b illustrate parameter combinations that correspond to the regions south and north of the NW Pacific subtropical ridge respectively. As indicated, Z_{E^*} is assumed to be moderately anticyclonic in both regions. The westward component of the environmental vorticity gradient reflects the influence of the intense Asian heat low throughout much of the troposphere during the NW Pacific typhoon season. Similarly, the southward and northward components reflect the influence of the equatorial trough and midlatitude baroclinic regions respectively. Such parameter combinations produce an absolute vorticity gradient that is larger and is directed more poleward north of the subtropical ridge compared to south of the subtropical ridge (Table 4.4; columns 3,4). Although the analytic TC wind profile of Table 4.3 Case 2 is used for both cases here, an additional piecewise-analytic profile (Fig. 4.23) has to be constructed to account for the increased magnitude of β_{e^*} north of the subtropical ridge.

If the phase shift of the environmental vorticity gradient is taken into account, then the tendency vector patterns (Figs. 4.24a,b and 4.25a,b) from which the propa-
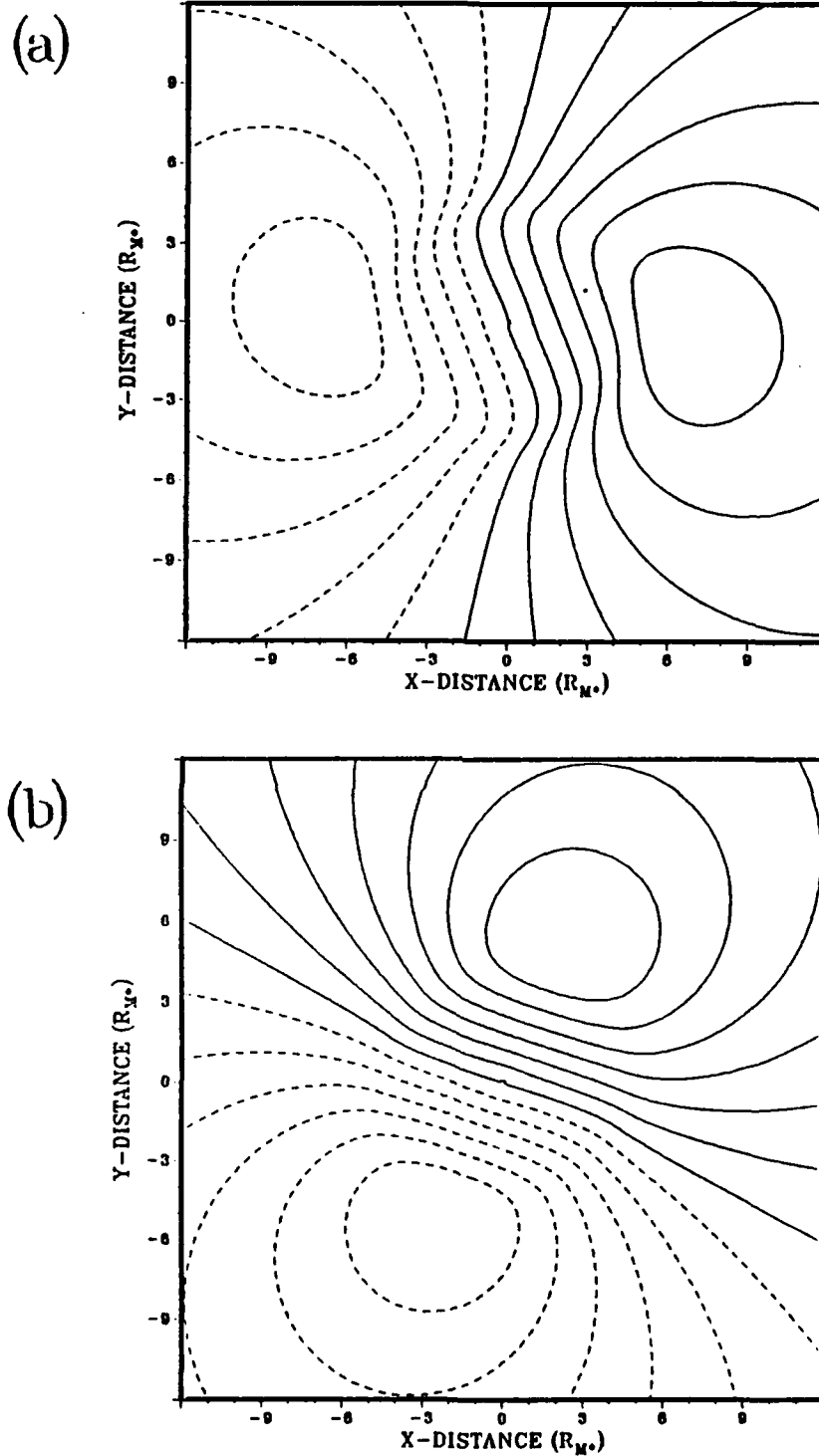
Fig. 4.21 Theoretically-predicted wavenumber one streamfunction fields for (a) Case 1 and (b) Case 4 of Table 4.3. Contour interval is $2 \times 10^5 m^2/s$.
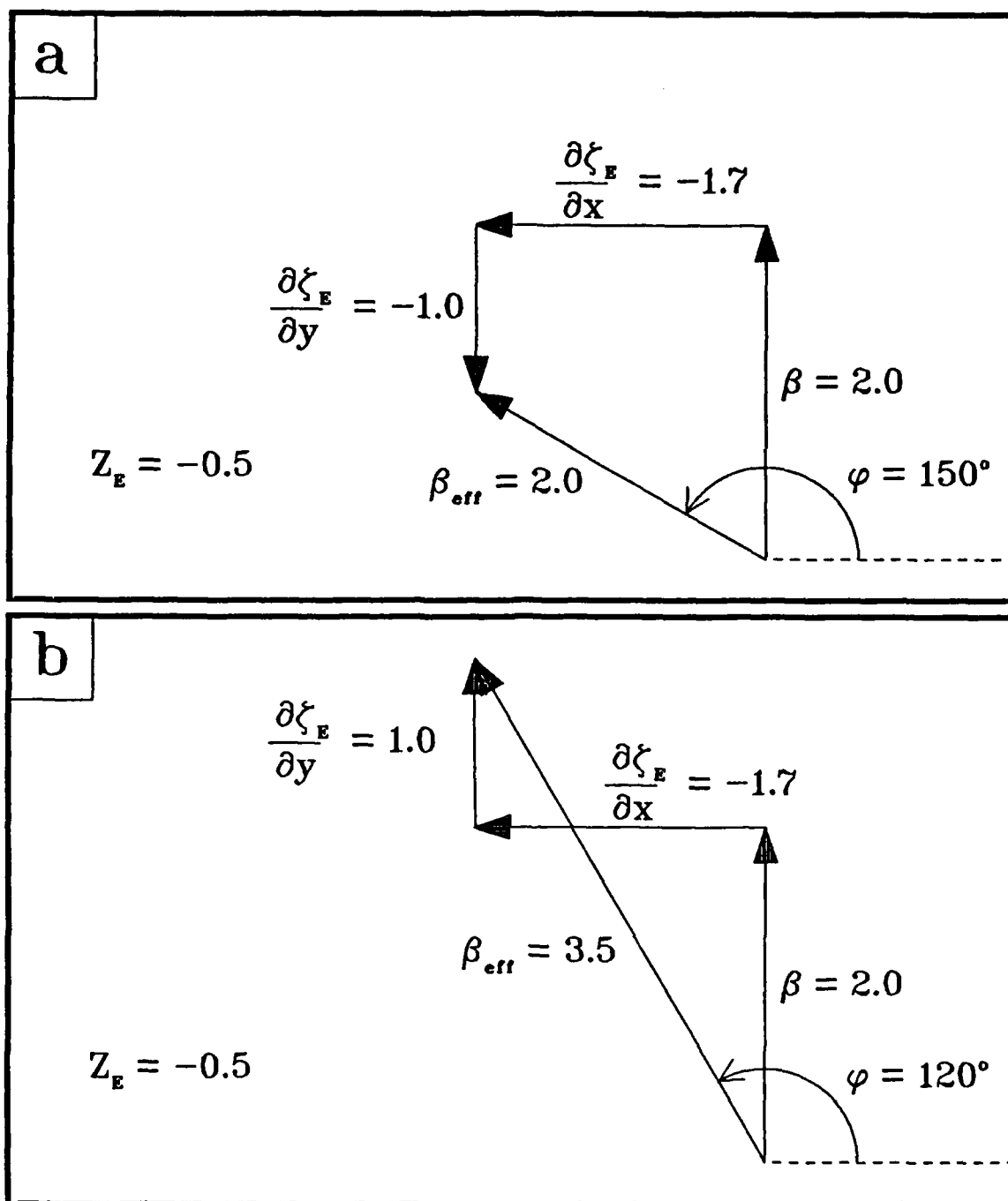
Fig. 4.22 Idealized planetary and environmental vorticity gradients for TC positions in an anticyclonic vorticity region (a) south and (b) north of the subtropical ridge in the lower to middle troposphere of the western North Pacific TC region. The units of the vorticity gradients are $10^{-11}m^{-1}s^{-1}$, and the units of Z_E are $10^{-5}s^{-1}$.

The table inset in panel (a):

n	R_n	$v_s(R_n)$	X_n	A_n	B_n
0	1.50	1.00			
1	3.25	0.33	0.10	$-3.69*10^{0}$	$5.05*10^{0}$
2	4.25	0.16	2.50	$-4.14*10^{-4}$	$6.43*10^{0}$
3				$1.03*10^{2}$	$-2.20*10^{2}$
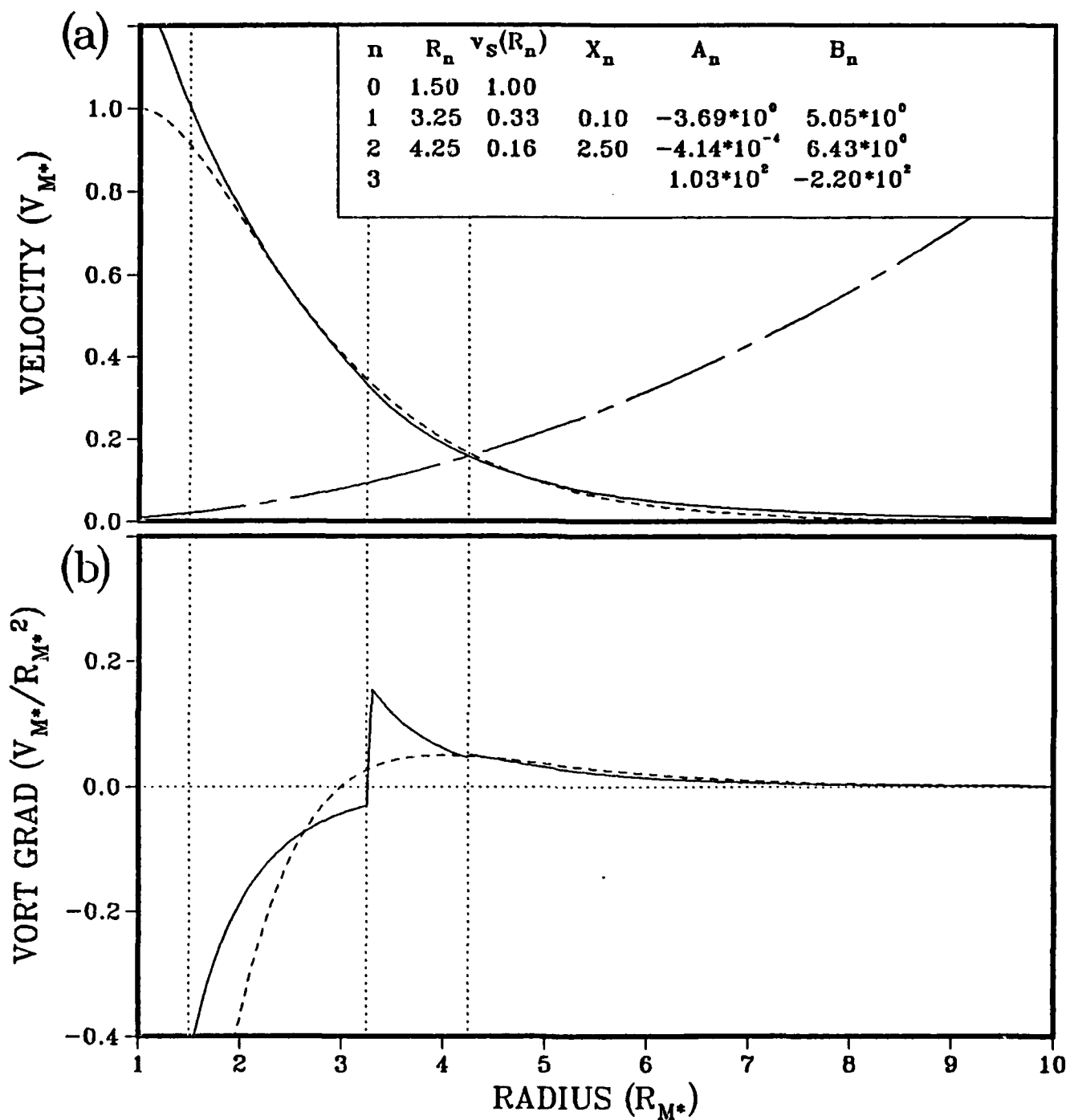
Fig. 4.23 As in Fig. 4.18, except that the piecewise-defined wind parameters (see inset) have been recalculated to account for $\beta_{eff} = 3.5 \times 10^{-11}\ m^{-1}s^{-1}$ in Fig. 4.21b.

gation velocities in Table 4.4 were obtained are consistent with those shown earlier (*e.g.*, Fig. 4.10). In each case, the Shear vector phase is opposite that of the Beta vector, which is now oriented 90° to the left of the direction of the environmental absolute vorticity gradient. The characteristic patterns in the radial profiles of interaction flow vorticity magnitude and phase are also evident (Figs. 4.24c and 4.25c). The orientation and amplitude of the wavenumber one gyre streamfunction are also dynamically consistent (Fig. 4.26), which suggests that the accuracy of the model with an environmental vorticity gradient included should be similar to the results shown earlier. Although equivalent numerical results are not available, the propagation directions predicted here are quite similar to the observed propagation directions for westward (pre-recurvature) and eastward (post-recurvature) moving TC's (Fig. 1.1b).

Table 4.4 Theoretically-predicted propagation velocities (columns 5,6) in response to environmental parameter combinations (columns 2-4) representing TC locations south (Case 1) and north (Case 2) of the subtropical ridge during the western North Pacific typhoon season.

Case	$Z_{\mathcal{E}}$ (x $10^{-5} s^{-1}$)	β_{eff} (x $10^{-11} m^{-1}s^{-1}$)	ϕ (deg)	$\hat{C}_{\star}$ (m/s)	α (deg)
1	-0.5	2.0	150	2.3	183
2	-0.5	3.5	120	2.9	156

E. SUMMARY

An analytical NDBT model based on the principle of nonlinear self-advection has been developed to predict the steady-state TC propagation and associated wavenumber one interaction flow induced by planetary and environmental forcing. The model has been made analytically tractable by dividing the highly complex and generally intractable TC propagation process into a number of manageable pieces via a number of reasonable assumptions. A piecewise-analytic solution for the wavenumber one interaction flow and the associated propagation velocity was then constructed from analytic solutions to
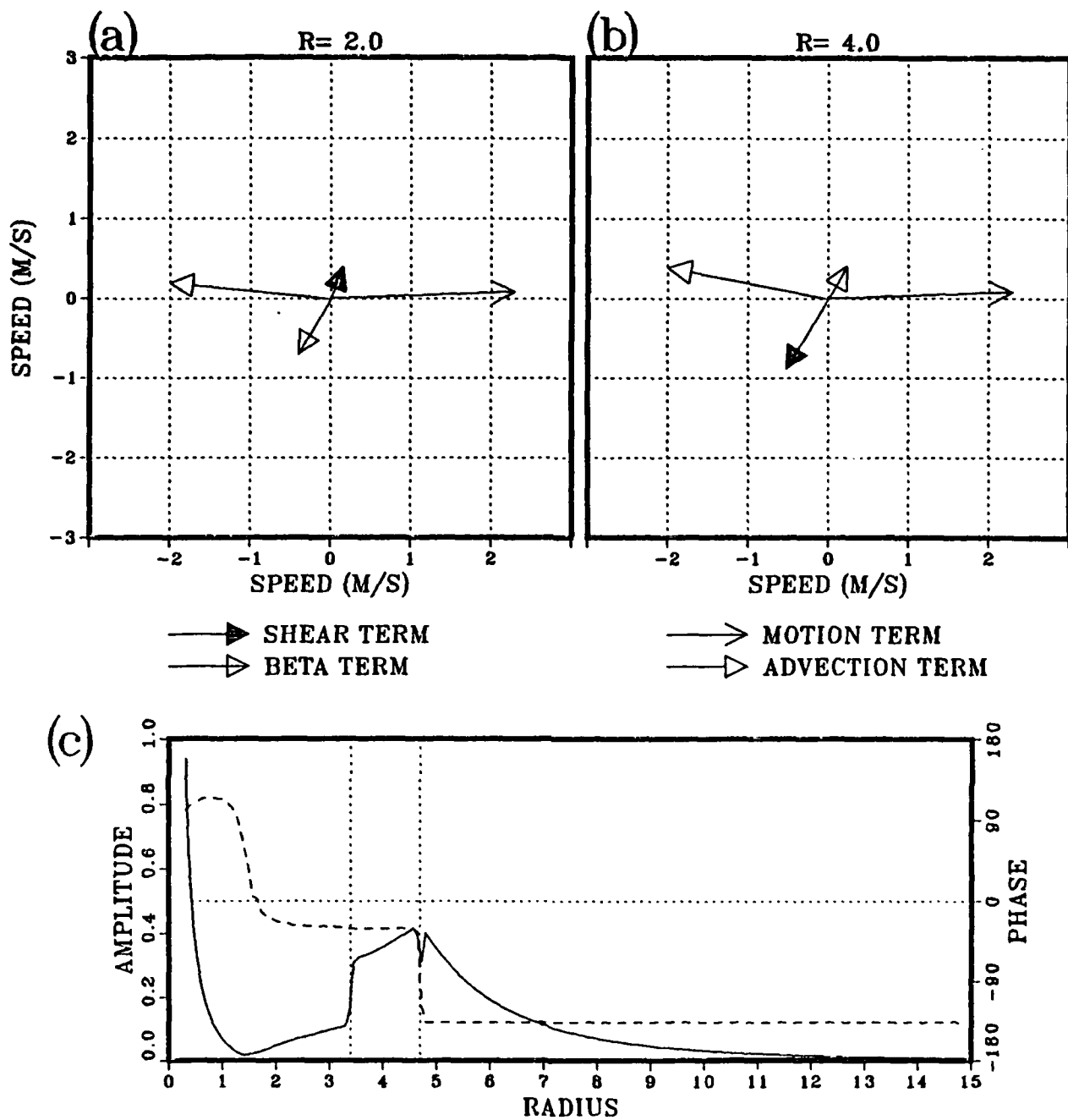
Fig. 4.24 (a)-(b) Vorticity tendency vector diagrams, and (c) vorticity amplitude and phase profiles as in Fig. 4.7, except for the model solution for Case 1 of Table 4.4.
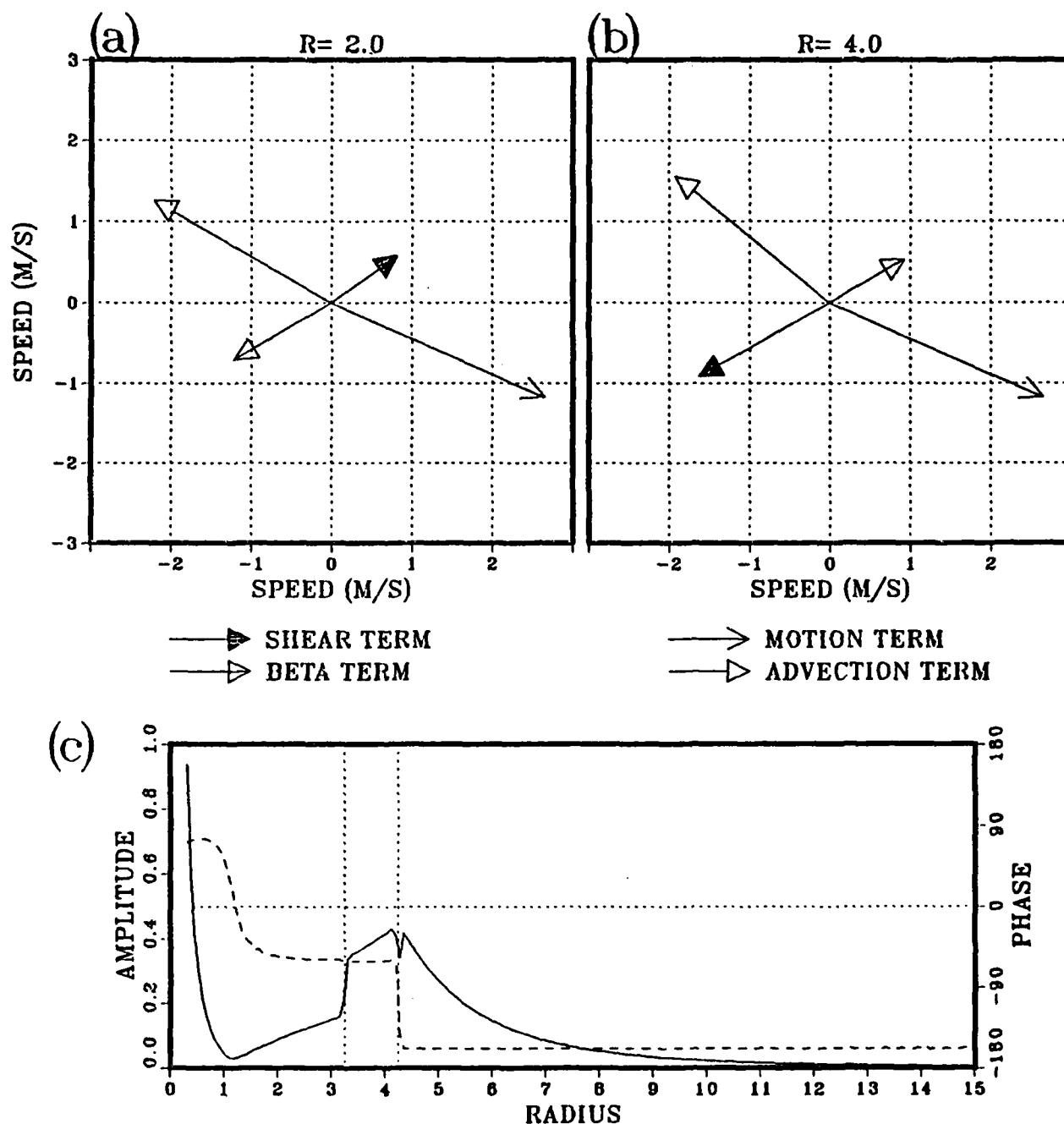
Fig. 4.25 As in Fig. 4.23, except for Case 2 of Table 4.
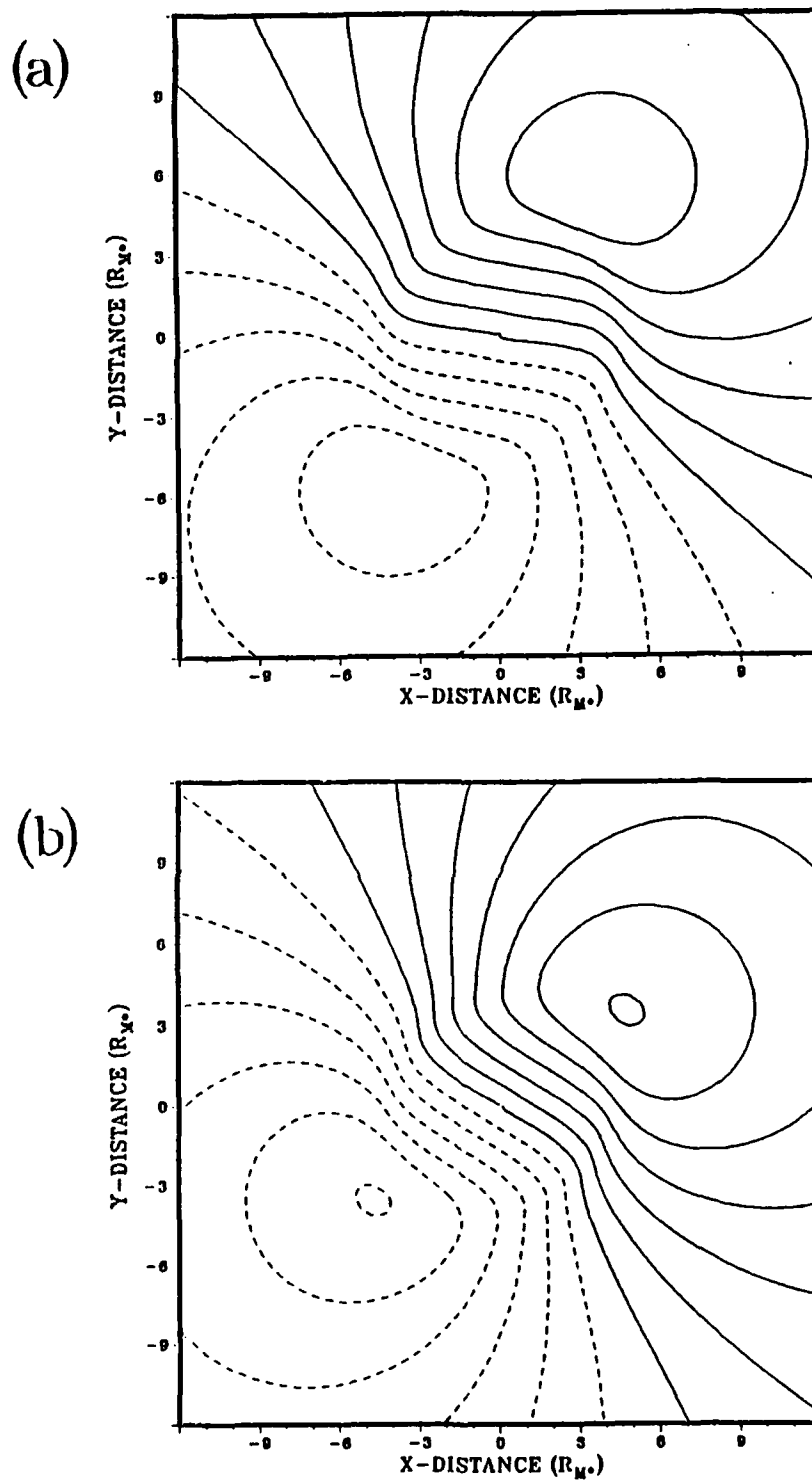
Fig. 4.26 Model-predicted wavenumber one streamfunction fields as in Fig. 4.3, except for (a) Case 1 and (b) Case 2 of Table 4.4. Contour interval is $2 \times 10^5 m^2/s$.

103

the individual pieces of the problem. The two key aspects of this piecewise-analytic modeling approach are to:

- divide the model domain relative to a transition radius within which is a Self-advection Region where mutual advections by the symmetric TC and the asymmetric interaction flow are important, and outside of which is a Dispersion Region where such advections are considered unimportant; and

- approximate the symmetric TC windfield by a piecewise-analytic modified Rankine profile that closely matches the analytic TC wind profile, except near the radius of maximum winds, and closely matches the analytic vorticity gradient in the Self-advection region near the transition radius.

This theoretical model is distinguished from previous efforts by the capabilities to:

- accurately predict both the zonal and meridional components of TC propagation by integrating linear and nonlinear mechanisms into a single self-advection process;

- accurately predict the wavenumber one gyre structure responsible for TC propagation based on either a knowledge of the propagation velocity, or determining the propagation from the model dynamics via a closure scheme;

- include the influence of changes in the symmetric wind of the TC;

- include the first-order effects of large-scale relative vorticity gradients of arbitrary magnitude and direction; and

- include the first-order effects of moderate values of uniform relative vorticity of the large-scale environment.

The close agreement between the TC propagation velocities predicted by this model and the equivalent numerical solutions verifies that the piecewise-analytic construction technique is dynamically sound. The propagation vector errors from this model have small, well-defined biases that depend on the two adjustable parameters of the model in a predictable and dynamically reasonable manner. This property, combined with the capability of the model to predict TC propagation and gyre structure for many realistic combinations of TC structure and environmental windfields, suggests that this model has significant potential for use as either: i) an initialization scheme for barotropic numerical forecast models such as SANBAR; ii) or as part of a "propagation + advection" track prediction aid. A demonstration of the potential usefulness of this model as an initialization tool is provided in Chapter V.

The success of this theoretical model in reproducing the numerical results of CW and FE provides strong evidence that nonlinear self-advection, rather than linear propagation, is the barotropic mechanism that contributes to the observed propagation of TC's. It is important to emphasize that the individual effects of β, environmental shear and environmental vorticity gradients are integrated within this self-advection model,

since those processes together determine the phase and amplitude of a wavenumber one interaction flowfield that advects the TC relative to the large-scale environment. By providing a unified theory for barotropic TC propagation, this model represents an important step toward the development of a general theory of TC motion. For the sake of brevity and to emphasize the unifying aspect of self-advection theory, this model will hereafter be referred to as the Barotropic Self-advection Model (BSAM).

V. BAROTROPIC SELF-ADVECTION MODEL APPLICATION

In this chapter, the usefulness and versatility of the BSAM will be demonstrated in three important areas. First, the issue of how accurately the outer wind strength must be measured to adequately account for propagation of TC's will be addressed by using tangential wind profiles based on composited data as input. An alternate approach of using the BSAM to predict an "effective" outer wind strength based on past TC propagation will also be outlined. Second, a quantitative assessment of the extent to which the asymmetric interaction flow will be accounted for in steering flow calculations will be made based on the wavenumber gyre structure predicted by the BSAM for the composite data. Suggestions on how to isolate the environment and interaction flow components will also be included. Finally, the feasibility of using the BSAM to initialize barotropic numerical forecast models will be demonstrated.

A. BSAM PREDICTIONS USING COMPOSITE DATA

1. Preliminary analysis

In Chapter IV, the BSAM propagation predictions were based on piecewise-analytic TC wind profiles that closely approximated the exponential wind profile (4.22) used in recent numerical studies (CW and FE). A similar exponential profile was also used by DeMaria (1985; DM). Exponential TC wind profiles were used in the BSAM to verify the accuracy of the theoretical predictions relative to equivalent numerical solutions. In light of the importance of TC structure on barotropic propagation, it is important to examine how well exponential profiles approximate TC winds, and whether some other functional form might be better for propagation-prediction purposes.

As shown in Fig. 5.1a, FE selected a "basic vortex" profile to have a radius of 15 m s winds at 300 km to agree with typical composite observations of TC surface tangential winds, such as those given by Merrill (1984) for large Atlantic hurricanes. For comparison, a "composite pressure-averaged typhoon" was calculated by taking a 950-150 mb pressure-weighted average of the western North Pacific composite TC tangential wind data of Frank (1977; his Fig. 9). The basic vortex has greater intensity and less outer wind strength than typical typhoons or large hurricanes, as represented by either the surface or the pressure-averaged tangential winds (Fig. 5.1a). The composite pressure-averaged wind profile for NW Pacific typhoons is significantly weaker at all radii than the composite surface wind profile for large Atlantic hurricanes because
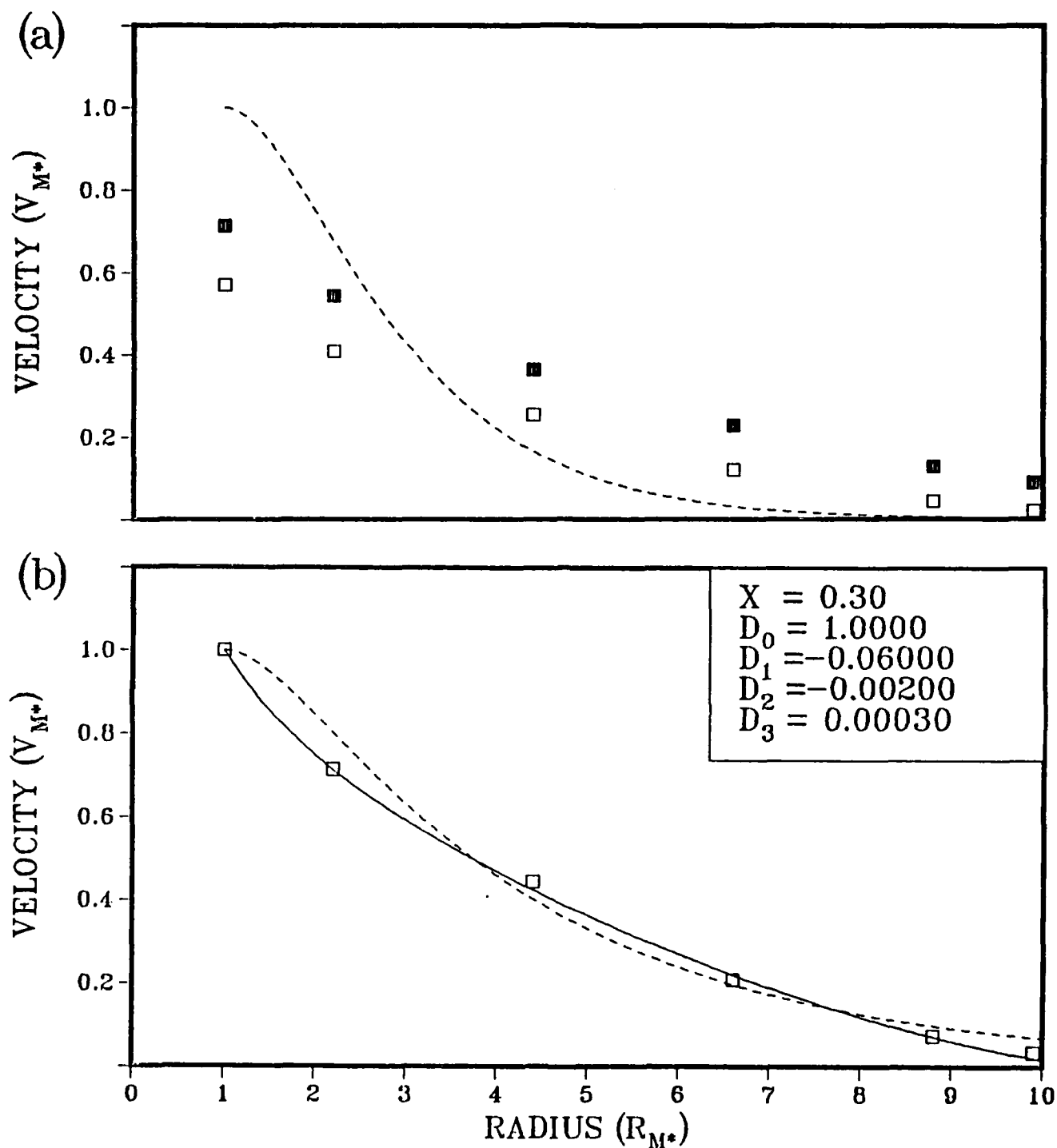
Fig. 5.1 (a) Radial profiles of Fiorino and Elsberry's "basic vortex" (dashed), the composite surface tangential winds of large Atlantic hurricanes (solid squares; Merrill 1984) and the tangential winds of the composite pressure-averaged typhoon (open squares; Frank 1977). Here $V'_{M^*} = 35$ m/s and $R_{M^*} = 100$ km. (b) Analytic approximations to the radial profile of the composite pressure-averaged typhoon (open squares) as defined by (4.22) with b = 0.6 (dashed) and (5.1) (solid; parameters in inset). Here $V'_{M^*} = 20$ m/s.

107

the tangential wind components decrease with elevation in TC's. Using surface wind profiles to initialize barotropic models may cause an overestimation of TC propagation associated with barotropic processes. The composite pressure-averaged typhoon wind profile will be used here.

Both FE and DM adjusted the maximum wind scale V_M and the b parameter in (4.22) to better fit the larger and weaker average typhoon/hurricane. Although the exponential profile can be adjusted to approximate the wind profile of the composite pressure-averaged typhoon (Fig. 5.1b), the exponential profile does not represent the curvature (and thus the vorticity gradient) of the composite profile nearly as well as the analytic function

$$v_S(r) = D_0 r^{-X} + D_1(r-1) + D_2(r-1)^2 + D_3(r-1)^3, \qquad (5.1)$$

which is a modified Rankine profile with a three-term Taylor series. Thus, (5.1) will be used as an analytic representation for composite TC tangential windfields below.

2. Propagation speed versus composite TC strength

By adjusting the curvature of the piecewise-analytic wind profile via the parameter X_1 in (4.6), the outer wind strength of the composite pressure-averaged typhoon may be underestimated, closely approximated and overestimated in the 300-800 km annulus (Figs. 5.2-5.4 respectively), even though the inner wind speeds remain essentially unchanged. In each case, the interface radius R_1 is located at 300 km as in FE so that the same strength change methodology is used. An additional parameter C_3 is present (see insets) because the functional form of v_S in the Dispersion Region has been modified to

$$v_S(r) = A_3 r^{-4} + B_3 r^{-5} + C_3 r^{-6}, \qquad (5.2)$$

to require that $\partial \zeta_S / \partial r$ be continuous at the transition radius. Although such a change adds two additional terms to (4.17b), it has a negligible influence on the BSAM-predicted propagation, and serves only to avoid overly large jumps in the piecewise-analytic vorticity gradient at R_T. The magnitude of the analytic vorticity gradient at R_T is about four times smaller for the composite profile (Fig. 5.2b) than for the exponential profiles used earlier (e.g., Fig. 4.2b). Also, the change of vorticity gradient sign occurs well into the Dispersion Region for the composite data due to the significantly greater outer wind strength. The vorticity gradient of the piecewise-analytic profile results in some underestimation of the analytic vorticity gradient at R_T. However, it is not certain whether
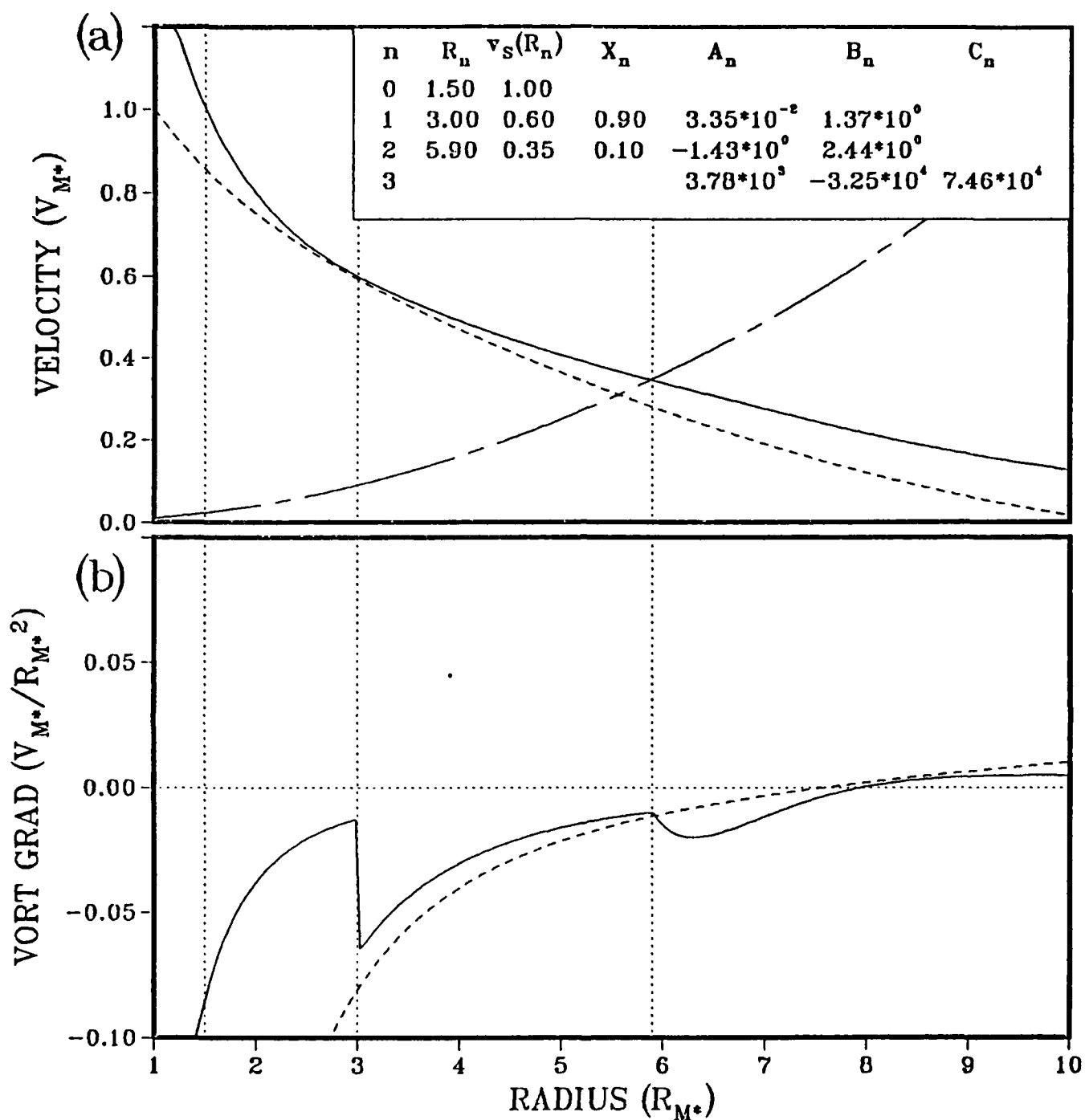
Fig. 5.2 (a) Radial wind profiles of the composite pressure-averaged typhoon (dashed) as approximated by (5.1) in Fig. 5.1b and a piecewise-analytic profile (parameters in inset) that overestimates outer wind strength. (b) Piecewise-analytic and analytic vorticity gradient profiles corresponding to the winds in (a). In both cases, $V_{M*} = 20$ m/s and $R_{M*} = 100$ km.

n	R_n	$v_S(R_n)$	X_n	A_n	B_n	C_n
0	1.50	1.00				
1	3.00	0.60	0.60	$-5.47*10^{-2}$	$1.36*10^{0}$	
2	5.50	0.31	0.10	$-1.91*10^{0}$	$3.05*10^{0}$	
3				$1.76*10^{3}$	$-1.26*10^{4}$	$2.44*10^{4}$
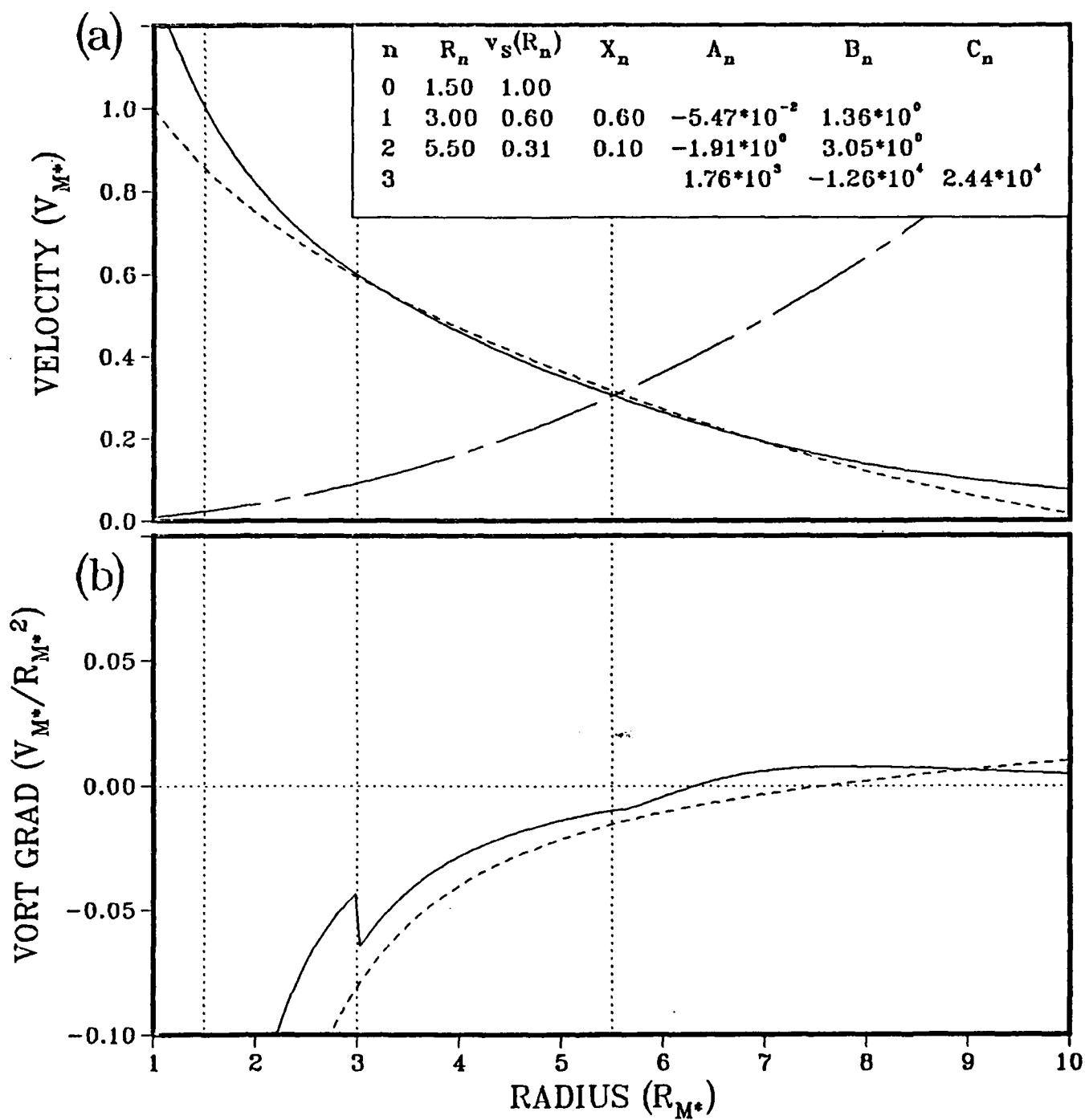
Fig. 5.3 As in Fig. 5.2, except for a piecewise-analytic wind profile that closely approximates the outer wind strength of the composite pressure-averaged typhoon in the 300 to 800 km radius "critical annulus."

110

n	R_n	$v_S(R_n)$	X_n	A_n	B_n	C_n
0	1.50	1.00				
1	3.00	0.60	0.10	$-2.31*10^0$	$3.54*10^0$	
2	5.30	0.27	0.10	$-2.31*10^0$	$3.54*10^0$	
3				$7.59*10^2$	$-3.57*10^3$	$3.67*10^3$
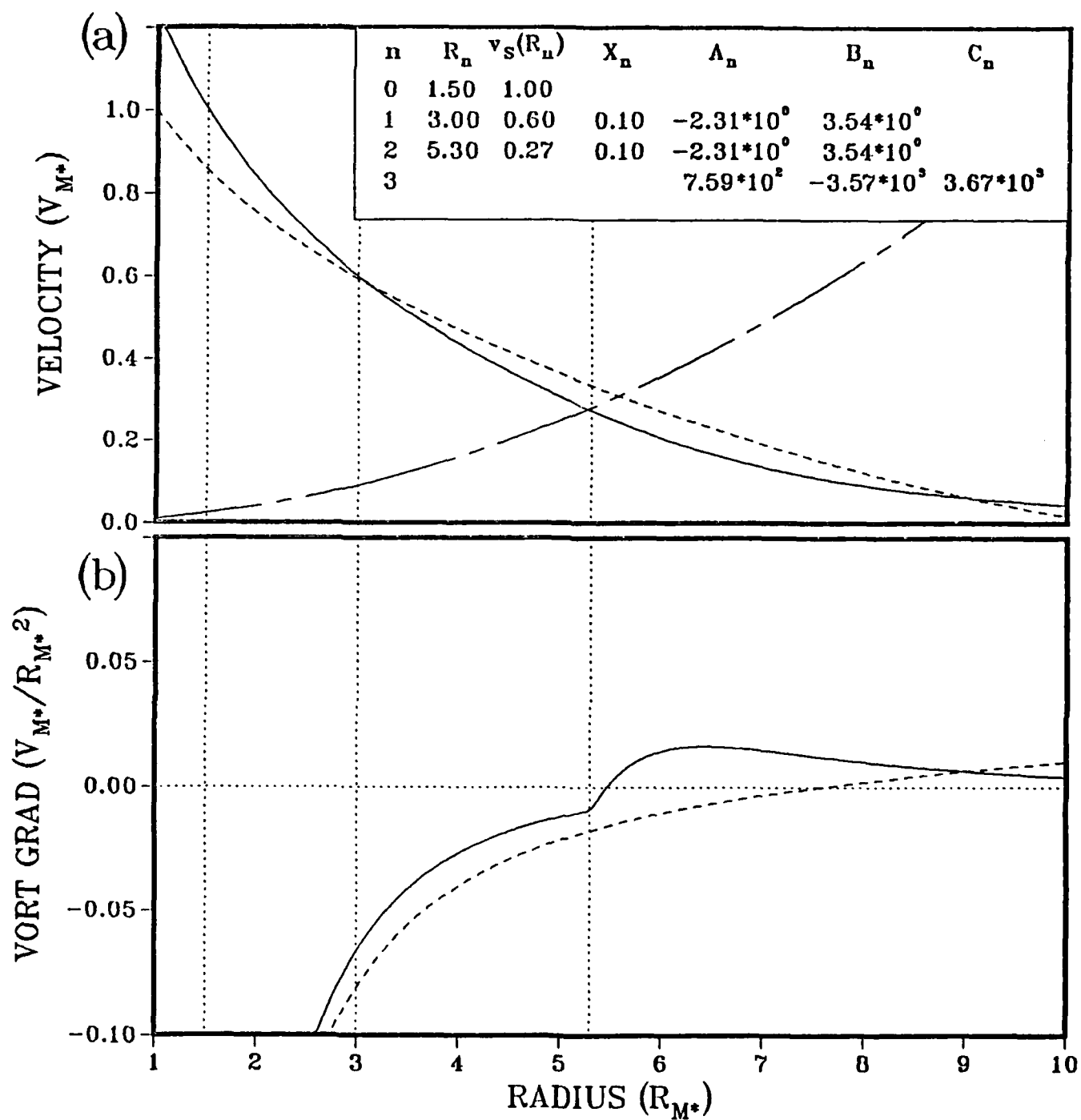
Fig. 5.4 As in Fig. 5.2, except for a piecewise-analytic wind profile that underestimates the outer wind strength of the composite pressure-averaged typhoon.

111

this will introduce a speed bias into BSAM propagation predictions because the coarse radial resolution and limited accuracy of the composite data allows for some subjectivity in selecting the curvature and fit of (5.1).

Table 5.1   TC propagation velocities (columns 5,6) predicted by the BSAM for piecewise-analytic wind profiles (see Figs. 5.2a-5.4a) that underestimate, approximate and overestimate the outer wind strength of the composite pressure-averaged typhoon (Cases 1-3 respectively). In each case, a quiescent environment has been assumed. The wind speed at the transition radius R_T (column 3) and at 550 km (column 4) are also shown.

Case	X_t	$v_{S^*}(R_{T^*})$ (m s)	$v_{S^*}(550\,\text{km})$ (m/s)	$\hat{C}$ (m/s)	α (deg)
1	0.1	5.4	5.0	1.8	137
2	0.6	6.2	6.2	2.2	132
3	0.9	7.0	7.4	2.8	127

The propagation speeds and directions predicted by the BSAM (Table 5.1) increase with increased TC outer wind strength, which is in general agreement with the results of Chapter IV and previous studies. Quasi-linear relationships exist between the propagation speed (column 5) and the wind speed at the transition radius (column 3), and the wind speed at 550 km (column 4). The first relationship has more relevance to the dynamics of the BSAM since $v_{S^*}(R_{T^*})$ is a rough measure of the amount the linear asymmetric forcing generated in the Dispersion Region, which acts to strengthen the wavenumber gyres and thus increase the propagation speed. The second relationship is also dynamically relevant because 550 km would be the center of FE's "critical annulus" between 300 and 800 km. The 1 m's propagation speed increase for a 2.4 m's increase in TC tangential winds at 550 km represents a potential for about 85 km of forecast error in 24 h. This result suggests that TC outer wind strength must be measured to within ± 1 m s in order for numerical models to be initialized with sufficient accuracy to avoid

significant forecast errors due to misrepresentation of TC strength. Important related questions are: i) do numerical model heating and dissipative parameterizations tend to maintain the tangential wind profile to this accuracy throughout the forecast integration; and ii) are changes in TC strength that occur during a forecast period accurately reproduced by numerical forecast models?

This sensitivity of TC propagation on outer wind strength poses a significant challenge for present observing system technologies. However, the method just used to demonstrate the wind-strength/propagation-speed relationship offers a potential alternate approach to determine an "effective" TC strength. In Table 5.1, the independent adjustment of a single parameter X_1 (R_T varies as a result) causes related changes to TC outer wind strength and propagation speed. It is therefore possible, in principle, to seek a value of X_1 such that the propagation speed predicted by the BSAM matches the observed value at the initial time. The associated wavenumber one gyre structure predicted by the BSAM could then be used to initialize a barotropic forecast model like SANBAR, or provide guidance in selecting an appropriate bogus vortex for baroclinic forecast models.

Implicit in such a scheme to predict TC strength are the requirements that: i) the large-scale environment is known sufficiently well to provide β_{eff}, ϕ and Z_F for the BSAM; ii) the track of the TC is resolved well enough to compute propagation relative to the barotropic steering of the environment; and iii) an estimate of TC speed at about 300 km is available. Since it is likely that many combinations of inner intensity and outer wind strength can give similar propagation velocities, such a scheme might not need to reproduce the outer wind structure of the TC, but only an inner-intensity/outer-wind-strength combination (i.e., an "effective" TC strength) that will produce the correct propagation. In addition, possible baroclinic contributions to TC propagation might also be parameterized to some extent by such an approach.

B. INTERPRETATION OF COMPOSITE TC PROPAGATION VECTORS

In Chapter I, comparison of observations of TC propagation with numerically derived depictions of β-induced wavenumber one gyre structure (FE) led to the preliminary conclusion that the uniform flow region of the gyres would not be accounted for in steering flows calculated over an annulus of 5-7° lat. radius. However, the wavenumber one gyres for the composite pressure-averaged typhoon due to β-forcing only (Fig. 5.5) are somewhat larger than the gyres associated with the basic vortex profile of FE (Fig. 4.4). The well resolved gyre structure provided by the BSAM will be used to calculate
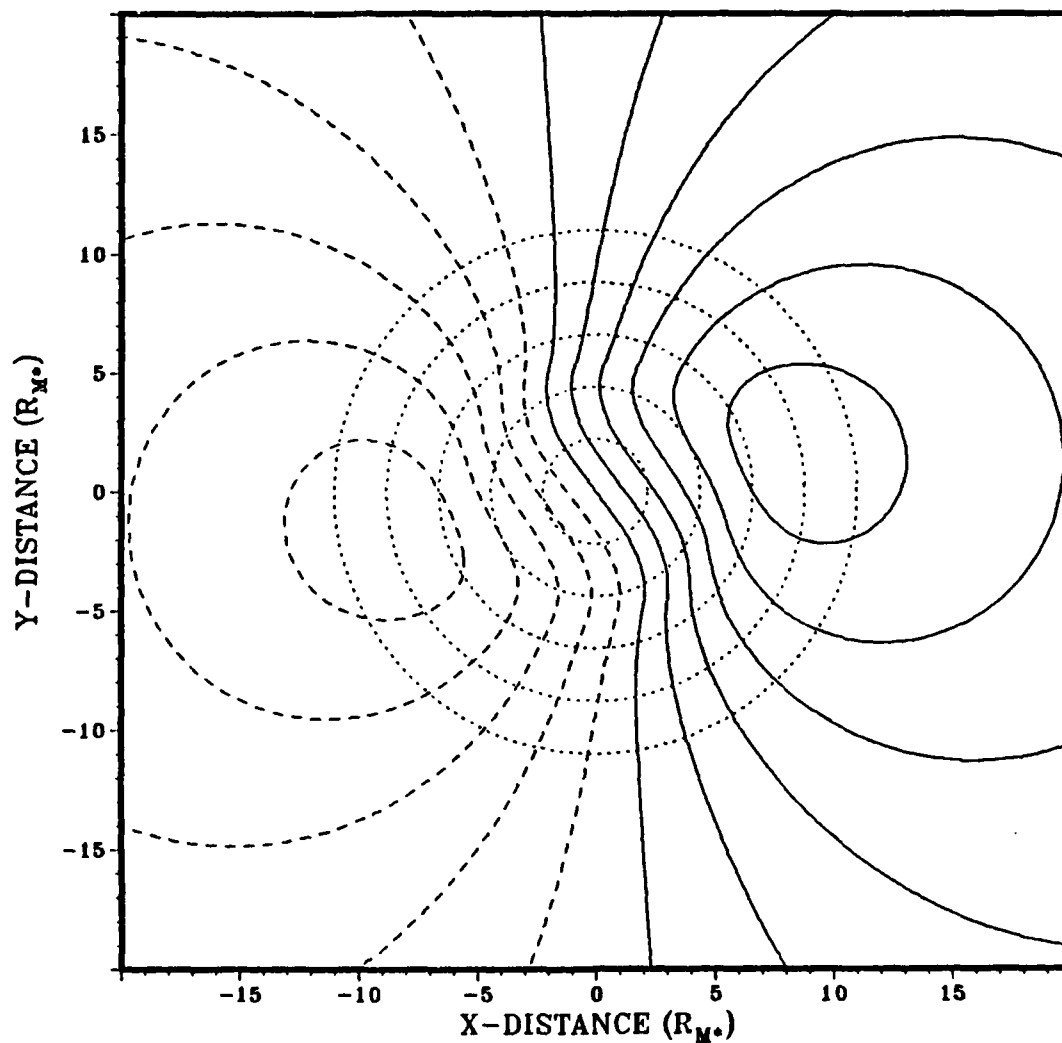
Fig. 5.5 Wavenumber one gyre streamfunction (dashed, negative) associated with Table 5.1 Case 2. Contour interval is $2.0 \times 10^5 m^2/s$. Dotted circles have radii of 2°, 4°, 6°, 8° and 10° lat. The middle circle corresponds to the center of the 5°-7° lat. radius annulus typically used to compute steering from composite data (*e.g.*, Chan and Gray 1982; Holland 1984). The parameter $R_{M^*} = 100$ km.

the extent to which TC self-advection is included in such steering flow calculations or is manifested as propagation.

By averaging the velocities around various circles centered on the BSAM-predicted gyres (Fig. 5.5; dotted lines), a set of velocity vectors representing interaction flow contributions to environmental steering may be obtained (Fig. 5.6a). Subtracting such vectors from the BSAM-predicted propagation velocity for the composite pressure-averaged typhoon (Table 5.1; columns 5,6) gives a set of vectors that represent the propagation of the storm relative to the steering computed at a particular radius (Fig. 5.6b). For composite steering computed at a 2° lat. radius, most of the interaction flow is accounted for in the steering, whereas the propagation vector is about 0.4 m/s to the west. In contrast, at the 6° lat. radius where steering is typically computed, all of the westward component and about one quarter of the northward component are manifested as propagation. This result is consistent with the structure of the wavenumber one gyre uniform flow region in Fig. 5.5, which is oriented essentially north-south at 6° lat. radius, but still has a velocity nearly as large as the innermost portion of the flow. This result may then explain why TC propagation computed from composite data over a 5-7° annulus tends to have a predominantly westward orientation (Fig. 1.1). Although the analysis here has used gyres associated with only the influence of planetary vorticity, the results would also apply to the more realistic environmental situations of Chapter IV Section D.3, if appropriate phase shifting of the vector patterns is taken into account.

As discussed in Chapter III, the angular windshear in the symmetric TC produces a down-shear tilting of the inner portion of the wavenumber one gyre that barotropically stabilizes the TC to asymmetric forcing. It is this down-shear tilt that produces the characteristic cyclonic rotation and increasing magnitude of TC propagation relative to steering flows computed at increasingly larger radii (Fig. 5.6b). This propagation vector pattern was evident in early compositing studies (George and Gray 1976; their Figs. 12 and 13), and is a persistent feature of the recent compositing results based on much larger data sets presented by W. Gray at a recent Office of Naval Research Workshop on Tropical Cyclone Motion (Elsberry 1989). Such vector patterns may be interpreted as evidence that observed TC propagation is a manifestation of self-advection by wavenumber one gyres produced by asymmetric forcing. Although baroclinic processes may also contribute to the total wavenumber one gyre pattern, the general agreement of observed propagation (Figs. 1.1) with the predictions of barotropic theory (Table 4.4) suggests that barotropic processes are the dominant influence.

115
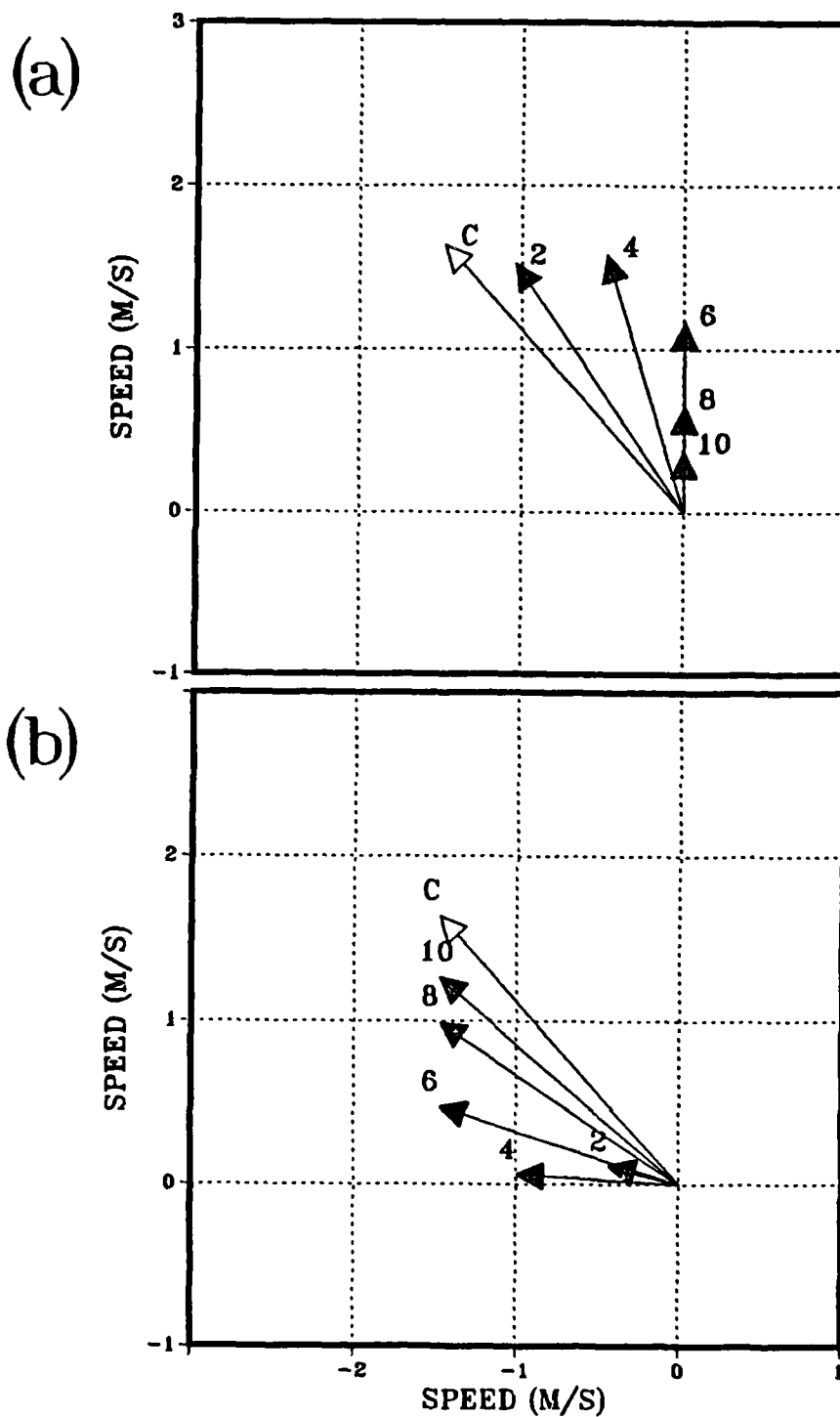
Fig. 5.6 (a) BSAM-predicted propagation (C) for the composite pressure-averaged typhoon and contributions to environmental steering by the associated BSAM-generated wavenumber one gyre flow evaluated around the 2,4,6,8 and 10° lat. radius circles of Fig. 5.5. (b) Differences between composite pressure-averaged typhoon propagation (C) and the wavenumber one gyre contributions to steering of (a).

For the BSAM to be used as a numerical model initialization tool or as part of a propagation + advection forecasting aid, the interaction flow must be effectively excluded from the environmental windfield. Although filtering is often used in an attempt to remove the influence of the TC from the large-scale environment, alternate methods to compute steering that better exclude the uniform flow region of the gyres should also be investigated. For example, the steering might be computed along circles as in Fig. 5.5, but including only the 90° arcs centered on a line normal to the direction of the large-scale absolute vorticity gradient (Fig. 5.7). Using this approach (Fig. 5.8a), the interaction flow contribution to the 6° lat. radius steering accounts for only half the northward component of propagation, and the contribution to the 8° lat. radius steering is essentially zero. As a result, nearly all of the interaction flow influence is manifested as propagation relative to steering computed at 8° lat. radius or larger (Fig. 5.8b). Thus, it may be desirable to depart from traditional steering computation methods to better separate the large-scale environment from the influence of the TC.

C. NUMERICAL MODEL INITIALIZATION

The wavenumber one gyre structures provided by the BSAM (based on either an external specification or an internal prediction of TC propagation) should be ideal for initializing a nondivergent, barotropic (NDBT) numerical model so that quasi-steady motion occurs immediately. Comparisons with the NDBT numerical model of CW will be used to provide a preliminary verification of this assertion. The model uses a β-plane approximation, a 4000x4000 km channel domain with an east-west cyclic boundary condition and a resolution of 20 km.

1. Quiescent environment predictions

Using the symmetric, exponential TC wind profile of Table 4.2 Case 2, the CW model predicts a nearly constant β-induced propagation direction of about 330° during the first 48 h (Fig. 5.9). In contrast, the propagation speed increases from zero initially to about 2.65 m s at 48 h. During this period, the asymmetric gyres develop, and then the propagation speed becomes almost constant (2.8 m s) after the gyres are established. In a real storm, these gyres are presumably present continually, and change only in response to variations in TC structure or environmmental forcing. The "forecast error" associated with the transient acceleration period evident in Fig. 5.9 may be estimated by comparing the 0-48 h track with a 48 h displacement between say 36 h and 84 h during which the propagation speed is quasi-steady. The comparison is facilitated by
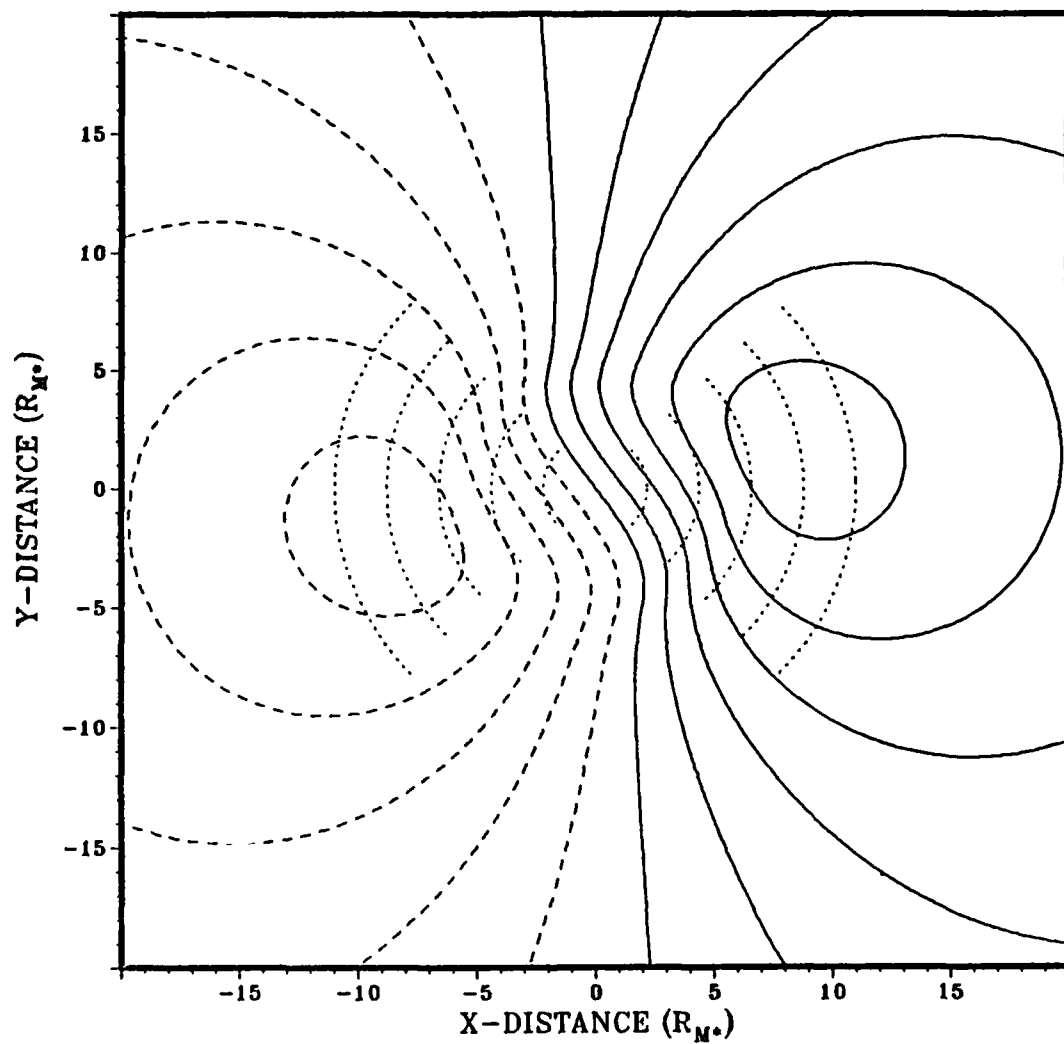
Fig. 5.7 As in Fig. 5.5, except for including in steering flow computation only the winds in the 90° arcs to the right and left of the planetary vorticity gradient.
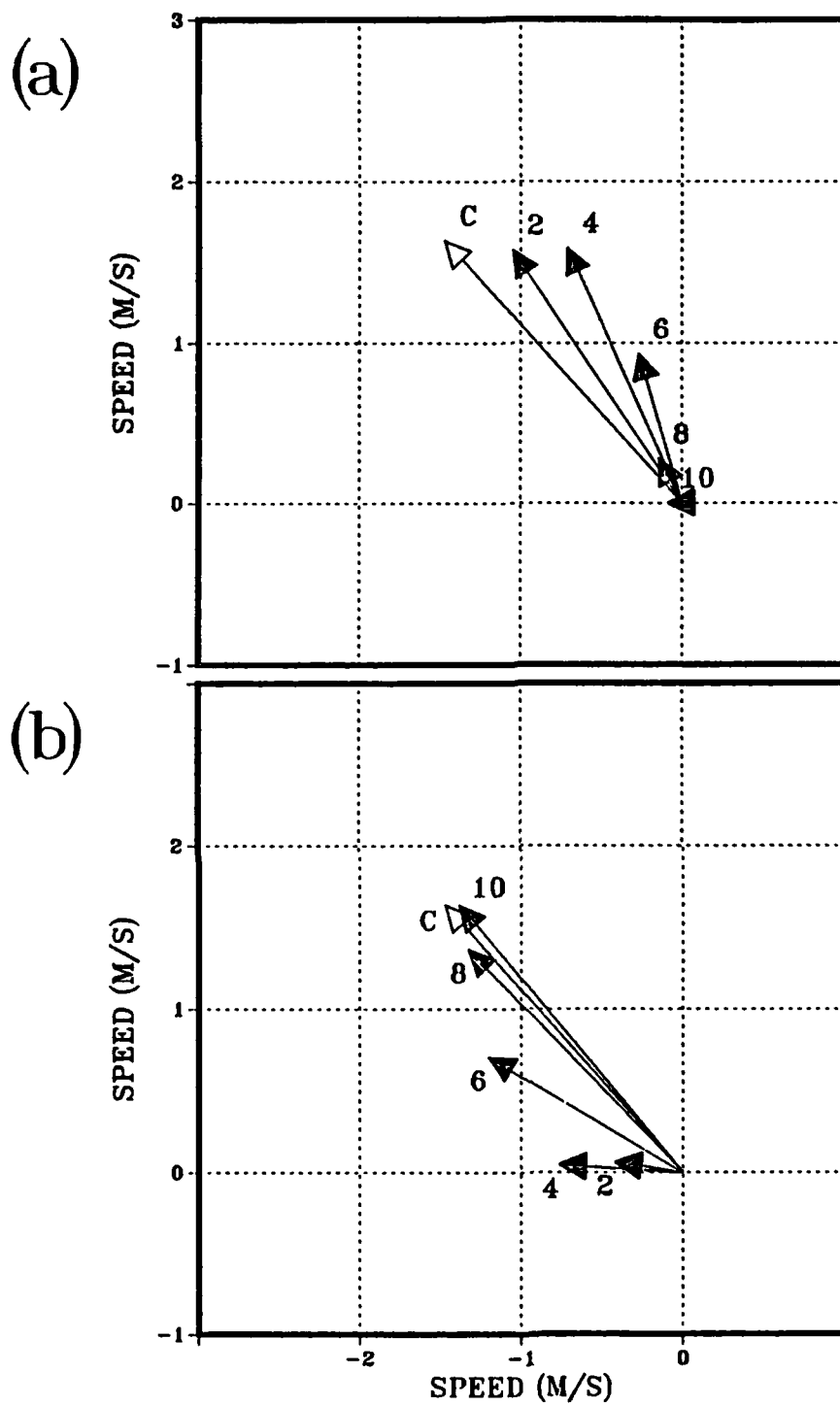
Fig. 5.8 As in Fig. 5.6, except for vectors calculated based on the arcs shown in Fig. 5.7.

119
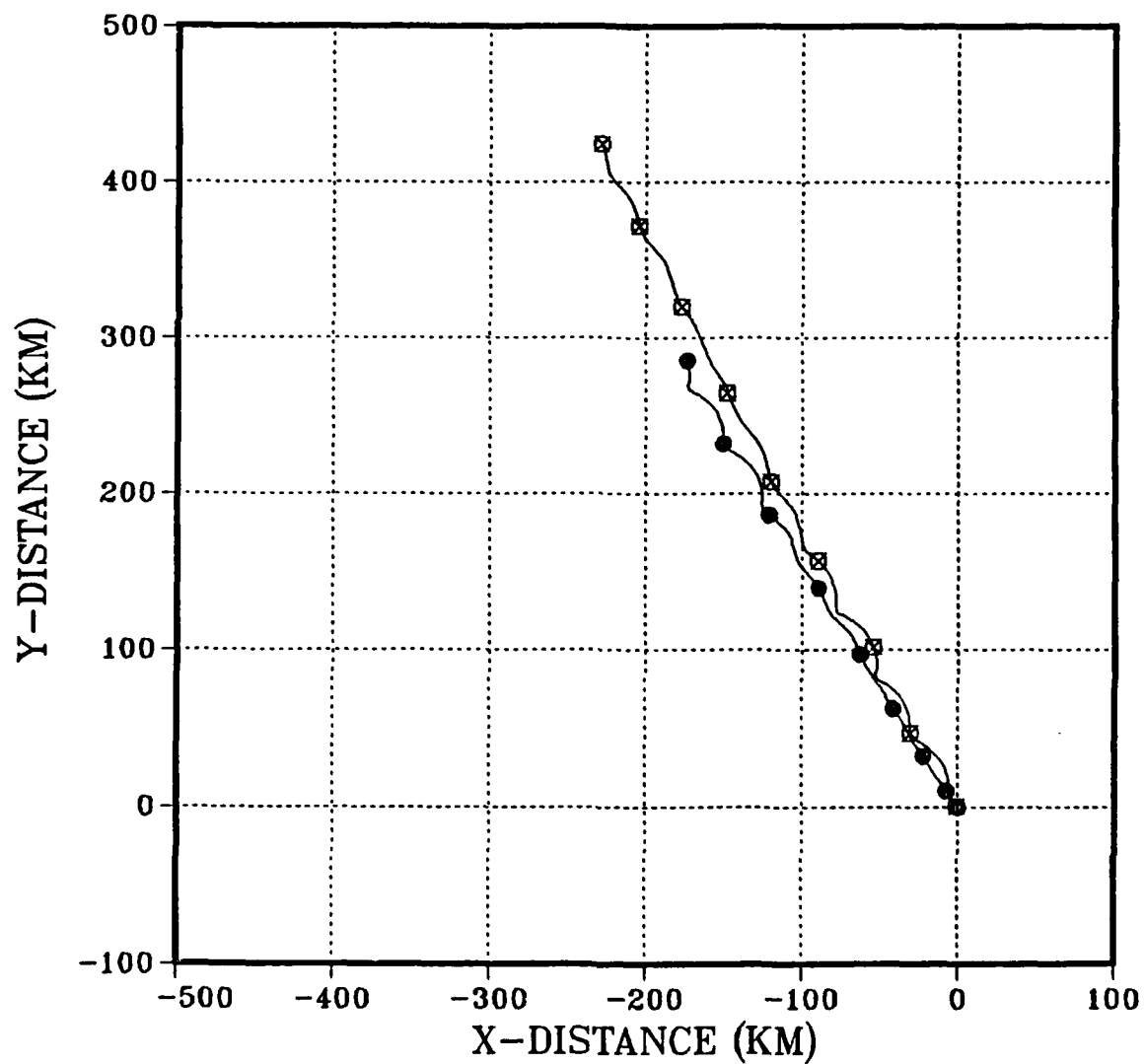
Fig. 5.9 β-induced propagation tracks and 6-hour positions predicted by the numerical model of Chan and Williams (1987) for an initial TC wind profile corresponding to Table 4.2 Case 2 from 0-48 h (solid circles), and for the period 36-84 h (crossed circles) except translated so that the 36 h position corresponds to the initial position of the TC.

120

translating the 36-84 h track so that the 36 h position of the TC corresponds to the initial position.

The along-track error of about 150 km suggested by this approach may be an underestimation since the TC has slowed to about 2.6 m/s by 84 h due to a weakening of outer wind strength as the TC is displaced northward on a β-plane (cf., FE). The much smaller cross-track error is caused by the slightly more northward track of the TC from 36-84 h as compared to 0-48 h. Since this error is small, and may be associated with different TC strength during the two 48 h periods or boundary influences, it will be ignored.

The numerical model is now modified to include the wavenumber one gyre structure generated by the BSAM given the propagation velocity of 2.8 m/s at 330° ($\alpha = 120°$) reported by CW, or the BSAM-predicted propagation velocity (Table 4.2, Case 2), as shown in Figs. 5.10a and 5.10b respectively. In both cases, essentially steady propagation of the model TC occurs immediately (Fig. 5.11). The propagation tracks for the two asymmetric initializations agree remarkably well, despite the 12° difference between the initial direction of propagation predicted by the BSAM and the value observed by CW. This indicates that the numerical model has rapidly adjusted for differences between the analytically-predicted gyres and those that would be generated from an initially symmetric TC wind profile (e.g., Fig. 4.4.). This is consistent with the results of Chapter III regarding short adjustment times near the radius of maximum winds, since only the central uniform flow region of the BSAM-generated gyres is altered by modest changes in propagation direction. Thus, the more important aspect of the initialization with the BSAM-generated gyres included is that the proper propagation speed is established immediately.

Using the 36-84 h track in Fig. 5.11 as a benchmark, the two initializations of the numerical model with β-induced gyre structures produce an along-track forecast error of about 60 km. As indicated above, this error is likely an overestimation, because the 36-84 h track includes an anomalously slow portion around 84 h. Thus, the along-track error at 48 h has been reduced from greater than 150 km to a value under 60 km. Part of the apparent cross-track error of 38 km relative to the translated 84 h position of the TC is an artifact of the more northward track of the TC from 36 h to 84 h, as mentioned above. Comparing the 0-48 h track in Fig. 5.9 with the 0-48 h tracks in Fig. 5.11 indicates that the cross-track error is actually about 20 km.
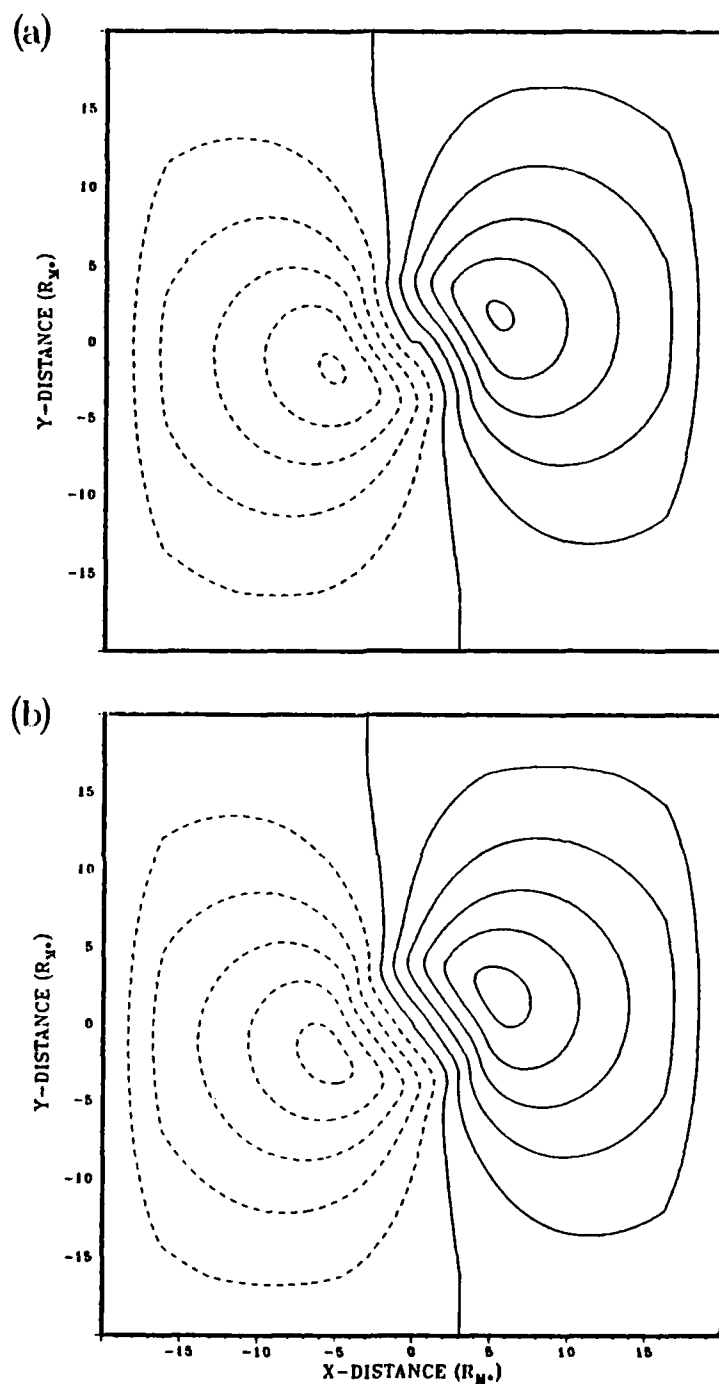
Fig. 5.10 Wavenumber one gyre streamfunction patterns generated by the BSAM for the symmetric TC of Table 4.2 Case 2 for (a) Chan and Williams propagation velocity of 2.8 m/s at 330° ($\alpha = 120°$), and (b) a BSAM-predicted propagation velocity of 2.65 m/s at $\alpha = 132°$. Areal extent of the figures corresponds to the domain of the numerical model, and the streamfunctions have been linearly adjusted to zero within 20 gridpoints of the domain boundaries.
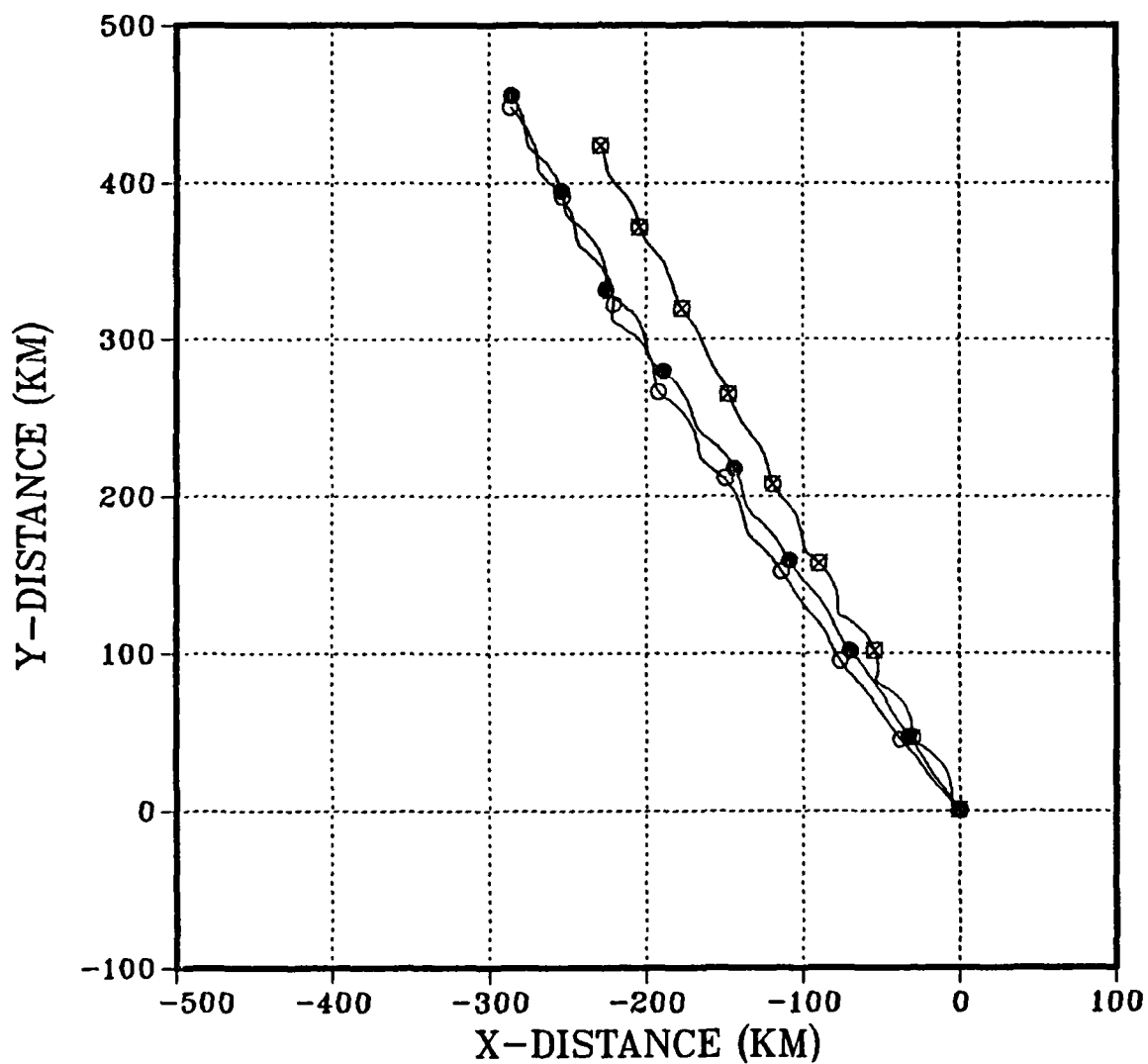
122

Fig. 5.11 The β-induced propagation tracks and 6-hour positions predicted by the numerical model initialized with the symmetric TC as in Fig. 5.9, except including the gyre structures of Fig. 5.10a (solid circles) and Fig. 5.10b (open circles). For comparison, the translated 36-84 h track (crossed circles) from Fig. 5.9 is also shown.

2. Results in a linearly-sheared environmental current

As shown in Table 4.3, the BSAM predicts significant changes in TC propagation speed and direction for different values of uniform environmental vorticity. Initialization tests may also be made with the CW numerical model by including a linearly-sheared zonal current defined by

$$u_{E*} = -Z_{E*} y_* , \tag{5.3}$$

which has zero velocity at the initial position of the TC. The numerical model is then integrated for 48 h using the symmetric TC vortex of Table 4.2 Case 2 with and without the BSAM-predicted gyres for Table 4.3 Cases 1 and 2. Only BSAM-predicted propagation velocities can be used here since numerical predictions of TC propagation relative to a sheared zonal current are not presently available, although work is proceeding in this area (Williams 1989; personal communication).

Comparison of the 0-48 h tracks of the initially symmetric and BSAM-initialized TC's in the uniformly anticyclonic (Fig. 5.12) and cyclonic (Fig. 5.13) zonal currents reveals a peculiar aspect that warrants detailed analysis. In the anticyclonic shear case, the distance between the 24 h and 30 h positions of the BSAM-initialized TC is equivalent to a speed of 3.3 m/s. Since the TC is moving essentially due north during this period, such a movement can only be due to a β-induced propagation that is substantially faster than the 2.3 m/s initially provided by the BSAM-generated gyre. This result may be due to the BSAM having a slow bias in the anticyclonic shear case. However, other evidence suggests the propagation speed increase may be associated with a nonsteady process present in the numerical model. For example, the 42 h to 48 h movement of the BSAM-initialized TC is equivalent to 3.9 m/s, which is significantly faster than the 24 h to 30 h speed computed above. In additional, the 42-48 h speed of the initially symmetric TC in Fig. 5.12 is faster (3.0 m/s) than the counterpart in a quiescent environment (Fig. 5.9), which was noted earlier to have a 42-48 h speed of 2.65 m/s. Thus, the evidence strongly suggests that the influence of uniform anticyclonic environmental shear causes a nonsteady alteration of β-induced TC propagation that cannot be accounted for by a steady-state model such as the BSAM.

A similar result is not found for the cyclonic shear case. The 42-48 h speed of 4.2 m/s for the BSAM-initialized TC in cyclonic shear (Fig. 5.13) also is substantially faster than the propagation of 3.0 m/s generated by the BSAM gyres (Table 4.3; Case 2, column 3). However, since this track is largely westward, a significant fraction of this
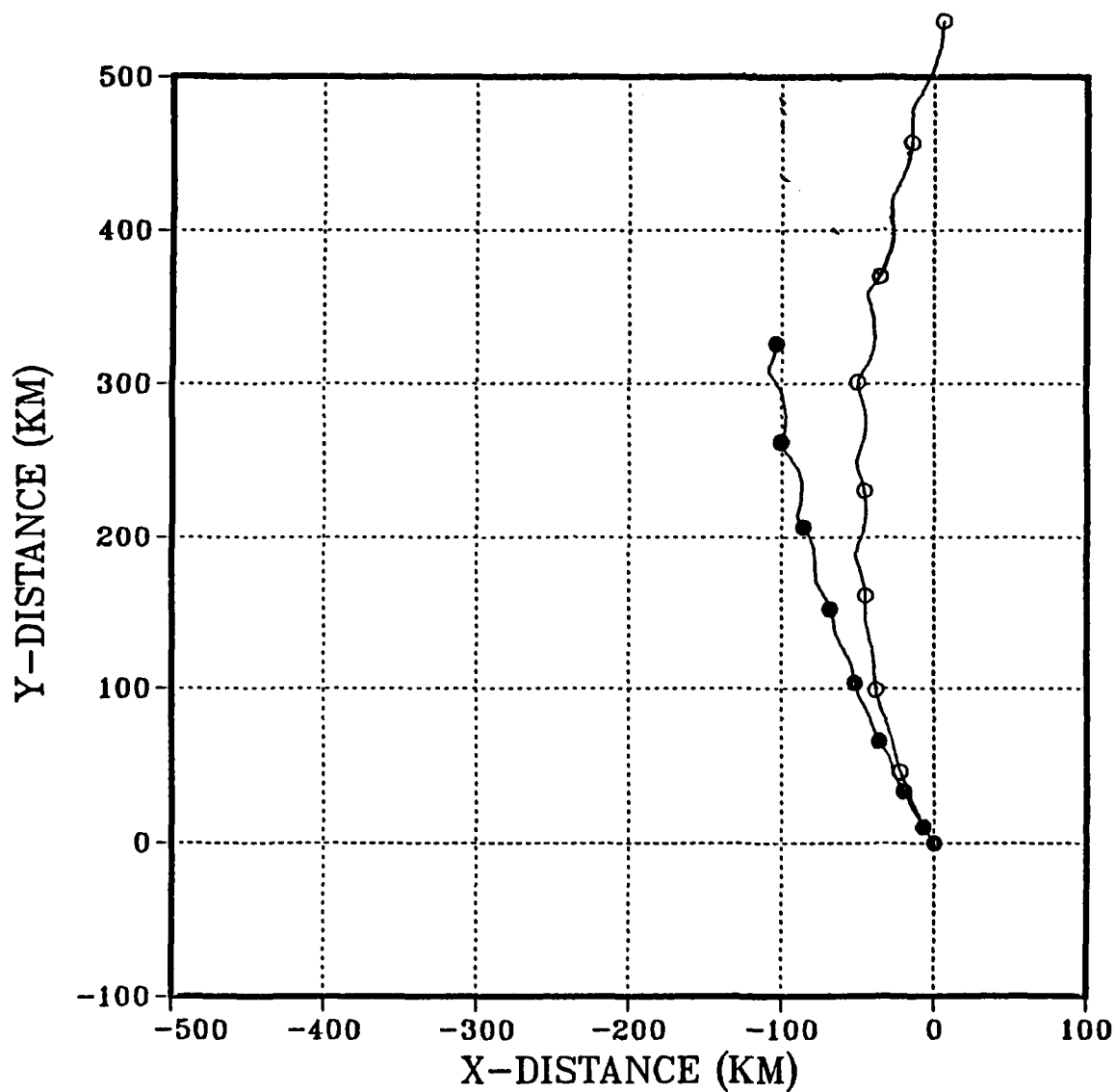
Fig. 5.12 Tracks and 6-hour positions predicted by the numerical model for β-induced TC propagation in an zonal current with linear anticyclonic shear of $Z_\xi = -5.0 \times 10^{-6}s^{-1}$ using the symmetric initial TC wind profile of Fig. 5.9 with (open circles) and without (solid circles) BSAM-generated wavenumber one gyres.

125
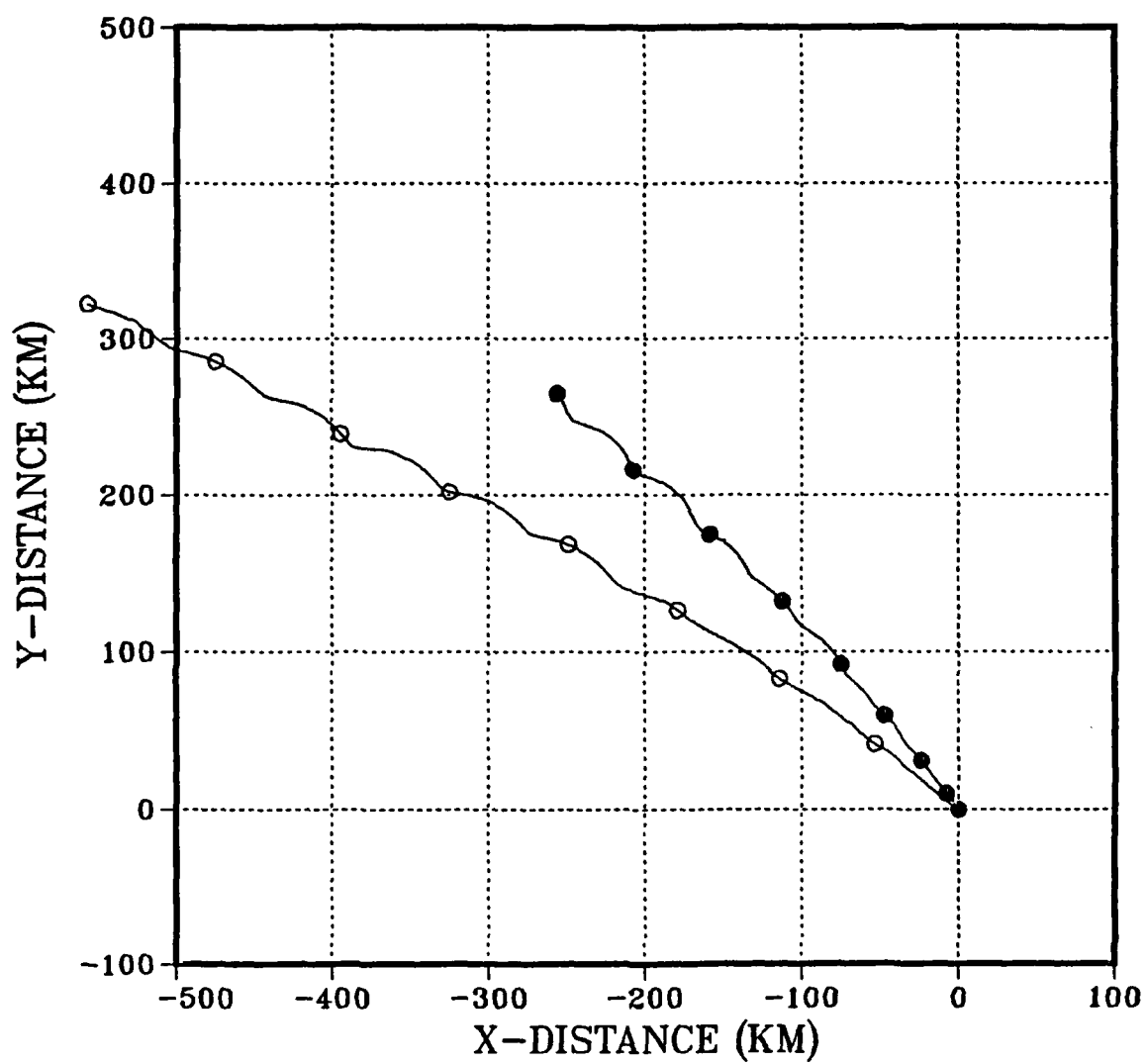
Fig. 5.13 As in Fig. 5.12, except for cyclonic shear of $Z_{E^*} = 5.0 \times 10^{-6} s^{-1}$.

total motion is due to the 1.5 m/s westward speed of the environmental current at that location. Subtracting the environmental velocity vector results in a β-induced propagation velocity of 2.9 m/s in a direction $\alpha \approx 144°$. The difference between this result and initial propagation specified in Table 4.3 Case 2 is insignificant compared to the large change in propagation velocity that occurs in the anticyclonic case above.

The solutions of Chan and Williams (1989) for β-induced TC propagation in a linearly-sheared zonal current also contain anomalously fast propagation in anticyclonic shear, but no measurable changes in cyclonic shear. Thus, this unexplained behavior is not limited only to the BSAM. The increased propagation speed in anticyclonic shear is certainly not intuitively plausible, since the results of FE (if applicable) would suggest that the weakening of the outer wind strength of the TC due to a superposition of an anticyclonically sheared current should cause slower propagation. Additional numerical integrations are being performed to gain a better understanding of the dynamical or perhaps numerical basis for this behavior (personal communication, R. T. Williams 1989).

The potentially nonsteady influence of linear environmental windshear on β-induced TC propagation make a precise determination of how well the BSAM has initialized the CW numerical model difficult. However, several qualitative observations and comments can be made. It is evident in Figs. 5.12 and 5.13 that significant cross-track as well as along-track errors exist between the positions of initially symmetric and BSAM-initialized TC's when a spatially variable environment is present. As in the quiescent environment case above, the along-track differences are due to the nonzero initial speed of the BSAM-initialized TC. The cross-track differences are in part due to a slightly different starting direction for the BSAM-initialized TC, which in effect accounts for phase shifting of the wavenumber one gyres by the "past" influence of environmental shear. Additional research will be necessary to understand to what extent the present asymmetric structure of TC's reflects past environmental influences. The cross-track differences are also due to the nonzero initial propagation speed of the BSAM-initialized TC which, continually subjects the TC to different environmental winds compared to the initially symmetric TC. Thus, the tracks of the BSAM-initialized and initially symmetric TC diverge with time. The divergence is much greater in the cyclonic environment case due to the greater speed of propagation and the cyclonic rotation of the β-induced gyres such that a larger zonal motion component (propagation + environmental advection) is produced. It should also be emphasized that the 48 h along-track and cross-track differences of up to 280 km and 80 km respectively in Figs.

5.12 and 5.13 indicate that initializing a numerical model with only a symmetric TC wind profile has much more serious consequences when spatially spatially variable environmental winds are present than for a quiescent environment (Fig. 5.11).

D. SUMMARY

In this chapter, three basic but important applications of the BSAM have been demonstrated. First, the BSAM has been used with composite observations to predict the barotropic propagation due to β for a composite pressure-averaged typhoon, and to predict the change in propagation speed that might be expected for a typhoon with larger or smaller outer wind strength. The results suggest that misrepresenting the outer wind strength by about 2.5 m/s will cause a 1 m/s error in barotropic propagation, which represents a potential forecast error of 85 km in 24 h. This application also outlined a method by which the BSAM might be employed to predict an "effective" outer wind strength based on *a priori* knowledge of TC propagation.

Second, analysis of the β-induced gyre structure predicted by the BSAM for the composite pressure-averaged typhoon provided evidence that the TC propagation vectors in composite data (Fig. 1.1) are indeed manifestations of wavenumber one gyres associated with self-advection processes. An alternate method for computing environmental steering that better separates the large-scale environment from the self-advection flow was also demonstrated.

Finally, and most importantly, the potential usefulness of the BSAM as an initialization tool for barotropic numerical forecast models was demonstrated. In the case of a quiescent environment, initializing the numerical model with BSAM-predicted wavenumber one gyres reduced the along-track forecast error at 48 h from more than 150 km to less than 60 km. When a linearly-sheared zonal environmental current was included, significantly larger along-track and cross-track differences of up to 280 km and 80 km respectively were observed between the 48 h positions of an initially symmetric TC and a BSAM-initialized TC.

VI. CONCLUSION

The principal achievement of this research has been the development, testing and preliminary application of a comprehensive theoretical model for predicting tropical cyclone (TC) propagation and associated asymmetries based on the barotropic self-advection process identified in recent numerical studies. The model is comprehensive in the sense that it includes the first-order effects of all of the dynamical processes that are presently understood to be important to barotropic TC propagation: gradients of planetary and environmental vorticity, changes in TC wind structure, and environmental windshear. Since the model is based on a single self-advection principle through which individual external forcing effects collectively determine the phase and amplitude of a wavenumber one gyre flow that advects the TC, the nomenclature Barotropic Self-Advection Model (BSAM) has been adopted. Because of the dynamical complexity of barotropic TC self-advection, a rather lengthy chain of hypotheses, assumptions and approximations were employed to make the problem analytically tractable. The principal "links" in this development chain are summarized in Section A and a summary of results follows in Section B.

A. OVERVIEW OF PRINCIPAL ANALYSIS TECHNIQUES

1. Dissection of the problem and model formulation

Based on prior numerical findings that TC propagation relative to steering results from wavenumber one asymmetries induced by TC-environment interaction, the total flow field has been partitioned into three components: i) a specified large-scale environment; ii) a symmetric cyclone circulation; iii) and an unknown asymmetric interaction flow component that is presumed to be responsible for TC propagation. A transformation to a reference frame moving with the TC has been utilized, and the symmetric TC component is assumed steady in such a reference frame to further simplify the problem. By subtracting from the total problem an equation governing the large-scale environment in the absence of the TC, an equation for the evolution of the interaction flow in response to external forcing has been obtained. Thus, the partitioning and transformation process significantly simplified the problem by focusing the analysis on that portion of total flow field that is relevant to TC propagation.

The mathematical complexity associated with the polar symmetry of the problem and the extreme radial anisotropy of the symmetric TC flow variables makes it very

129

difficult to find a single solution that is analytic in the whole model domain. Thus, it has been assumed that a piecewise-analytic solution obtained using a matched-asymptotic approach will be a reasonable approximation. In the preliminary model development (Chapter II), this assumption entailed dividing the model domain relative to a "transition radius." Inside this radius is a Self-advection Region in which mutual advections by the symmetric TC and interaction flow dominate, and outside this radius is a Dispersion Region in which those advections are unimportant relative to the external asymmetric forcing. After formally showing that only wavenumber one processes can contribute significantly to TC propagation, the problem has been further simplified by retaining only the first-order contributions to wavenumber one processes in the interaction flow governing equation.

To overcome the problem of radial anisotropy noted above, the model domain has been subdivided further (Chapter IV) by assuming that the symmetric TC winds in the Self-advection Region can be reasonably represented by a set of piecewise-analytic, modified Rankine segments. A solution valid for the whole model domain then has been assembled from solutions valid in individual annular regions by imposing matching conditions on solutions at the annulae interfaces. Thus, the intractability of the full problem has been overcome by subdividing the problem sufficiently to make the individual pieces analytically tractable. The success of this systematic dissection approach to modeling TC self-advection has been demonstrated by several comparisons with complete numerical solutions and with some observational results.

2. Free versus forced transient analysis

An examination of the response of initially imposed perturbations on a Rankine vortex provides important theoretical insights into why TC-like vortices in the barotropic numerical models propagate steadily in a slightly deformed state in response to persistent environmental forcing, rather than rapidly distorting and dispersing. The unforced initial value problem analyzed in Chapter III represents the homogeneous counterpart to the forced steady propagation problem addressed in Chapter IV. By choosing initial conditions with the same spatial structure as in the forcing terms of the steady-state problem, the forced transient adjustments in numerical TC models may interpreted in terms of the analytically tractable unforced problem. This modeling technique permits a formal mathematical analysis of barotropic vortex adjustment to imposed asymmetries that was not possible for the related forced problem.

3. Closing the Barotropic Self-advection Model (BSAM)

Although the transformation to a reference frame moving with the TC was an important step in dividing the TC self-advection problem into manageable pieces, the presence of the propagation speed and direction in the interaction flow equation represented two additional unknowns. Thus, a closure scheme based on numerical results has been devised in which it is hypothesized that the correct propagation velocity will be associated with a particular wavenumber one gyre structure that has an approximate balance between vorticity tendencies due to the advection of large-scale absolute vorticity by the symmetric TC and the shearing of interaction flow vorticity by the symmetric TC winds. Specifically, the advection of the vorticity of the symmetric TC by the wavenumber one interaction flow is assumed to account for all of the propagation vector, except for a 0.4 m/s component associated with linear Rossby wave propagation of the dominant scale of the TC. The closure scheme depends sensitively, but predictably, on the two adjustable features of the BSAM associated with the transition radius. In a comparison with equivalent numerical model solutions, the closure scheme error was 0.25 m/s and 12° without any adjustment of the two available parameters.

B. SUMMARY OF RESULTS

1. Barotropic vortex stability

The first important result of this research is that the angular windshear of the symmetric circulation of TC-like vortices acts to make the vortex barotropically stable to small asymmetric perturbations from axisymmetry. The windshear in the symmetric circulation tilts the perturbations downshear, which results in a barotropically stable transfer of kinetic energy from the perturbation to the "basic state" represented by the symmetric vortex. The damping dependence is an algebraic continuous spectrum-type response analogous to the damping of perturbations imposed on an f-plane Couette flow. The damping rate is proportional to perturbation wavenumber, and is faster (slower) for perturbations with a radial structure that decays rapidly (slowly) with increasing radius. A wavenumber one perturbation associated with the advection of planetary vorticity by the symmetric TC loses about 80% of the initial kinetic energy by 24 h, which agrees well with the adjustment times in recent numerical modeling studies of TC adjustment on a β-plane. Thus, the quasi-steady propagation of TC's in barotropic models may be regarded as a balance between the transfer of kinetic energy from the symmetric TC to the wavenumber one interaction flow due to external asym-

metric forcing and the transfer of kinetic energy to the symmetric TC from the wavenumber one asymmetry due to the symmetric angular windshear.

The presence of significant tangential windshear in TC's, and the qualitative similarity of TC propagation tracks in baroclinic and barotropic models, strongly suggests that this barotropic vortex stability mechanism also may play a fundamental role in actual TC propagation. It should be emphasized that the asymmetry-damping influence of symmetric angular windshear is not limited to vortices scaled to approximate TC's. Rather, the shear-damping mechanism is applicable to any vortical flow that may be reasonably approximated by barotropic dynamics, and in which the strength of the vortical flow is strong compared to other influences over a significant horizontal area. Examples are Gulf Stream rings and other intense ocean eddies.

2. Dependence of propagation speed on TC strength

The piecewise-analytic symmetric TC wind profile in the BSAM permits propagation predictions for various tangential wind profiles. During testing of the closure scheme, it has been demonstrated that the BSAM-predicted propagation speed depends strongly on the magnitude of the symmetric vorticity gradient in the vicinity of the transition radius. This result complements the conclusions of Fiorino and Elsberry (1989) regarding strength changes quite well, since the transition radius is typically located near the middle of their 300-800 km critical annulus. Specifically, the BSAM demonstrates that the speed of TC propagation depends on the second derivative of the TC tangential winds, which explains why the propagation/wind-strength dependence is so strong.

The model has also been used with composite TC tangential wind profiles to obtain a practical estimate of the wind measuring accuracy required to avoid significant forecast error due to misrepresenting TC strength. Piecewise-analytic wind profiles have been constructed that underestimate, approximate, or overestimate the outer wind strength of a composite pressure-averaged typhoon. A quasi-linear relationship is found between the symmetric TC windspeed at 550 km and the associated propagation speed. Specifically, the speed of propagation increases by 1 m/s for a 2.4 m/s increase in v_s(550 km), which suggests that the TC outer wind strength must be measured to about ± 1 m/s to avoid having 24 h forecast errors greater than 85 km. The capability to alter outer wind strength by changing only one parameter suggests that the BSAM might be used to estimate an "effective" TC outer wind strength given sufficiently accurate information about the environmental windfield, the past propagation of the TC relative to environmental steering and the intensity of the storm.

3. Dependence of propagation on environmental vorticity

The influence of uniform environmental vorticity in altering the phase of the wavenumber one gyres in the Dispersion Region can be included in the BSAM for values of Z_F ($\times 10^{-5}$ s^{-1}) inside the range -0.5 to 1.5. An increased (decreased) propagation speed and a more (less) westward propagation direction is predicted when cyclonic (anticyclonic) uniform vorticity is present compared to β-induced propagation in a quiescent environment. Although the direction changes are generally consistent with propagation vectors in an unpublished numerical study by Chan and Williams (1989), a verification for the BSAM-predicted speed changes is not available. An unresolved issue here is that a steadily increasingly propagation speed is evident in the Chan and Williams solutions for anticyclonic shear, whereas an essentially steady propagation speed is found for cyclonic shear. If the steadily evolving propagation speed and asymmetry situation is relevant to TC's, then the question of how long the TC has been in a particular environment may be important to track forecasting.

BSAM predictions of TC propagation have been made for situations involving zonal and meridional gradients of environmental vorticity, the influence of β, and a uniform component of environmental vorticity. For example, a TC north (south) of the subtropical ridge where a westward gradient of environmental vorticity is also present is predicted to have a more northward (westward) and faster (slower) propagation in general agreement with composite observations in the western North Pacific (e.g., Fig. 1.1).

4. Numerical model initialization

An important potential application of the BSAM is to provide the initially symmetric bogus vortex of a barotropic numerical model with the correct wavenumber gyre structure so that quasi-steady propagation occurs immediately, and thus overcome a well-known slow bias. Such an application may also be regarded as an indirect test of the validity of the modeling concepts, techniques and assumptions employed in developing the BSAM. For a quiescent environment, the BSAM-predicted wavenumber one gyre produces virtually steady propagation regardless of whether an internally or externally-derived propagation velocity is used. Including the BSAM-generated gyres in the numerical model initialization reduces the along-track forecast error from more than 150 km to less than 60 km. This preliminary result shows that the BSAM has significant potential as an initialization tool for operational barotropic forecast models such as SANBAR.

The unresolved issue regarding nonsteady β-induced propagation in anticyclonic shear mentioned above precludes a precise estimation of the potential 48 h forecast error

133

reduction that might be achieved by a numerical model initialization with the BSAM. Nevertheless, the along-track (cross-track) differences of up to 280 km (80 km) between the 48 h positions of TC with and without BSAM-initialization illustrates the potential sensitivity of TC track prediction to the initial asymmetric structure of the TC when a spatially variable environment is present. Using the adjustable parameters in the BSAM to minimize barotropic forecast model track error in some statistical sense may be a viable approach for developing an initialization scheme that can improve barotropic numerical model forecast skill, and provide additional insights into the interaction of TC's with the surrounding environment.

APPENDIX A. COMPOSITE DATA CONVERSION

Composite studies have generally characterized TC propagation in relative terms (*e.g.*, speed and direction differences) using a rotated coordinate system aligned with storm motion. This compositing methodology tends to make theoretical interpretation of the data difficult because the analytical and numerical studies predict that TC propagation will possess a particular orientation with respect to the direction of the large-scale vorticity gradient. In particular, a rotated storm-relative coordinate system would tend to obscure TC propagation associated with the gradient of the Coriolis parameter, since that gradient has a storm and environment-independent northward orientation. Thus, part of the difficulty in comparing theory with the composite observations may be readily overcome by representing TC propagation as a vector quantity in a north-oriented earth-relative coordinate system.

The TC motion and steering flow composite data are taken from the latitude, direction, speed and intensity stratifications of Chan and Gray (1982) and George and Gray (1976) for the western North Pacific region, and the direction and recurvature stratifications of Holland (1984) for the Australian-Southwest Pacific region. Holland used a single steering flow definition based on a 800 to 300 mb pressure-weighted mean wind averaged over an annulus extending 5° to 7° lat. from the TC center. Although Chan and Gray used the same horizontal domain, several vertical averaging schemes were tested. Only the Chan and Gray steering flow based on a surface to 300 mb vertical average is used here, since it most closely approximates the steering flow definition used by Holland. Vertically-averaged steering flows have been chosen for this analysis rather than individual steering levels (*e.g.*, George and Gray 1976) to more appropriately compare the observations with the theoretical modeling results that are predominantly based on barotropic dynamics.

Table A.1 summarizes the conversion process for the western North Pacific composite data. The columns labelled V_{PM}, DD, V_C and D_C contain previously published data, and the last two columns have been computed using the relationships

$$D_B = D_C + DD \tag{A.1}$$

$$V_B = \frac{V_C + V_{PM}}{\cos DD} . \tag{A.2}$$

Table A.1 Original and converted composite TC motion data for the western North Pacific region. Column heading meanings: V_{PM} is the speed of the steering flow component parallel to the direction of the composite TC minus the speed of the TC; DD is the difference between the direction of TC motion and the steering flow; V_C and D_C are the speed and direction of motion of the TC respectively; and V_B and D_B are the speed and direction of the steering flow respectively. The data in columns V_{PM} and DD are taken directly from Chan and Gray (1982), and the data in columns V_C and D_C are taken directly from George and Gray (1976). The data in columns V_B and D_B have been computed as described in the text. Directions are measured clockwise from North and the data in the last four columns are relative to a reference frame fixed to the surface of the earth.

Composite Stratification	V_{PM} (m s)	DD (deg)	V_C (m s)	D_C (deg)	V_B (m s)	D_B (deg)
Latitude:						
>20°N (GT)	-1.0	19	5.6	352	4.9	011
<20°N (LT)	-1.6	6	5.1	300	3.5	306
Direction:						
Westward (W)	-2.3	17	6.2	285	4.0	302
Northward (N)	-1.0	17	5.3	324	4.5	341
Eastward (E)	-0.5	16	7.1	027	6.8	043
Speed:						
Slow (SL)	-0.9	27	2.4	338	1.7	005
Moderate (M)	-1.1	20	5.2	326	4.4	346
Fast (F)	-1.3	14	10.1	006	9.1	020
Intensity:						
Weak (WK)	-1.1	14	4.9	319	3.9	333
Intense (I)	-1.1	20	5.0	326	4.2	346
Very Intense (VI)	-1.7	26	5.2	319	3.9	345

All column labels are defined in the table caption. Table A.2 is analogous to Table A.1 for the Australian-Southwest Pacific composite data. The columns labelled SD, DD, V_B

and D_B contain previously published data, and the columns labelled V_C and D_C have been computed using (A.1) and

$$V_C = V_B - SD. \qquad (A.3)$$

The TC propagation vectors shown in Fig. 1.1 were then computed for each composite stratification using the last four entries in each row of Tables A.1 and A.2.

Table A.2 Analogous to Table A.1 for the Australian-Southwest Pacific region. The column headings DD, V_C, D_C, V_B and D_B have the same meanings as in Table A.1 and SD is the speed difference between the composite TC and steering. The data in columns SD, DD, V_B and D_B are taken directly from Holland (1984), except that the steering flow directions are measured clockwise from North. The data in columns V_C and D_C have been computed as described in the text.

Composite Stratification	SD (m/s)	DD (deg)	V_C (m/s)	D_C (deg)	V_B (m/s)	D_B (deg)
Direction:						
Westward (W)	1.3	-4	4.0	247	2.7	243
Southwestward (SW)	1.1	-18	3.6	241	2.5	223
Southward (S)	-0.5	-32	3.0	172	3.5	140
Southeastward (SE)	-1.1	-23	3.8	150	4.9	127
Eastward (E)	-1.2	-3	4.2	106	5.4	103
Recurvature:						
Before (B)	1.1	-13	3.5	238	2.4	225
Near (N)	0.5	-26	3.7	193	3.2	167
After (A)	-0.5	-2	5.0	162	5.5	160

APPENDIX B. PIECEWISE-ANALYTIC VORTEX CONSTRUCTION

The following outline describes the procedure for constructing piecewise-analytic radial profiles of TC tangential wind and relative vorticity. The approach here is to use the linear degrees of freedom in (4.6), (4.16) and (5.2) to develop closed-form expressions for the coefficients A_1, A_2, A_3, B_1, B_2, B_3 and C_3 such that the piecewise-analytic profiles must have continuous windspeed and relative vorticity. The remaining nonlinear degrees of freedom are then used to adjust the fit of the piecewise-analytic profiles to the corresponding analytic profiles by selecting various values for X_1 and X_2 and assessing the results via interactive computer graphics.

1. Given the trial values of R_0 and R_1 from Step 1 of the model solution procedure (Chapter IV Section A.4), choose trial values for $v_S(R_0)$ and $v_S(R_1)$. Generally R_0 will be in the vicinity of the radius of maximum winds, and thus $v_S(R_0) \approx 1$ will provide a good first estimate. The value of $v_S(R_1)$ for the piecewise-analytic vortex is chosen to closely approximate the windspeed of the analytic profile at R_1.

2. Determine the coefficients A_1 and B_1 for (4.6) in the first annulus, by solving the 2x2 linear system that results from applying the boundary conditions of Step 1 above to (4.6).

3. Determine the coefficients A_2 and B_2 by requiring the windspeed and vorticity of the piecewise-analytic TC structure to be continuous at R_1. As in Step 2 above, this entails solving a 2x2 linear system.

4. Repeat the process in Step 3 to determine the coefficients A_3 and B_3 in (4.16) by requiring the piecewise-analytic windspeed and vorticity to match at the transition radius R_T. For the piecewise-analytic profiles used in Chapter V, this step is modified to include evaluation of C_3 in (5.2) by solving the linear 3x3 system that results from requiring the piecewise-analytic windspeed, vorticity and vorticity gradient to be continuous at R_T.

5. Using interactive computer graphics, vary the parameters X_1 and X_2 to adjust the piecewise-analytic windspeed and vorticity profiles to approximate the analytic counterparts as described in Chapter IV Section B.1. During this step, also adjust R_0, R_1, $v_S(R_0)$ and $v_S(R_1)$ if necessary to achieve an acceptable fit.

LIST OF REFERENCES

Anthes, R. A., and J. E. Hoke, 1975: The effect of horizontal divergence and the latitudinal variation of the Coriolis parameter of the drift of a model hurricane. *Mon. Wea. Rev., 9,* 757-763.

Anthes, R. A., 1982: Tropical cyclones: their evolution, structure and effects. *Meteor. Monographs,* Vol. 19, No. 41, Amer. Meteor. Soc., Boston, 208 pp.

Boyd, J. P., 1983: The continuous spectrum of linear Couette flow with the Beta effect. *J. Atmos. Sci., 40,* 2304-2308.

Carr, L. E. III, and R. L. Elsberry, 1989: Observational evidence for predictions of tropical cyclone propagation relative to environmental steering. *J. Atmos. Sci.* (in press).

Case, K. M., 1960: Stability of plane couette flow. *Phys. Fluids, 8,* 143-148.

Chan, J. C.-L., 1986: Supertyphoon Abby - An example of present track forecast inadequacies. *Weather and Forecasting, 1,* 113-126.

-----, and W. M. Gray, 1982: Tropical cyclone movement and surrounding flow relationship. *Mon. Wea. Rev., 110,* 1354-1374.

-----, and R. T. Williams, 1987: Analytical and numerical studies of the Beta-effect in tropical cyclone motion. Part I: Zero mean flow. *J. Atmos. Sci., 44,* 1257-1265.

-----, and -----, 1989: Analytical and numerical studies of the Beta-effect in tropical cyclone motion. Part II: Zonal mean flow. To be submitted to *J. Atmos. Sci.*

DeMaria, M., 1985: Tropical cyclone motion in a nondivergent barotropic model. *Mon. Wea. Rev., 113,* 1199-1210.

-----, 1987: Tropical cyclone track prediction with a barotropic spectral model. *Mon. Wea. Rev., 115,* 2346-2357.

Elsberry, R. L., 1986: Some issues related to the theory of tropical cyclone motion. Technical Report NPS 63-86-005, Naval Postgraduate School, Monterey, CA 93943, 25 pp.

-----, 1988: ONR Tropical Cyclone Motion Research Initiative: Mid-year review, discussion and working group reports. Technical Report NPS 63-88-005, Naval Postgraduate School, Monterey, CA 93943, 86 pp.

-----, 1989: ONR Tropical Cyclone Motion Research Initiative: Field Experiment Planning Workshop. Technical Report NPS 63-89-002, Naval Postgraduate School, Monterey, CA 93943, 79 pp.

139

Farrell, B. F., 1982: The initial growth of disturbances in a baroclinic flow. *J. Atmos. Sci., 39*, 1663-1686.

-----, 1987: On developing disturbances in shear. *J. Atmos. Sci., 44*, 2718-2727.

Fiorino, M., 1987: The role of vortex structure on tropical cyclone motion. Ph. D. Dissertation, Naval Postgraduate School, 369 pp.

-----, and R. L. Elsberry, 1989: Some aspects of vortex structure related to tropical cyclone motion. *J. Atmos. Sci., 46*, 975-990.

Flierl, G. R., V.D. Larichev, J.C. McWilliams and G.M. Reznik, 1980: The dynamics of baroclinic and barotropic solitary eddies. *Dyn. Atmos. Oceans, 5*, 1-41.

Frank, W. M., 1977: The structure and energetics of the tropical cyclone. I: Storm structure. *Mon. Wea. Rev., 105*, 1119-1135.

George, J.E., and W. M. Gray, 1976: Tropical cyclone motion and surrounding parameter relationships. *J. Appl. Meteor., 15*, 1252-1264.

Hawkins, H. F., and S. M. Imbembo, 1976: The structure of a small, intense hurricane, Inez 1966. *Mon. Wea. Rev., 104*, 418-442.

Holland, G. J., 1983: Tropical cyclone motion: Environmental interaction plus a Beta effect. *J. Atmos. Sci., 40*, 328-342.

-----, 1984: Tropical cyclone motion: A comparison of theory and observation. *J. Atmos. Sci., 41*, 68-75.

Kao, S.-K., 1955: Wave motion in a rotating Couette flow of a viscous fluid. *Tellus, 7*, 372-380.

Kasahara, A, 1957: The numerical prediction of hurricane movement with the barotropic model. *J. Meteor., 14*, 386-402.

-----, and G. W. Platzman, 1963: Interaction of a hurricane with the steering flow and its effect upon hurricane trajectory. *Tellus, 15*, 321-335.

Kitade, T., 1980: Numerical experiments of tropical cyclones on a plane with variable Coriolis parameter. *J. Meteor. Soc. Japan, 58*, 471-488.

-----, 1981: A numerical study of the vortex motion with barotropic models. *J. Meteor. Soc. Japan, 59*, 801-807.

Kuo, H. L., 1950: The motion of atmospheric vortices and the general circulation. *J. Meteor., 26*, 390-398.

Madala, R. V., and S. A. Piacsek, 1975: Numerical simulation of asymmetric hurricanes on a β-plane with vertical shear. *Tellus, 27*, 453-467.

McCalpin, J. D., 1987: On the adjustment of azimuthally perturbed vortices. *J. Geophys. Res., 92*, 8213-8225.

McWilliams, J. C., and G. R. Flierl, 1979: On the evolution of isolated nonlinear vortices. *J. Phys. Oceanogr., 9,* 1155-1182.

Merrill, R. T., 1984: A comparison of large and small tropical cyclones. *Mon. Wea. Rev., 112,* 1408-1418.

Mied, R. P., and G. J. Lindemann, 1979: The propagation and evolution of cyclonic Gulf Stream rings. *J. Phys. Oceanogr., 9,* 1183-1206.

Neumann, C. J., and J. M. Pelissier, 1981: Models for the prediction of tropical cyclone motion over the North Atlantic: An operational evaluation. *Mon. Wea. Rev., 109,* 522-538.

Pedlosky, J., 1964: An initial value problem in the theory of baroclinic instability. *Tellus, 16,* 12-17.

Peng, M. S., and R. T. Williams, 1989: Dynamics of vortex asymmetries and their influence on vortex motion on a β-plane. Submitted to *J. Atmos. Sci.*

Rossby, C.-G., 1939: Relation between variations in the intensity of the zonal circulation of the atmosphere and the displacements of the semi-permanent centers of action. *J. Marine Res., 2,* 38-55.

-----, 1948: On the displacements and intensity changes of atmospheric vortices. *J. Mar. Res., 7,* 175-196.

Sanders, F., A. C. Pike and J. P. Gaertner, 1975: A barotropic model for operational prediction of tracks of tropical storms. *J. Appl. Meteor., 14,* 265-280.

Shapiro, L. J., and K. V. Ooyama, 1989: Barotropic vortex evolution on a β-plane. Submitted to *J. Atmos Sci.*

Smith, R. K., W. Ulrich and G. Dietachmayer, 1989: A numerical study of tropical cyclone using a barotropic model. Part I. The role of vortex asymmetries. Submitted to *Quart. J. Roy. Meteor. Soc.*

Thompson, W. J., R. L. Elsberry and R. G. Read, 1981: An analysis of eastern North Pacific tropical cyclone forecast errors. *Mon. Wea. Rev., 109,* 1930-1938.

Weatherford, C. L., and W. M. Gray, 1988: Typhoon structure as revealed by aircraft reconnaissance. Part II: Structural variability. *Mon. Wea. Rev., 116,* 1044-1056.

Willoughby, H. E., 1988: Linear motion of a shallow-water, barotropic vortex. *J. Atmos. Sci., 45,* 1906-1928.

Yeh, T. C., 1950: The motion of tropical storms under the influence of a superimposed southerly current. *J. Meteorology, 7,* 108-113.

INITIAL DISTRIBUTION LIST

No. Copies

1. Defense Technical Information Center   2
   Cameron Station
   Alexandria, VA 22304-6145

2. Library, Code 0142   2
   Naval Postgraduate School
   Monterey, CA 93943-5002

3. Oceanographer of the Navy   1
   U.S. Naval Observatory
   34th and Massachusetts Ave. N.W.
   Washington, D.C. 20390

4. Commander   1
   Naval Oceanography Command
   NSTL Station
   Bay St. Louis, MS 39522

5. Commanding Officer   1
   Fleet Numerical Oceanography Center
   Monterey, CA 93943-5105

6. Chief of Naval Research   1
   Marine Meteorology Program (Code 1122MM)
   800 N. Quincy St.
   Arlington, VA 22217

7. Commanding Officer   1
   Naval Western Oceanography Center
   Box 113
   Pearl Harbor, HI 96860

8. Commanding Officer   1
   Naval Oceanography Command Center, Guam
   COMNAVMARIANAS Box 12
   FPO San Francisco, CA 96630-2926

9. Chairman (Code 63Rd)   1
   Department of Meteorology
   Naval Postgraduate School
   Monterey, CA 93943-5000

10. Prof. R. L. Elsberry (Code 63Es)   10
    Department of Meteorology
    Naval Postgraduate School
    Monterey, CA 93943-5000

11. Prof. R. T. Williams (Code 63Wu)   10
    Department of Meteorology
    Naval Postgraduate School
    Monterey, CA 93943-5000

12. Assoc. Prof. P. A. Durkee (Code 63De)   1
    Department of Meteorology
    Naval Postgraduate School
    Monterey, CA 93943-5000

13. Adj. Res. Prof. M. S. Peng (Code 63Pg)   1
    Department of Meteorology
    Naval Postgraduate School
    Monterey, CA 93943-5000

14. Dr. D. C. Smith IV   1
    Nova University Oceanography Center
    8000 North Ocean Drive
    Dania, FL 33004

15. LCDR L. E. Carr III   5
    Naval Oceanography Command Center
    COMNAVMARIANAS Box 12
    FPO San Francisco, CA 96630-2926